NASA CONTRACTOR REPORT 166021

DESIGN AND TEST OF AIRCRAFT ENGINE ISOLATORS FOR REDUCED INTERIOR NOISE

James F. Unruh and Dennis C. Scheidt

SOUTHWEST RESEARCH INSTITUTE
San Antonio, Texas 78284

CONTRACT NAS1-14861
DECEMBER 1982

National Aeronautics and
Space Administration

Langley Research Center
Hampton, Virginia 23665

SOUTHWEST RESEARCH INSTITUTE
Post Office Drawer 28510, 6220 Culebra Road
San Antonio, Texas 78284

NASA CONTRACTOR REPORT 166021

DESIGN AND TEST OF AIRCRAFT ENGINE ISOLATORS FOR REDUCED INTERIOR NOISE

James F. Unruh and Dennis C. Scheidt

SOUTHWEST RESEARCH INSTITUTE
San Antonio, Texas 78284

CONTRACT NAS1-14861
DECEMBER 1982

Approved by:

H. Norman Abramson, Vice President
Engineering Sciences Division

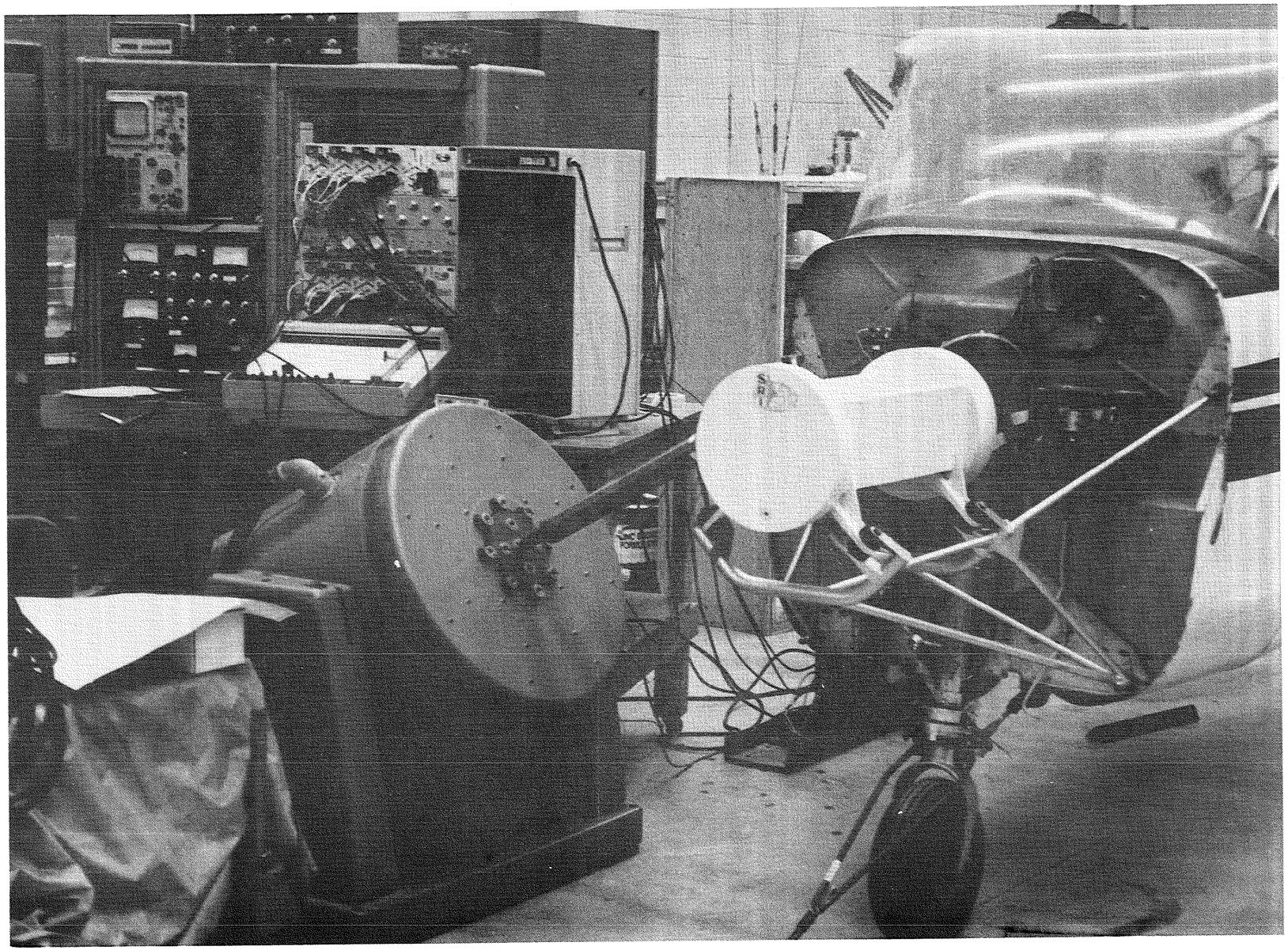

FRONTISPIECE

TABLE OF CONTENTS

TABLE OF CONTENTS (CONTINUED)

LIST OF TABLES

LIST OF FIGURES

LIST OF FIGURES - CONTINUED

LIST OF FIGURES - CONTINUED

NOMENCLATURE

f	harmonic frequency
f_d	driving frequency
f_n	equipment support frequency
f_{BAND}	one-third octave frequency band
g	acceleration due to gravity
i	complex number $\sqrt{-1}$
k	complex isolator stiffness
rpm	engine speed
A_B	base excitation acceleration
A_m	supported mass acceleration
AB	airborne component
ARMS	engine overall r.m.s. acceleration
CF	force level correction factor
DRMS	engine overall r.m.s. displacement
F	engine force level
F_r	reference force level
K	parameter defined in Equation (10)
K_A	isolator axial stiffness, frequency dependent
$\overline{K}_A$	isolator axial stiffness at 100 Hz
K_A^s	isolator axial static stiffness
L_R	ratio of isolator radial to axial stiffness
OASPL	overall sound pressure level
P1,P2,P3	microphone locations
P12	maximum OASPL when considering P1 and P2
P123	maximum OASPL when considering all microphones
SB	structure-borne component
SPL	sound pressure level
SPL_r	reference sound pressure level
T	transmissibility
W	supported test weight
X_B	base excitation displacement

X_A	supported mass displacement
X,Y,Z	coordinates of aircraft reference system
β	frequency harding parameter and critical damping ratio
γ	ratio of f_d to f_n
η	material loss factor
θ	phase angle, in general
θ_X^S	engine rotation about X axis
ω	circular frequency, $2\pi f$

I. INTRODUCTION

Over the past several years Southwest Research Institute has been pursuing an active research program to gain a better understanding of the sources of structure-borne interior noise, paths of propagation and methods of noise control in lightweight general aviation aircraft. During the conduct of the program a single engine light aircraft was employed as a ground test vehicle in a series of engine attached and engine detached, engine running tests to determine the relative levels of structure-borne and airborne noise (ref. 1-2). From the ground test results it was concluded that engine induced structure-borne noise was equal to or greater than airborne noise transmission and therefore a concentrated effort in the area of developing structure-borne noise control measures would be necessary if overall interior noise of the aircraft were to be reduced.

A structure-borne interior noise prediction model of the test aircraft was then developed (ref. 2) using a structural acoustic finite element modeling procedure (ref. 3). A comparison of predicted results to laboratory measured aircraft response and to engine running data showed that structural-acoustic coupling, i.e., fuselage flexibility, had a strong influence on the fundamental cabin acoustic resonances and provided the major low frequency path for engine induced structure-borne noise. It was also found that the lightweight fuselage structure had a high modal density which would limit the useful frequency range for which deterministic modeling procedures would be applicable. Using the model in the frequency range below 200 Hz (ref. 4), it was concluded that the most effective and lightweight noise control measure would appear to be improved engine vibration isolation.

Data on the effectiveness of improved engine vibration isolators for reduced structure-borne noise transmission was not available in the literature and therefore the efforts of the program were directed towards a study of this potential noise control measure. A laboratory test procedure was developed to simulate engine induced structure-borne noise transmission in the test aircraft via electrodynamic shaker excitation (ref. 5). The general arrangement is shown as the frontispiece to this report. Analysis of the interior sound

pressure level transfer function data for a series of isolators with varying mechanical properties showed, as expected, that decreasing the engine support frequencies results in reduced structure-borne noise transmission out to approximately 150 Hz. Beyond 150 Hz isolation levels off and appears to decrease somewhat above 600 Hz. It was concluded that elastomeric isolators do not respond as constant parameter single degree-of-freedom components, but rather exhibit responses characteristic of components with frequency dependent properties. A procedure was then developed for the evaluation of engine vibration isolators for reduced structure-borne noise transmission by coupling analytical models of the engine, vibration isolators, and engine mount structure to an empirical model of the fuselage (ref. 6). By comparison of predicted structure-borne noise transmission to laboratory based measurements it was observed that isolator stiffness was a strong parameter governing the noise transmission while isolator damping was a much weaker parameter. It was also found that for the test aircraft, moderate changes to the lightweight, high strength engine mount structure did not affect the transmission phenomena. The study indicated that the modeling procedures were adequate to judge the relative performance of candidate isolators for the purpose of retro-fit isolator design if the mechanical properties of the isolators were known (ref. 6).

The objective of the present study was to develop the structure-borne noise transmission model into an isolator retrofit design tool. The model was used to predict the required isolator characteristics for a desired level of noise reduction relative to the performance of the original equipment isolators. Improved isolators were then built and tested for a proof of concept evaluation.

The components of the structure-borne noise transmission model used in the previous and present investigations are reviewed in Section II of this report, and the corresponding mathematical procedures are presented in detail in references 5 and 6. The isolator design specification developed for this study is discussed in Section III. Of primary importance in the correlation of the design predictions and the test results is the selection of isolator configurations to meet the design objective and evaluation of their static and dynamic material properties which is the subject of Section IV of this report.

It should be emphasized that the dynamic properties of a majority of the isolators available from "off the shelf" sources are not known. Isolator manufacturers generally limit dynamic measurements to the frequency range up through 100 to 200 Hz and these measurements are usually carried out on material coupons to determine material static to dynamic ratios, loss factors, and material modulus. Determination of isolator properties in the installed configuration, i.e., proper preload and excitation levels is a difficult task as will be seen by the data and discussions presented in Section IV. Section V discusses the test setup used to evaluate the candidate isolators and discusses the corresponding test results. Correlation of test results to the design model predictions using the measured isolator properties is reported in Section VI with conclusions given in Section VII.

Use of trade names or names of manufacturers in this report does not constitute an official endorsement of such products or manufacturers, either expressed or implied, by the National Aeronautics and Space Administration.

II. NOISE TRANSMISSION MODEL

A detailed description of the structure-borne interior noise transmission model used during this investigation is given in references 5 and 6. Only a brief review of the model components and model correlation to previous laboratory sweep data will be given in the following sections.

A. Model Components

The scope of the study described in reference 6 was for the most part limited to investigating the influence of changes in the engine mount structure and vibration isolators on the structure-borne noise transmission characteristics of the test aircraft. Noise control changes to the fuselage/cabin area were not included in the study and therefore the fuselage/cabin response was characterized empirically. Components forward of the fuselage firewall were modeled analytically so that design variations could be easily incorporated into the system model. The model was developed using the conventional global axis system, where X is aft along the centerline of the fuselage, Y is to the pilot's right and Z is upward for a right-handed system. The frontispiece shows the physical arrangement of the test components.

The aircraft engine was replaced with a dummy engine having equivalent mass, center of gravity, and inertia. The dummy engine was modeled as a six-degree-of-freedom rigid body. As illustrated in Figure 1a, connection of the engine to the isolators is visualized via four rigid extension arms. At the isolator attach points it was assumed that the three translational degrees of freedom were sufficient to model the transmitted engine loads to the vibration isolators.

The vibration isolators are modeled as three mutually perpendicular frequency dependent translational springs at each of the engine to engine mount attach points. Isolator properties were specified with respect to their local axial and radial coordinates as shown in Figure 1b and then transformed to the global axis system.

The engine mount structure consists of a truss-like assemblage of 1.91 and 1.59 cm 4130 steel tubes which form a very strong and lightweight (5.22 kilograms) carrythrough structure. The structure is shown schematically in Figure 1c and was modeled using a finite element beam idealization. The free-free structure exhibited fifty one normal mode responses below 1000 Hz, which when added to an additional six rigid body degrees-of-freedom, allowed arbitrary motion of the structure to be completely described. Again only the translational degrees of freedom at the isolator attach points were retained for load/motion carrythrough. Likewise only the three translational degrees of freedom at each of the four engine mount to firewall attach points were retained to be consistent with the fuselage/firewall representation.

The dynamic characteristics of the fuselage at the engine mount attachment points and the response of selected cabin interior locations were determined by what is generally referred to as point and/or transfer impedance testing. A frequency dependent dynamic stiffness matrix data base was developed for the fuselage structure in terms of the firewall translational degrees of freedom at the engine mount attach points as are shown in Figure 1d. Along with the structural characterization of the fuselage, firewall force excitation to interior sound pressure level transfer functions were recorded at three cabin locations. P1, P2, and P3. The cabin response microphone locations are shown in Figure 2 wherein P1 is positioned at the pilot's ear level, P2 at the copilot's ear level and P3 mid-cabin at the passenger's ear level. A continuous random source was used in the transfer impedance and SPL transfer function tests using a bandwidth of resolution of 2.0 Hz with sufficient sample averaging to insure a normalized standard error of less than 1 dB. The data base was developed in the frequency range from 10 to 1000 Hz.

Typical measured cabin and firewall spectral responses are shown in Figure 3. As can be seen by the SPL transfer function data the cabin, which was void of interior trim, was very rich in resonant response. The fundamental cabin acoustic resonance occurred at around 64 Hz, as denoted, however many of the resonant responses were local structural panel responses. In Figure 4, as taken from reference 2, several of the test aircraft panel

resonant responses are given along with their panel locations. The measured fuselage driving point inertance, as given in Figure 3, shows the fuselage structure to be primarily stiffness like throughout the frequency range of interest.

The component models were coupled via force summations at each of the component interfaces, i.e., the rigid engine to isolators, the isolator to engine mount, and engine mount to fuselage firewall. Compatibility of displacements at each of the component interfaces was assured through the use of consistent nodal displacements throughout the component models. The resulting coupled equations of motion were programmed for solution in FORTRAN-IV-Plus on a PDP 11/70 minicomputer.

B. Model Correlation to Sweep Data

Sound pressure level (SPL) transfer function predictions were compared to laboratory generated data for several isolator configurations to obtain a measure of confidence in the interior noise transmission model. In the laboratory setup, pictured in the frontispiece, a 7100N electrodynamic shaker was used to drive the engine harmonically at a constant force level (normally 89 N_{rms}) while cabin sound pressure level responses were recorded for the three interior microphones P1, P2, and P3 shown in Figure 2. The sound pressure level data generated for a reference excitation level of F_r may be used to obtain SPL at any excitation level F by the use of the expression

$$SPL = SPL_r + 20 \log_{10} (F/F_r), \qquad (1)$$

thus the terminology transfer function spectra is used to describe such data. Typical cabin SPL transfer function data are shown in Figure 5a for test configurations employing a set of rigid isolators, a set of original equipment isolators (3006-H) and a set of soft rubber mounts (22002-1). As can be seen the interior SPL spectra are quite rich in resonant response. The lack of increased isolation in the higher frequency region as expected from model predictions (ref. Figure 5b), was quite surprising. The predicted spectra shown in Figure 5b were based on the isolators static rated properties (ref. 6).

The disagreement between measured and predicted SPL observed in the previous work suggested that dynamic isolator properties should be used to try to obtain improved agreement between predictions and laboratory data. To this end laboratory procedures were developed that would allow direct isolator stiffness determination via transmissibility tests. The procedures are discussed in Section IV of this report along with the isolator stiffness properties of a number of isolators used during this investigation (ref. to data summary in Table 3). Typical results of the transmission model correlation to the previously generated sweep data, when measured isolator dynamic material properties are used, are given in Figure 6. In Figure 6 the maximum SPL transfer function response in each one-third octave band among P1, P2, and P3 is plotted versus the band center frequency for a shaker force input of 89 N_{rms}. In Figure 6a the correlation for the rigid isolators is given wherein the model predictions are quite good up through 315 Hz while thereafter the model predictions fall off. This is attributed to lack of representation in the model wherein the rotational degrees of freedom, i.e., moment transfer, at the engine to engine mount and/or engine mount to firewall attach points were not included. The following correction factors, taken from the rigid isolator correlation analysis, were included in the model in an attempt to compensate for this effect.

One-Third Octave	ΔSPL
400	9.2
500	13.0
630	9.3
800	18.3

In Figure 6b correlation of the model predictions to measured sweep SPL transfer function data are given for the soft rubber (22022-1) isolators. The isolator dynamic material properties were used in the predictions and as can be seen correlation to the measured data is quite good out to 250 Hz, however the high frequency predicted roll off is still somewhat noticeable even when the above (rigid isolator) correction factors are applied. Nevertheless, it was felt that the transmission model was sufficiently accurate to be used in a design study aimed at determining trends in isolator properties necessary to achieve a desired level of structure-borne noise transmission.

Based on the noise transmission data taken during the present investigation, it is now believed that the measured transfer function data of Figure 6b were contaminated by direct shaker airborne noise transmission beyond the 315 Hz band. A discussion of the effects of the direct airborne noise transmission will be given in Section VI.

C. Model Simplification

Previous studies of the engine mount structure had shown the elastic response of the high strength-lightweight structure to have little influence on the predicted interior noise. This observation was also qualitatively verified experimentally (ref. 6). In an effort to reduce computational time, the elastic mode responses of the engine mount structure were removed from the equations of motion, and only the rigid body transformations between the engine isolators and fuselage attach points were retained. Calculations were then made to determine the effect of the reduced formulation. The maximum interior SPL responses with the reduced model varied at most 0.5 dB from the full model results. Computational time, however, was reduced by a factor of approximately seven (7). This simplified model was employed during the present investigation.

III. ISOLATOR DESIGN SPECIFICATION

Armed with a structure-borne noise transmission prediction model how does one determine the required isolator mechanical properties to achieve a desired noise reduction goal and what are the overall aircraft design penalties or constraints? The present study was aimed at answering these questions with as much realism for an inflight design/evaluation as possible within the budgetary constraints of the program. To this end the design specification and evaluation was limited to laboratory simulations of expected inflight engine excitation. This approach was also prompted by the lack of inflight or engine running ground test procedures that would allow determination of reduced levels of structure-borne noise in the presence of a high level of airborne noise transmission, i.e., reliable source separation procedures.

A. Postulated Inflight Engine Excitation

The engine running - engine attached/detached data obtained during a previous investigation (ref. 2) was used in order to establish a more realistic source than the uniform sweep of 89 N_{rms} (20 lb_f rms) used during the transmission model development. The engine running structure-borne noise spectra provide a realistic measure of the relative importance of each one-third octave band level to the overall spectrum sound pressure level. During flight the aircraft engine operates in the speed range from 2100 to 2700 rpm. Using the measured structure-borne interior noise levels at an engine speed of 2160 rpm, the shaker force level for the configuration shown in the frontispiece (termed Load Case #2 in ref. 6) was adjusted such that the predicted one-third octave SPL data using the original equipment isolators (with dynamic to static factors) matched the measured levels. The measured structure-borne noise spectra at 2160 rpm are given in Figure 7. The input force spectrum consisted of harmonics of 18 Hz (2160/120) out to 1000 Hz. The resulting force tone levels relative to 89 N_{rms} are given in Figure 8. Here we note that each level is assigned to the tone which can then take on various spectrum frequencies depending on the desired engine speed.

It was assumed that the dynamic engine forces are proportional to the engine static torque levels which result in an overall force level correction versus engine speed. From aircraft performance charts (ref. 8) the engine torque at a given altitude is related to engine rpm. When the torque level at 2160 rpm (23750 cm-N) is used as a reference, a force level correction factor of the form

$$CF = 3.392 - 5166/rpm \tag{2}$$

results for a reference altitude of 762 meters (2500 ft). Here we see that at an engine speed of 2640 rpm the force levels increase by 44% over those at 2160 rpm.

The above engine force excitation spectra were developed from available data for the purposes of a design procedure evaluation and would not be recommended for inflight isolator design. A much more direct method for engine force measurement/evaluation would be necessary for actual flight worthy hardware specification and design.

B. Design Parameters

1. Engine Speed

An envelope of expected interior SPL's for the original equipment isolators was developed from predicted spectra generated at engine speeds of 2160, 2280, 2400, 2520, and 2640 rpm as given in Figure 9. The SPL at the prop-tone, in the 80 Hz band, is rather consistent for all engine speeds while considerable variations occur in other bands of the spectrum. This is especially true in the 250 Hz band where the expected SPL levels exceed those in the 80 Hz band. The importance of optimizing an isolator design for the range of possible engine speeds can be seen by this data, since the spectrum shape changes radically with engine speed. While there exists an infinite number of engine speeds in the aircraft operating range, for the purpose of this study the five engine speeds given above were used exclusively. The corresponding engine 1/2 rpm harmonics are, respectively, 18, 19, 20, 21, and 22 Hz. The maximum overall sound pressure level for the original equipment isolators occurs at the highest engine speed (2640 rpm) at a level of 114.2 dB. As will be seen, this is not always the case, since for other

isolator configurations the maximum OASPL level may occur at other engine speeds, depending on the engine support frequency.

2. Engine Motion

The DRMS value listed for the various engine speeds in Figure 9 is the engine overall rms displacement in centimeters. The overall displacement level is computed from the square root of the sum of the squares (SRSS) of engine displacements computed at each engine harmonic. At each harmonic the engine c.g. displacements, and rotations multiplied by a 50.8 cm (20 in.) arm are combined via a SRSS to obtain a measure of overall engine motion. Thus, the DRMS is an estimate of the expected, cowling to engine or spinner displacement, etc., dynamic motion due to engine excitation. Figure 9 shows that the engine dynamic displacement (DRMS) decreases with increasing engine speed, even though an increase in force level occurs with increasing engine speed as given by the torque correction factor CF. This is due to the engine support frequency remaining fixed (isolator properties are fixed) while the input force spectrum continuously shifts to higher frequencies with increasing engine speed, thus increased vibration isolation. For a particular aircraft isolator retrofit design a more specific engine motion prediction would be specified based on potential design constraints.

For engine mounted equipment, changes in the overall engine acceleration environment (ARMS) may be of interest, and therefore the engine acceleration levels were also computed based on the 50.8 cm sphere about the engine c.g. in an identical manner as were the overall displacement levels.

The engine motion of primary importance to the designer may be that due to static torque rotation. There are other possible engine motions; however, we consider herein only the θ_X^S rotation (ref. Figure 1a). With engine torque expressed in terms of engine speed (ref. 7) an expression was developed to relate engine rotation to engine speed and isolator stiffness in the form

$$\theta_X^S = (37.454 - 57048/\text{rpm}) \; / \; K_A^S \qquad (3)$$

where θ_x^s is the engine rotation in radians due to static torque loading, rpm is the engine speed, and K_A^s is the axial static stiffness of one of the isolators in N/cm. For the original equipment isolators, K_A^s = 4640 N/cm. At engine speeds of 2160 and 2640 rpm, the engine static rotations are, respectively, 0.0024 and 0.0034 radians or 0.122 and 0.173 centimeters based on a maximum distance, engine c.g. to cowling, of 50.8 centimeters. Thus it can be seen, by comparing these displacements to the DRMS values given in Figure 9, that the static torque displacement exceeds the engine dynamic displacements and that the expected dynamic displacement levels will become even less important when the support frequency drops, since the static displacement increases as K_A^s decreases. Noting that the maximum engine static torque is produced at the highest engine speed of 2640 rpm, the engine maximum static displacement X_e, at a rotational arm of 50.8 centimeters, may be expressed in terms of the isolator static axial stiffness K_A^s, as (using Equation (3) directly)

$$X_e = 805./K_A^s \tag{4}$$

where X_e is expressed in centimeters and K_A^s in N/cm. This expression is used directly to obtain a relative measure of the expected engine deflection for a candidate isolator.

3. Isolator Mechanical Properties

The potential frequency depenence of an isolator was included in the design model by postulating a maximum allowable isolator stiffness versus frequency envelope of the form

$$K_A = \overline{K}_A \begin{cases} 1.0 & f \leq 100 \\ [100.-\beta+(\beta-1)f^2/10000.]/99. & 100 \leq f \leq 1000 \end{cases} \tag{5}$$

where β is a parameter in the range from 1 to 10. A normalized stiffness spectrum is plotted in Figure 10 showing the effect of the β parameter on the isolator stiffness. From the measured stiffness properties of the soft rubber isolator (22022-1) it was found that a minimum value of β would be on the order of 2 to 3. Measured values of β for several isolators are given in Section IV. The above spectrum specifies the isolator axial stiffness

and the parameter denoted as L_R (called L-ratio) was used to specify the ratio of radial to axial stiffness. The use of the L-ratio is consistent with isolator manufacturer's static stiffness product specifications. As will will be seen by the data presented in Section IV, the use of the L-ratio is normally conservative when specifying isolator dynamic properties.

Previous studies (ref. 6) showed that the isolator material loss factor, η, was a weak parameter with respect to noise transmission. In the present study the isolator material loss factor was considered to be frequency independent and employed in the usual way as a structural loss factor,

$$k = k(\omega)\ (1 + i\eta). \tag{6}$$

C. Parametric Design Curves

The input parameters to the structure-borne noise transmission model were as follows:

rpm	Engine speed
$\overline{K}_A$	Isolator axial dynamic stiffness
L_R	Ratio of radial to axial stiffness
β	Ratio of stiffness at 1000 Hz to stiffness at 100 Hz
η	Isolator material loss factor.

Upon entry of these parameters into the transmission model, expected maximum (based on maximum response from [P1, P2, P3]) sound pressure level one-third octave spectra (both unweighted and A-weighted) were generated along with displacement and acceleration spectra and overall spectrum levels out to 1000 Hz. Maximum OASPL and OASPL(A) values were determined from spectra generated at the five engine speed settings, 2160, 2280, 2400, 2520, and 2640 rpm with the maximum OASPL and OASPL(A) not always occurring at the same engine speed.

The axial dynamic stiffness considered in the parameter study were $\overline{K}_A$ = 438. (250.), 875. (500.), 1750. (7000.), 3500. (2000,) and 7000 N/cm (4000 lb/in.), with corresponding engine static torque deflections, based on an isolator static to dynamic ratio of 2.0, of 3.68 (1.45), 1.84 (0.124), 0.919 (0.362), 0.450 (0.181), and 0.230 cm (0.091 in.). The L-ratio was

varied from 0.25 to 8.0 and, as will be seen, is one of the stronger parameters except for $\overline{K}_A$. Material loss factor, η, was varied in the range from 0.05 up through 0.45.

A series of isolator design curves were developed based on the above range of parameters and are presented in Figures 11 through 16. In Figure 11 predicted maximum unweighted OASPL levels are given versus L-ratio for nominal values of β and η and at various values of isolator axial stiffness. Depending on the stiffness value, $\overline{K}_A$, an optimum value of L_R appears to be around the value of 2.0. The dependence of OASPL on the frequency dependence of the isolator material, β, is given in Figure 12 for nominal values of L_R and η at several axial stiffness values. We can see from these data that the unweighted interior noise levels are insensitive to the specified isolator frequency dependence, thus peak levels occur in the lower frequency range where β has little or no effect. In Figure 13 the effects of varying the isolator material loss factor, η, on the OASPL for various values of $\overline{K}_A$ and nominal values of L_R and β are given. As can be seen η is a very weak parameter except at the very high engine support stiffnesses. At a low support stiffness ($\overline{K}_A$) the input force spectrum is above the support frequency and thus a slight increase in OASPL is realized while at the highest support stiffness, the input force spectrum would lie within the engine support frequency where an increasing loss factor would reduce OASPL's. The effects of η are not felt to be important with respect to interior noise transmission.

In Figures 14 through 16 similar data are presented with the A-weighted OASPL values as the dependent design variable. As shown in Figure 14, the optimum L-ratio is not around 2.0 but would be closer to 0.25, i.e., the isolator needs to be weaker in the radial direction than in the axial direction by a factor of 4.0. At the higher values of support stiffness we can see considerable variations of OASPL with L-ratio, local minimum occur with 5 dB(A) variations. Physical reasons for these variations will be discussed below. In Figure 15 the effects of variation of β on the expected A-weighted OASPL's are shown. As can be seen, an increase in β results in an increase in OASPL(A), with more pronounced effects at the higher support

stiffnesses. The general trend is expected since the A-weighted network reduces the low frequency components of the response. Again at the higher support stiffness increased sensitivity occurs. The effects of variation of material loss factor, η, on the A-weighted OASPL's is given in Figure 16. Note that the increased transmission due to increased loss factor is more pronounced than for the unweighted values and at the 7000 N/cm support stiffness a benefit is realized when increasing η. Nevertheless, in the range of stiffness for which an improved design is desired, the material loss factor appears to be a weak parameter in governing the selection of an isolator for reduced structure-borne noise transmission.

Throughout the range of parameters considered the engine acceleration levels varied from 24.5 g to 27. g with maximum one-third octave spectrum levels on the order of 18. g's. The engine acceleration levels were governed mainly by the engine mass and input force spectrum, however the ARMS increased with increasing $\overline{K}_A$ and L_R with little dependence on β. The engine dynamic displacement levels, DRMS, remained well below the engine static torque displacement levels and therefore have negligible effect on overall engine displacements. Similar results would be expected if engine static thrust and thrust oscillations were to be considered in the design evaluation.

The rather odd noise transmission behavior occurring at the higher isolator stiffnesses as is shown in Figures 14 and 15, is attributed to a change in fuselage stiffness at the higher frequencies. Recall that a driven mass sees not only the spring stiffness of its isolator support but also the stiffness of the base to which the isolator is attached. In this case the fuselage stiffness at the engine mount attach points is of interest. A general rule of thumb is to supply a base stiffness ten (10) times that of the isolator. This can be quite difficult to achieve in lightweight aircraft construction. In Figure 17 the firewall engine mount attach point stiffnesses are given for the Cessna 172 test aircraft. The upper values given in Figure 17 are the stiffness values at 100 Hz and the lower values, the minimum stiffness occurring out to 1000 Hz. The lower engine mount attach points (2,3) attach directly into the channel stiffened box beam floor structure while the upper attach points are connected, via a hat section, to the main door

forward support structure which is somewhat weaker than the lower carrythough structure. With an isolator stiffness of say 3500 N/cm axial direction and 7000 N/cm in the radial direction (L_R = 2.0), a stiffness ratio (isolator to fuselage) of 10:1 is only possible for the longitudinal direction at or below 100 Hz. If β = 3, at a 1000 Hz we would have isolator stiffnesses on the order of 10,500 and 21,000 N/cm, respectively. At this point the engine may as well be connected directly to the engine mount structure. Thus to achieve a 10:1 stiffness ratio in all directions may be impossible if the isolators exhibit a frequency hardening effect such as for β = 3.

For the purposes of developing adequate isolator designs to withstand the expected dynamic environment the peak differential displacements and accelerations across the isolators were computed for support configurations with $\overline{K}_A$ being equal to or less than 1750 N/cm. The peak expected differential displacement across the isolator occurs at 1/2 rpm harmonic number 4, in the frequency range from 72 to 88 Hz, at a value of 0.015 cm. The corresponding maximum differential acceleration is approximately 7 g's.

D. Design Objective

The predicted maximum interior sound pressure level spectra for the original equipment isolators is given in Figure 18. The maximum OASPL and OASPL(A) occurred at an engine speed of 2640 rpm at levels of 114 dB and 105 dB(A), respectively. A design objective was set at reducing these predicted maximum SPL levels by 15 dB, thus the objective could be met by reducing the structure-borne noise levels to 99 dB and 90 dB(A).

From the design curves given in Figures 11 through 15 it can be seen that a rather wide selection of possible isolator parameters is allowed so long as the isolator axial dynamic stiffness is 1750 N/cm (1000 lb/in) or less. We may also note that it is the unweighted spectrum that will control the isolator design, so long as the L-ratio is somewhat less than 5.0. A reasonable design improvement could be expected by selecting $\overline{K}_A$ = 1750 N/cm, L_R = 2.0, β = 3.0, η = 0.15 resulting in OASPL levels of 97.8 dB and 84.2 dB(A). This design choice results in a 16 dB or 20 dB(A) decrease in expected interior noise levels. The penalty for this increase in transmission

loss is a predicted increase in engine motion from 0.172 cm to 0.919 cm due to static torque. The predicted engine dynamic acceleration levels increased from 24.8 g rms to 26.9 g rms when reducing the isolator stiffness from $\overline{K}_A$ = 8055 N/cm to 1750 N/cm.

In Table 1 engine support frequencies for several isolator stiffness values are given along with corresponding engine c.g. normalized motion vectors. As can be seen by these data the support frequencies are quite low for the range of $\overline{K}_A$ and L_R for which adequate structure-borne noise isolation can be achieved.

IV. ISOLATOR CONFIGURATIONS AND MECHANICAL PROPERTIES

A. Physical Constraints

The physical constraints placed on the selection of candidate isolator configurations arise from two sources, those due to geometric constraints, i.e., compatibility with the existing engine and engine mount structure and those associated with engine static preloads which must be supported by the isolator. For the laboratory based design it was hoped that several possible candidate isolator configurations could be found from existing stock items available from isolator manufacturers (ref. 8-9) which would require only a minimum of refixturing of existing hardware. A sketch of the dummy rigid engine is given in Figure 19 and a photograph of the forward section of the engine mount structure showing the isolator attachment lugs is given in Figure 20. The engine isolator attachment lugs are 1.27 cm (0.5 in.) thick, 5.08 cm (2.0 in.) wide with a 3.175 cm (1.25 in.) diameter hole and were originally designed to accommodate the 22002-1 soft rubber isolator (ref. 6). The engine mount isolator attachment lugs have an axial separation of 5.38 cm (2.12 in.) and will accommodate an isolator with a radial dimension of approximately 5.0 cm (2.0 in.).

The only isolator preload of interest in the laboratory based evaluation is that due to the engine deadweight. With a dummy engine weight of 170 kilograms (374 lb) the isolator will be subjected to an axial and radial preload in the range of 250 - 340 N (56 - 76 lb). For an inflight design the engine static torque and thrust preloads on the isolators must also be considered, however these preloads were not included in the laboratory simulation.

B. Selection of Candidate Configurations

The selection of candidate isolators which would satisfy the above constraints and lie within the acceptable range of isolator parameters was based on suggestions from isolator manufacturers and the isolator static properties given in available product literature. It should be realized that available isolator data are at most static unidirectional load

deflection curves or a specification of maximum rated load and corresponding deflection at that load (ref. 8-9). To satisfy the requirement that $\overline{K}_A$ be less than 1750 N/cm (1000 lb/in.) would conservatively require that the isolator static stiffness K_A^s be equal to or less than 875 N/cm (500 lb/in.), i.e., a dynamic to static ratio of 2.0. With an axial preload of 340 N (76 lb) the preload deflection would be .386 cm (.15 in.).

Photographs of the isolators and their component parts used in the present investigation are given in Figures 21 and 22. Three of the isolators denoted as Rigid, 3006H, and 22002-1 were isolators used previously to develop the transmission model. The Rigid configuration is a solid steel isolator which provided a rigid link between the engine and engine mount structure. The only local compliance in the system would come from the isolator attachment lugs. The 3006H configuration is the original equipment tube form mounts fitted with a pair of steel collars to pick up loads in the axial direction. The 22002-1 configuration is the soft rubber mount for which the dummy engine isolator attachment lugs were originally designed to accommodate (ref. 8, pp D21-D23). The remaining three isolator configurstions were specifically developed to meet the program design objectives.

The WRB-030M configuration, shown in Figure 22d, is a pair of modified WR4-030 and WB4-030 ring and bushing mounts (ref. 8, pp D25-D27). The mounts are rated at a maximum load of 157 N (36 lb) each. The ring mounts were modified by removing a set (12 each) of the fingers on one side of the mount to allow sufficient penetration of the bushing mount into the engine attachment lug to insure proper alignment during installation. No modification to the existing engine or engine mount structure was necessary for the WRB-030M configuration.

The 22002-11M isolator configuration, shown in Figure 22e, is a modification of the original soft rubber isolator 22002-1. The 22002-1 was modified to increase the isolator axial "rubber wall", i.e., the length of elastomer in axial compression, by adding two additional bushings. The isolator components were cast with a low durometer, high damped elastomer. The manufacturers rated loads of the 22002-1 isolator are 267 N (60 lb) and

178 N (40 lb) in the axial and radial directions, respectively. Thus it was felt that the modified design would be quite adequate in the axial direction with marginal static load capability in the radial direction. It was necessary to modify the engine mount structure to accept the longer isolator by altering the engine mount attachment lugs from the separation distance of 5.38 cm (2.12 in.) out to 9.35 cm (3.68 in.). The installed isolator configuration is shown in Figure 23.

A pair of Multiplane mounts were used in the 206PD-45 isolator configuration. The manufacturers rated load for one of the mounts is 200 N (45 lb) at a deflection of 0.476 cm (.1875 in.) with the axial and radial stiffness being nearly equal (ref. 9, pp A6-A7). From the rated load/deflection data the isolator expected static stiffness would be K_A^S = 840 N/cm (480 lb/in.) which just meets the static stiffness criteria. The 206PD-45 isolator configuration required a modification to the dummy engine isolator attachment arm as is shown in Figure 24.

C. Static Load Deflection Characteristics

Static load-deflection data for each of the three candidate isolator configurations were obtained for unidirectional and bidirectional loading. The data were then used to obtain a measure of the effects of bidirectional loading on the isolators and isolator static stiffness values for later correlation to measured structure-borne interior noise transmission data. The static load-deflection data were obtained using a series of deadweight loadings in the range from 0 to 356 N (80 lb) and deflections were read from a mechanical dial indicator. The bidirectional loading consisted of a static 356 N (80 lb) transverse load to simulate maximum expected static preload of the opposite axis, i.e., radial for loading in the axial direction, etc. The load-deflection curves for the WRB-030M, 22002-11M and 206PD-45 isolator configurations are given in Figures 25 through 27, respectively and the isolator static stiffness values in the 311-356 N (70-80 lb) load range are summarized in Table 2.

As seen in Figure 25, the rapid axial stiffness increase in the WRB-030M configuration indicates an overload of the elastomer placing the

isolator out of the acceptable static stiffness range (below 875 N/cm). The reduced strength of this isolator is attributed to the modifications that were made to accommodate its installation. The softening behavior of the 22002-11M isolator configuration for axial loads above 130 N (30 lb) occurs due to the precompression of the installed isolator being overcome by the applied load. This was intentional to obtain as low as possible axial stiffness which will occur when the engine deadweight exceeds the isolator precompression and the upper elastomer is no longer loaded (see Figure 23). The 206PD-45 isolator configuration in the axial direction was quite unaffected by a radial preload, however the radial axis was quite sensitive to axial preload and nearly doubled in stiffness. In general, the isolator configurations were sensitive to off axis preloads, exhibiting various trends, both increasing and decreasing in stiffness.

It is of interest to note the effects of bidirectional preloads on the isolator static stiffnesses since bidirectional preloading of the isolators was not possible during the dynamic properties tests. It is not known if bidirectional preloads produce similar effects in the isolator dynamic stiffness properties.

D. Isolator Dynamic Properties

As previously discussed, at the onset of the present investigation it was felt that a successful isolator design would require data on the dynamic stiffness properties of the candidate isolators. After searching the open literature it was found that such data was for the most part non-existent. Isolator designs for equipment vibration isolation, in general, use the manufacturers isolator static load-deflection data to determine equipment support frequencies from which single degree of freedom transmissibility characteristics of the system are generated. For the single degree of freedom model, isolation begins when the driving frequency, f_d, equals to $\sqrt{2}\ f_n$, where f_n is the equipment support frequency. Thereafter transmissibility, T, roll off is governed by the expression

$$T^2 = (1 + 4\gamma^2\beta^2)/[(1 - \gamma^2)^2 + 4\gamma^2\beta^2] \qquad (7)$$

where γ is the ratio f_d/f_n and β is the isolator critical damping ratio. For multi degree-of-freedom systems arrays of constant parameter elements are coupled to predict overall system vibration isolation levels.

Material coupon testing is carried out routinely by the isolator manufacturers to determine isolator material properties such as material and loss modulus and to establish fatigue properties of various rubber and elastomeric compounds. These data are generated in the frequency range up through 100 to 200 Hz. Transmissibility testing of configured isolators is usually carried out as a method of quality control to insure a consistent product rather than to obtain isolator stiffness data.

Initially several test arrangements were evaluated to obtain consistent and repeatable isolator stiffness data in the frequency range out to 1000 Hz. Program resources would not allow an indepth study or development of test apparatus and instrumentation for this purpose, however, the test and data analysis procedures as described below were felt to be sufficient for the purposes of the investigation.

Dynamic properties of the isolator configurations were determined using a base excitation, seismic driven, test configuration as is schematically shown in Figure 28. For the test setup the equation of motion is

$$(W/g)A_m + k(1 + i\eta)\ (X_m - X_B) = 0 \qquad (8)$$

where W is the weight of the supported mass, g the gravitational acceleration, k the unknown isolator stiffness, η the unknown isolator material loss factor, X_B the base excitation displacement, and A_m and X_m the supported mass acceleration and displacement, respectively. For harmonic motion, $X_m = -A_m/\omega^2$ and $X_B = -A_B/\omega^2$, where A_B is base excitation acceleration, thus we may write,

$$W(A_m/A_B) - K(1 + i\eta)\ [(A_m/A_B)-1] = 0 \qquad (9)$$

where $K = kg/\omega^2$. (10)

The transmissibility, T, is then written as

$$T = (A_m/A_B) = \frac{K[((K-W)+\eta^2K)^2 + (\eta(K-W)-\eta K)^2]^{1/2}}{[(K-W)^2 + K^2\eta^2]} \exp[i\theta] \qquad (11)$$

where

$$\tan \theta = \frac{[(K-W) - \eta K]}{[(K-W) + \eta^2 K]} \qquad (12)$$

For a given transmissibility ratio T and phase angle θ between A_m and A_B, the above expression may be solved for K and η. For our purposes η is not a strong parameter and was obtained via the amplification ratio at the support mass resonance as

$$\eta = 1./[T^2 - 1.]^{1/2}. \qquad (13)$$

Using the above value of isolator loss factor throughout the frequency range of interest will allow the direct use of Equation (11) in an iterative way, to determine the stiffness at any frequency. The use of Equation (12) was found to yield very inconsistent results due to small changes in phase, θ, beyond the isolator support resonance.

During the isolator property tests a nominal base input acceleration (A_B) of 2 g's was used in the frequency range from 150 to 200 Hz and 5 g's beyond this range. The acceleration amplitude ratio was recorded graphically and digitally via d.c. proportional outputs from an HP3575A amplitude and phase analyzer. Data were nominally recorded in the frequency range 20 to 1000 Hz with the realization that below and just above resonance of the supported mass these procedures may yield erroneous results. Phase changes in these areas occur rapidly and should be taken into account. A frequency sweep rate of 0.2 decade per minute was used throughout the tests.

Transmissibility data for the 22002-1, WRB-030M, 22002-11M and 206PD-45 isolator configurations are given in Figures 29 through 32. In general, wave effects (ref. 10) in the elastomers will cause an apparent increase in stiffness at the higher frequencies, i.e., the β effect, and this phenomena is quite apparent in the axial transmissibility curves shown in Figures 29a through 32a. It was found that higher preloads tend to suppress wave effects and thus support masses near to the expected installed

isolator preloads were used during the dynamic tests for a majority of the isolators. The axial transmissibility curve for the 22002-11M isolator demonstrates the early onset of wave effects due to a relatively light preload for the isolators load capability. The isolator axial stiffness curves were fitted to the design model isolator stiffness spectrum (see Figure 10) by selecting $\overline{K}_A$ as the stiffness value at 100 Hz and determining appropriate β value. The fitted curves are shown by a series of solid dots on the transmissibility/stiffness plots of Figures 29 through 32 and the parameters are listed in Table 3.

The isolator radial transmissibility and computed stiffness curves exhibited a rather odd behavior which was quite repeatable yet could not be traced to a fixture resonance, its origin is still unknown. However, the value of the radial transmissibility curves is the corresponding stiffness values at 100 Hz which were used to determine an L-ratio for the isolator configuration. The L-ratios for the various isolators are listed in Table 3 and the corresponding design model radial stiffnesses based on the L-ratio and β parameters are likewise plotted as a series of solid dots on the radial transmissibility/stiffness plots.

The isolator material loss factors listed in Table 3 are an average of axial and radial loss factors determined from the amplification ratio at the test support mass resonance. The 22002-11M isolator was somewhat nonlinear with respect to excitation amplitude as indicated by the offset in transmissibility when changing amplitudes from 2 to 5 g's, see Figures 31a and 31b. This sensitivity to amplitude was most apparent at the support mass resonance wherein the loss factor increased with increased amplitude. Since the isolator material loss factor was determined to be a very weak parameter with respect to structure-borne noise transmission (see Figures 13 and 16), additional effort to extract more representative loss factor data based on expected isolator excitation levels was not expended.

In general all the isolator configurations exhibited some degree of nonlinearity with respect to support mass weight (preload) and/or excitation amplitude, however within range of expected preload and excitation amplitudes the data listed in Table 3 are considered to be representative of the

installed isolator properties. The only exception is the effect of bidirectional static preload which was indicated by the static load/deflection data presented in Table 2. The summary of isolator dynamic properties given in Table 3 was used to correlate design model predictions to measured structure-borne noise transmission data.

V. ISOLATOR TEST EVALUATION

A. Test Setup

The wings, empennage and interior trim were removed from the test aircraft as shown in the frontispiece. A 1.27 cm plywood bulkhead was installed at Body Station 108 which separated the cabin area from the fuselage aft tail cone. In this configuration the cabin was most sensitive to structure-borne noise transmission and provided a maximum signal to noise ratio for the acoustically untreated laboratory environment.

Three interior microphones were positioned in the aircraft as in the previous sweep tests (see Figure 2), the only possible exception being the longitudinal position of microphone P3 which was mounted on a portable fixed height stand. Maintaining identical positions of the interior response microphones P1, P2, and P3, throughout the model development and during the present investigation was felt to be most important owing to large spatial variations in cabin pressure levels that result from excitation of structural-acoustic resonances in the lower frequency region (ref. 2). Maintaining the positions of P1 and P2 were assured by a cabin mounted fixed microphone rack, however P3 was on a movable stand to allow for storage of aircraft related equipment during periods between tests. Unfortunately there was some question as to the exact forward/aft relocation of P3 during the present investigation and therefore correlation of data with transmission model predictions required removal of P3 from the data for improved correlation as is discussed in Section VI.

Engine excitation was provided by a 7100 N electrodynamic shaker attached to the engine, via a load cell, in the position shown in the frontispiece. This excitation position introduces torsional oscillations of the engine thereby providing a realistic engine excitation. In order to simulate the full spectrum of engine 1/2 rpm harmonics, a terminal peak sawtooth (linear ramp pulse) drive signal was used. The signal was shaped with a series of filters to give a spectrum distribution representative of the design model spectrum given in Figure 8. A 50 millisecond

trace of the simulated engine 2160 rpm excitation time history is given in Figure 33 and in Figure 34 its corresponding Fourier amplitude spectrum. As can be seen, all tones of the fundamental 18 Hz signal are present in the spectrum. One-third octave filters were used to shape the signal which required only minor adjustments for the higher engine speed settings. To minimize direct shaker noise radiation the shaker face was covered with a lead blanket during data acquisition.

B. Data Acquisition and Reduction

The shaker input force and the three interior microphone responses were recorded for each of the five engine speed settings on a 14-channel FM intermediate band magnetic tape for post data analyses. The data were then replayed into an analog to digital conversion system with anti-aliasing filters set at 1250 Hz and digitized at a rate of 4096 samples per second per channel. The data were organized into one-second records and Fourier transformed to the frequency domain (bandwidth of resolution 1.0 Hz). A typical microphone response amplitude spectrum is given in Figure 35; as expected the microphone response is rich in tonal response reflecting the spectral content of the drive signal.

By comparison of the input force spectrum given in Figure 34 to the spectra of Figure 8 it can be seen that the experimental force excitation levels could not be adjusted to the high levels used in the design model. To correct this difference in sources, input force to interior sound pressure level response transfer functions were computed from the time correlated records of the drive and response signals. Since the spectra were primarily discrete tones the transfer functions were computed only at the tones which were precisely identified in the drive signal spectrum. Sample averaging was used via power and cross spectra calculations to enhance the data. The data given in Table 4 demonstrate the stability of the transfer function determination with respect to sample averaging. These data were taken from the rigid isolator configuration. The variation in maximum and minimum transfer function at P1 is shown along with data for P2 and P3 at the corresponding tones. As can be seen by the data in Table 4, the peak transfer functions are well represented using only 1 sample average, i.e.,

a one 1-second record, while the lowest value transfer function shows some variation due to interference background noise. Three sample averages were used for all data presented in this report.

C. Analysis and Results

1. Transfer Functions

It is instructive to compare the transfer function data taken from the continuous sweep method used for the design model correlation studies (ref. 6) to the multiple tone excitation of the present investigation. During the previous sweep tests a constant input force of 89 N_{rms} was used with a sweep rate of 2.0 Hz/second from 10 - 1000 Hz. At the time it was determined that 2.0 Hz/second was the fastest sweep rate allowed without loss of peak response in the lower frequency range. A comparison of SPL transfer function data taken from continuous sweep and multiple tone excitations are presented in Figures 36 through 38. In Figure 36 a comparison of SPL transfer function data is given for the rigid isolator configuration. Initially, it appears that the sweep rate used on the previous investigation may have been considerably faster than required to capture the interior response. However, transfer function data for the 22002-1 soft rubber mounts, as given in Figures 37 and 38 show quite improved agreement between the two methods of excitation. The reason for the discrepancies in the transfer functions generated for the rigid isolators is not known. Excessive sweep rate is a possible candidate since much sharper responses are expected for the rigid isolators which do not contribute to system damping. There is also the possibility of nonlinear response during the multiple tone excitation due to the use of somewhat higher excitation force levels than used during the continuous sweep tests. Time would not allow pursuit of this phenomena, however the data suggest that when obtaining transfer function data of this nature that appropriate force excitation levels and spectral content, relative to expected responses, be used to insure accurate representation.

2. Facility Noise Floor

To determine if a facility noise floor was reached during the isolator evaluations a special airborne configuration run was made. The

dummy engine was connected to the shaker and supported by a "sky hook", an overhead crane, while the tire pressure in the aircraft was reduced to lower the aircraft to its engine installed attitude. In effect, the structure-borne noise path was cut and the airborne noise path reconstructed as in the isolator installed configurations. The only difference in the configurations would be the engine static loading effects on the fuselage airframe response. Transfer function data were obtained at each of the five engine speed settings and interior noise spectra computed based on the force excitation levels used in the design model evaluations, the airborne noise levels are given in Table 5. Two sets of overall sound pressure levels are given in Table 5, P12 are the maximum OASPL levels when P3 is removed from the data and P123 considers all three microphone responses. The airborne component levels were considered sufficiently high to warrant removal of this component from the isolator data. This was accomplished by comparing at each tone in the spectra the measured airborne and isolator data components at each microphone location. If the isolator data were 6 dB greater than the airborne component the two levels were substracted to obtain the structure-borne component. The spectrum frequency at which the isolator data were less than 6 dB above the airborne component was considered to be the useful frequency range of measured data and all data above that frequency were no longer considered in the OASPL computations.

3. Overall Sound Pressure Level Data

Recall that the multiple tone input force spectra in the transmission model was adjusted to yield the measured structure-borne noise level data obtained from engine attached/detached engine running tests. The specific configuration was interior removed, engine speed 2160 rpm, and original equipment 3006H tube mounts installed. For the purpose of direct comparison of laboratory data to the transmission model predictions all laboratory data were adjusted via the recorded transfer functions to reflect the transmission model input force spectra. All data were also adjusted for influences of the measured airborne noise components, as previously described. The resulting maximum overall sound pressure level data P123 and P12 are listed in Tables 6 and 7, respectively. In these tables unweighted and

A-weighted OASPL data are given for both uncorrected, combined airborne and structure-borne (AB + SB), spectra and corrected, structure-borne alone (SB), spectra. The one-third octave band beyond which the measured data were no longer 6 dB above the airborne noise levels, f_{BAND}, is also given in Tables 6 and 7 to indicate the useful range of measurement for the given isolator configuration.

As can be seen by the data listed in Tables 6 and 7 the airborne noise transmission did not greatly influence the unweighted OASPL data, however, it had a noticeable influence on the A-weighted levels, particularly for the softer isolator configurations which exhibited overall lower transmission levels. It is of interest to note that the rigid isolator configuration data were for the most part unaffected by the airborne noise corrections and therefore the rigid isolator correction factors applied to the transmission model (reference Section II.B) cannot be attributed to airborne noise contamination. During the present investigation uncorrected data were retained out to the 800 Hz one-third octave band (maximum 891 Hz). Data in the 1000 Hz band were contaminated by a structural resonance of the "rigid" engine and therefore removed from consideration since flexibility of the engine was not included in the transmission model.

By comparing the maximum unweighted OASPL levels of 116.7 dB (P123) and 108. dB (P12) for the original equipment isolators, 3006H, to the maximum levels of 106.3 dB (P123) and 97.8 dB (P12) for the 206PD-45 isolator configuration it can be seen that 10.4 dB (P123) and 11.0 dB (P12) noise level reductions were accomplished during the investigation. Likewise A-weighted noise level reductions of 11.7 dBA (P123) and 11.2 dBA (P12) were realized. These levels fell short of the 15 dB design goal originally set in the program and therefore a more detailed review of the data will now be given in an attempt to determine an area where imporvement of the design procedures may be made.

In Tables 8 and 9 the unweighted and A-weighted OASPL at the individual microphone locations are listed for all isolator configurations and engine speeds along with maximum levels P123 and P12, respectively. As can be seen by these data the maximum unweighted interior levels are for the most part

dominated by the response at P3, the aft cabin microphone, while responses at P1 and P2 are measurably lower and of more or less equal level. The variation in OASPL at the individual microphone locations with engine speed is given graphically in Figures 39 and 40 for the unweighted and A-weighted response, respectively. Figure 39 clearly shows the dominance of P3 in the unweighted levels for a majority of the isolator configurations, while the data in Figure 40 show that the responses at P1 and P2 control a majority of the A-weighted levels. As previously discussed, there was some question as to the proper replacement of the P3 microphone during the present investigation and with the unweighted levels being dominated by the response at P3 all data were re-analyzed with P3 removed, giving rise to the P12 data. Additional discussion on the importance of the position of the P3 microphone will be given below in Section V.C.4.

The correlation of measured maximum OASPL levels, P123, to engine deflection due to static torque, reference 50.8 cm (20 in.) arm, is given in Figure 41 for both unweighted and A-weighted spectrum levels. The deflection data given in Figure 41 are taken from the data listed in Table 3. The linear regression correlation coefficient, R, and regression line for the data are given in the figure. Linear regression of the unweighted data resulted in a regression coefficient of -0.83 indicating reasonable data correlation to the linear curve fit. Linear correlation of the measured A-weighted OASPL data to engine static displacement resulted in a correlation coefficient of R = -0.40, which indicates very poor correlation, as can be seen directly by the data in Figure 41. The engine static deflection was used as a correlating parameter for the data since this parameter represents a potential system design constraint. Due to the direct relationship between engine displacement, X_e, and the isolator axial static stiffness K_A^s, reference Equation (4), the data of Figure 41 can be viewed as a correlation of measured OASPL to isolator axial static stiffness. In Figure 42 a linear correlation of the measured OASPL data to the measured dynamic axial stiffness at 100 Hz, $\overline{K}_A$, is presented. The linear correlation coefficients of 0.83 and 0.74 for the unweighted and A-weighted OASPL data, respectively, indicate improved correlation of the noise data when using the dynamic stiffness, for the A-weighted OASPL data.

4. Sound Pressure Level Spectra

Typical comparisons of one-third octave maximum sound pressure level spectra for various isolator configurations are given in Figures 43 and 44, for engine speeds of 2160 rpm and 2640 rpm, respectively. The fundamental engine 1/2 rpm harmonics corresponding to the engine speeds of 2160 and 2640 rpm are 18 and 22 Hz and therefore there was no excitation in the 63 and 50 Hz one-third octave bands as is shown by the data in Figures 43 and 44, respectively. In general, decreasing the isolator stiffness decreases structure-borne noise transmission throughout the spectrum, however not necessarily uniformly. As expected, the largest decrease in noise transmission occurred when going from the rigid isolator configuration to the original equipment 3006H isolator configuration, however the exceptionally large difference obtained at the simulated engine speed of 2640 rpm was quite surprising. For the non-rigid isolator configurations the unweighted spectra are dominated by the response in the 80 Hz one-third octave band. The 80 Hz band spans the frequency range from 70.8 to 89.1 Hz and thus contains the fourth engine harmonic (72 to 88 Hz) which has the highest drive level of any tone in the input drive spectrum (ref. Figure 8).

With the maximum structure-borne noise spectrum, P123, being dominated by the response of P3 at a single tone, the importance of correct repositioning of microphone P3 is established. Maximum P123 OASPL levels for the original equipment 3006H and 206PD-45 isolators occurred at a simulated engine speed of 2280 rpm, reference data in Table 8. Effect of removing the response of P3 from the maximum OASPL levels can be seen by the spectra plotted in Figure 45. In the 80 Hz band a decrease of 14 dB occurs when P3 is removed from the data resulting in a 8-10 dB reduction in overall spectrum levels. We may also note that the removal of P3 has very little influence on the measured SPL above the 80 Hz band.

At a simulated engine speed of 2280 rpm the engine fourth excitation harmonic occurs at 76 Hz. A comparison of transfer function data at P3 obtained during the transmission model development with the present transfer function levels obtained via multiple pure tone excitation was given in Figure 38. This data clearly shows a 6-8 dB difference in transfer function

level for the 22002-1 isolator configuration at 76 Hz which indicates a possible error in relocating the P3 microphone during the present isolator evaluations. If this is in fact the case, one should expect better correlation of the transmission model predictions with the P12 data, wherein P3 is removed, that with the P123 data.

VI. COMPARISON OF TEST RESULTS WITH DESIGN

A. Design Curves

A plot of predicted unweighted overall sound pressure levels versus isolator dynamic stiffness at a 100 Hz, $\overline{K}_A$, for L-ratios of 2.0 and 5.0, as taken from the design curve of Figure 11, is given in Figure 46 along with measured maximum P123 OASPL values for each of the isolator configurations. The isolator stiffness values were taken from the measured values listed in Table 3 and the maximum OASPL responses obtained from data listed in Table 6. The trend of the measured data follows the design curve trend, the only major exception being the WRB-030M configuration, however the measured data fall approximately 6 to 8 dB higher than the design curve predictions. To what extent the influence of removing P3 from the measured data would have on the predicted design curves will now be discussed.

B. Design Model Predictions

The measured isolator properties in the form of the design model parameters ($\overline{K}_A$, β, L_R, and η, as taken from Table 3) were used in the design model to generate predictions for direct comparison to the measured OASPL data. The measured and predicted unweighted and A-weighted P123 OASPL values for each of the isolator configurations at each of the five engine speeds are listed in Table 10. The predicted OASPL levels reflect the limited frequency range of the measured data, reference Table 6. Correlation plots of the data are given in Figures 47 and 48 for the unweighted and A-weighted levels, respectively. The data correlations show the design model to be mainly unconservative with isolator configurations WRM-030M and 206PD-45 exhibiting maximum deviations from the predicted levels. The A-weighted levels show improved correlation with the design model predictions, mainly due to the reduced influence of the dominate low frequency contributions (80 Hz band).

The effect of removing the P3 microphone response from the model predictions and measured data are shown in the data listed in Table 11. The corresponding correlation plots are given in Figures 49 and 50 for the unweighted and A-weighted OASPL P12 data, respectively. As can be seen the

correlation of predicted to measured values noticeably improved with a conservative trend in the predicted levels. The WRB-030M and 206PD-45 isolator configurations were again unconservatively predicted however, much improved as compared to the predictions using all three microphones. Again the A-weighted spectrum levels show improved correlation over that of the unweighted values. From these data it was concluded that the P3 microphone was not in the same position during the isolator evaluations as it was during the transmission model development and therefore the data correlations using P12 are more representative of the predictive capabilities of the design model.

It is of interest to note that the WRB-030M and 206PD-45 isolators were configured from much smaller volumes of elastomeric material than the other soft isolators (22002-1 and 22002-11M) and thus the level of dynamic strain per unit volume of elastomer would naturally be much higher. Thus, the potential for these isolators to operate in a region of nonlinear elastic response due to excessive strain is much increased over that of the larger isolators. Again note that the effects of bidirectional static loading on the dynamic properties of the isolators could not be determined and therefore may have been the reason for poor correlation of the WRB-030M and 206PD-45 isolators.

VII. CONCLUSIONS

An engine induced structure-borne interior noise transmission model for a single engine general aviation aircraft was used to develop a set of retrofit vibration isolator design curves for reduced interior noise transmission. Several candidate isolator configurations were developed with the design objective of a 15 dB decrease in overall structure-borne interior noise transmission over that of the aircraft's original equipment isolators. Results from laboratory test evaluation of the candidate isolator configurations, using simulated pure tone engine excitation, support the following conclusions.

1) Overall maximum interior noise level reductions on the order of 10 dB were realized from the candidate isolators when considering both forward and aft cabin noise levels.

2) The structure-borne noise transmission model used in the isolator design specification was adequate for assessing the trends in improved structure-borne noise isolation for a given change in isolator dynamic properties.

If the transmission model development and isolator design procedures as employed in this report are to be used for retrofit isolator design, the following observations and recommendations should be taken into consideration to insure success of the overall program.

1) The potential for nonlinear response in lightweight structure typical of general aviation fuselage construction appears to warrant some caution when developing the fuselage empirical data bank. Force level excitations should be considered which are representative of actual imposed loading, both in magnitude and spectral content. The multiple pure tones produced by a filtered terminal peak sawtooth, as used on the present investigation, appears to be a good representation for propeller driven aircraft. Shaker force limitations

will, however, generally limit the spectral width of the excitation.

2) The importance of rotational degrees of freedom at structural interfaces for the transmission of vibration/noise should be taken into consideration especially at the higher frequencies (beyond 250 Hz).

3) Since dynamic properties of the isolators control interior noise transmission while their static properties control overall engine motion, representative mechanical properties of the isolators, both static and dynamic, must be specified to insure an adequate design evaluation. The dynamic properties of elastomeric isolators, under installed preloads and excitation levels, do not operate as linear single degree of freedom systems. Methods for the evaluation of the dynamic properties of isolators is one area that will require additional research if improved correlation between design model predictions and actual isolator performance is to be expected. However, relative to the knowledge of actual engine input force characterization, the use of representative isolator parameters such as dynamic stiffness at 100 Hz, $\overline{K}_A$, frequency hardening effect, β, and axial to radial stiffness, L-ratio, may be quite sufficient for improved isolator design.

REFERENCES

1. Unruh, J.F., and Scheidt, D.C.: "Engine Induced Structural-Borne Noise in a General Aviation Aircraft," SAE Transactions Paper No. 790626, Vol. 88, pp 2171-2184, 1980.

2. Unruh, J.F., Scheidt, D.C., and Pomerening, D.J.: "Engine Induced Structural-Borne Noise in a General Aviation Aircraft," NASA CR-159099, August, 1979.

3. Unruh, J.F.: "Finite Element Subvolume Technique for Structure-Borne Interior Noise Prediction," AIAA Journal of Aircraft, Vol. 17, No. 6, June 1980.

4. Unruh, J.F.: "Structure-Borne Noise Prediction for a Single Engine General Aviation Aircraft," AIAA Journal of Aircraft, Vol. 18, No. 8, August, 1981.

5. Unruh, J.F., and Scheidt, D.C.: "Engine Isolation for Structure-Borne Interior Noise Reduction in a General Aviation Aircraft," NASA CR-3427, SwRI Project 02-4860, May 1981.

6. Unruh, J.F.: "Procedure for Evaluation of Engine Isolators for Reduced Structure-Borne Interior Noise Transmissions," Paper No. 81-1970, AIAA 7th Aeroacoustics Conference, Palo Alto, Calif., October 1981.

7. "Cessna 1963 Model 172D, Skyhawk and Powermatic Series Owner's Manual," Cessna Aircraft Company, Wichita, Kansas, August, 1975.

8. Barry Controls: "Application Selection Guide-Vibration, Shock, Noise," Product Literature, Division of Barry Wright Corp., 700 Pleasant St., Watertown, MA 02172.

9. Lord Kinematics: "Vibration/Shock/Noise Control Products, Elastomeric Flexible Couplings, Bonded and Molded Elastomers," Product Literature, Lord Corporation, 1635 West 12th Street, Erie, PA 16514.

10. Snowdon, J.C.: "Handbook of Vibration and Noise Control," Report No. AD/A-071 485, Applied Research Laboratory, Penn. State University, April 1979.

TABLE 1. ENGINE SUPPORT FREQUENCIES

L_R	$\bar{K}_A$ ~ N/cm (lb/in.)			C.G. MOTION VECTOR					
	1750 (1000)	1300(750)	875(500)	x	y	z	θ_x	θ_y	θ_z
0.25	3.44	2.98	2.44		1.0		-0.08		
	4.39	3.80	3.10	1.0		-0.07		0.04	
	7.85	6.80	5.55	0.21		1.0		-0.05	
	8.36	7.24	5.91		-0.11		0.12		1.0
	9.26	8.02	6.55	-0.70		1.0		0.25	
	24.49	21.21	17.32		1.0		0.79		-0.02
2.0	8.69	7.53	6.14	1.0		-0.24		0.10	
	9.63	8.34	6.81		1.0		-0.09		0.01
	12.58	10.90	8.90	0.19		1.0		0.01	
	15.64	13.55	11.06		-0.43		0.24		1.0
	19.80	17.15	14.00	1.0		-0.11		-0.14	
	24.71	21.40	17.47		1.0		0.67		-0.03
5.0	12.53	10.85	8.86	1.0		-0.28		0.11	
	14.91	12.91	10.54		1.0		-0.13		0.01
	17.84	15.45	12.61	0.18		1.0		0.01	
	23.06	19.97	16.31		0.98		0.91		1.0
	25.51	22.10	18.04		1.0		0.45		-0.09
	30.63	26.53	21.66	1.0		-0.08		-0.12	

TABLE 2. ISOLATOR STATIC STIFFNESS VALUES
IN 311-356 N (70-80 lb) LOAD RANGE

ISOLATOR CONFIGURATION	Stiffness ~ N/cm (lb/in)	
	Unidirectional Loading	Bidirectional Loading 356 N (80 lb)
WRB-030M		
Axial	1280. (730.)	1350. (770)
Radial	2330. (1330.)	3500. (2000)
22002-11M		
Axial	325. (183.)	515. (295)
Radial	3500. (2000.)	1840. (1050)
206PD-45		
Axial	650. (370.)	650. (370)
Radial	935. (535.)	1750. (1000)

TABLE 3. ISOLATOR DYNAMIC PROPERTIES TAKEN FROM TEST DATA

ISOLATOR CONFIGURATION	$\overline{K}_A$[1] N/cm	(lb/in)	L_R[2]	β	η	X_e[3] cm	(in.)	K_A^S N/cm	(lb/in)
RIGID[4]	52,535	(30000)	8.0	1.0	0.0	.015	(.006)	52,535	(30000)
3006H[5]	8055	(4600)	8.0	1.0	0.10	.173	(.068)	4640	(2650)
22002-1	4115	(2350)	0.98	2.3	0.10	.368	(.145)	2190	(1250)
WRB-030M	2225	(1270)	2.52	5.0	0.16	.597	(.235)	1350	(770)
22002-11M	3325	(1900)	6.84	5.0	0.31	1.56	(.614)	515	(295)
206PD-45	1315	(750)	1.47	5.0	0.10	1.24	(.489)	650	(370)

[1] Effective Axial Stiffness for frequency dependent model

$$K_A = \overline{K}_A \begin{cases} 1 & f \le 100 \\ [100-\beta + (\beta-1)f^2/10000.]/99. & 100 \le f \le 1000 \end{cases}$$

[2] Effective Radial Stiffness computed as $K_R = L_R \cdot K_A$.

[3] Engine deflection at an arm of 50.8 cm (20 in.) due to Maximum Static Torque, ref. Equation (4).

[4] Computed based on Local compliance of engine mount isolator attachment lugs.

[5] Not tested, properties reflect dynamic to static ratio of 1.7, L_R taken from product literature.

TABLE 4. VARIATION OF SPL TRANSFER FUNCTIONS WITH SAMPLE AVERAGES, RIGID ISOLATORS, 2160 RPM

Tone Hz	Sample Averages	Response Microphone P1	P2	P3
144.	1	106.99	106.36	98.61
	3	107.03	106.36	98.53
	5	107.14	106.57	98.66
594.	1	60.33	82.68	72.36
	3	62.61	81.43	76.17
	5	57.48	81.65	76.84

TABLE 5. MEASURED TEST FACILITY AIRBORNE NOISE LEVELS

Engine Speed	Unweighted OASPL - dB		A-Weighted OASPL - dBA	
	P12	P123	P12	P123
2160	88.7	89.6	86.5	87.3
2280	89.1	90.1	86.3	87.0
2400	89.7	91.1	84.7	85.6
2520	89.1	90.4	85.4	86.3
2640	89.2	91.5	85.3	86.7

TABLE 6. COMPARISON OF MEASURED PEAK P123 OVERALL SOUND PRESSURE LEVELS WITH AND WITHOUT AIRBORNE COMPONENT REMOVED

Configuration	RPM	Unweighted P123 dB		A-Weighted-P123 - dBA		f_{BAND} Hz
		AB*+SB*	SB	AB+SB	SB	
3006H	2160	111.6	111.2	99.2	94.7	500
	2280	116.8	116.7	99.7	96.4	630
	2400	113.0	112.6	100.4	93.3	250
	2520	112.3	111.6	101.5	95.3	250
	2640	112.4	111.9	100.8	96.8	500
Rigid	2160	129.7	129.7	114.7	114.5	800
	2280	129.5	129.5	109.1	108.8	800
	2400	124.0	123.9	109.4	109.2	800
	2520	121.8	121.7	106.8	106.4	800
	2640	134.5	134.5	125.0	124.9	800
22002-1	2160	104.3	103.7	91.3	89.1	500
	2280	113.1	113.0	92.7	91.1	315
	2400	108.2	107.9	91.3	87.6	200
	2520	106.1	105.4	91.3	87.5	200
	2640	106.2	105.6	91.6	88.3	400
WRB-030M	2160	106.9	106.5	92.8	91.1	315
	2280	114.2	114.1	94.1	92.4	200
	2400	110.6	110.3	92.1	89.8	200
	2520	109.7	109.3	96.1	94.7	250
	2640	104.6	104.0	92.8	90.2	250
22002-11M	2160	108.2	107.9	92.0	89.3	315
	2280	110.8	110.7	92.2	90.2	250
	2400	109.7	109.4	95.2	93.6	250
	2520	108.8	108.3	94.6	92.2	250
	2640	108.4	107.9	96.9	95.8	250
206PD-45	2160	98.6	96.7	90.5	81.2	200
	2280	106.6	106.3	90.5	85.1	250
	2400	105.0	104.3	91.0	83.3	200
	2520	103.2	101.8	94.1	84.2	200
	2640	101.3	99.7	90.8	84.3	315

*AB ~ Airborne Noise
SB ~ Structure-borne Noise

TABLE 7. COMPARISON OF MEASURED PEAK P12 OVERALL SOUND PRESSURE LEVELS WITH AND WITHOUT AIRBORNE COMPONENTS REMOVED

Configuration	RPM	Unweighted P12 ~ dB		A-Weighted P12-dBA		f_{BAND}
		AB*+SB*	SB	AB+SB	SB	Hz
3006H	2160	106.7	105.7	98.6	93.5	500
	2280	106.4	105.4	98.6	93.7	500
	2400	108.2	107.0	99.9	91.3	250
	2520	106.3	104.0	101.1	94.2	250
	2640	108.8	108.0	100.1	95.0	500
Rigid	2160	127.9	127.8	114.3	114.2	800
	2280	117.3	117.2	105.7	105.2	800
	2400	120.4	120.3	108.6	108.3	800
	2520	118.4	118.3	105.9	104.8	800
	2640	132.9	132.9	122.5	122.5	800
22002-1	2160	101.7	100.9	90.3	87.5	315
	2280	102.8	102.0	89.9	86.5	315
	2400	103.0	102.3	89.7	85.1	200
	2520	100.5	99.1	90.0	86.0	200
	2640	103.1	102.3	91.0	87.2	315
WRB-030M	2160	102.8	102.1	91.5	89.6	250
	2280	104.1	103.1	91.4	88.0	200
	2400	104.7	103.1	90.5	80.5	100
	2520	104.8	104.2	95.5	94.2	250
	2640	104.5	103.9	92.6	90.2	250
22002-11M	2160	102.0	101.1	91.2	88.1	250
	2280	100.4	99.4	90.2	87.2	250
	2400	105.9	105.4	94.6	92.9	250
	2520	103.0	101.9	93.7	91.2	250
	2640	107.2	106.7	96.6	95.7	250
206PD-45	2160	96.7	94.4	89.9	79.8	200
	2280	98.1	96.1	88.8	81.6	250
	2400	98.7	97.1	89.2	79.0	200
	2520	98.4	94.1	93.8	82.3	200
	2640	99.3	97.8	89.9	83.8	315

*AB ~ Airborne
SB ~ Structure-borne

TABLE 8. MEASURED OVERALL SOUND PRESSURE LEVELS, ALL MICROPHONES ACTIVE, AIRBORNE COMPONENTS REMOVED

Configuration	RPM	Unweighted OASPL ~ dB				A-Weighted OASPL ~ dBA			
		P1	P2	P3	P123	P1	P2	P3	P123
3006H	2160	104.4	104.6	110.8	111.2	92.0	92.3	92.4	94.7
	2280	104.8	103.7	116.6	116.7	92.9	91.5	94.7	96.4
	2400	103.2	106.5	112.4	112.6	89.1	89.7	91.8	93.3
	2520	102.8	102.8	111.1	111.6	93.5	92.6	91.3	95.3
	2640	105.1	107.7	111.5	111.9	92.7	94.1	94.6	96.8
Rigid	2160	127.8	127.0	126.4	129.7	113.8	113.4	109.0	114.5
	2280	113.7	117.1	129.4	129.5	103.2	104.6	107.5	108.8
	2400	119.9	117.8	122.6	123.9	107.0	106.4	105.6	109.2
	2520	117.8	113.0	121.1	121.7	103.2	103.8	103.2	106.4
	2640	132.3	132.3	131.8	134.5	121.6	121.8	123.6	124.9
22002-1	2160	99.1	99.2	102.0	103.7	86.4	84.5	85.8	89.1
	2280	102.0	98.9	112.9	113.0	86.3	82.4	90.0	91.1
	2400	97.5	101.7	107.7	107.9	82.1	82.7	85.8	87.6
	2520	97.5	97.4	104.8	105.4	85.8	82.7	83.7	87.5
	2640	96.2	102.0	105.2	105.6	83.0	86.6	85.1	88.3
WRB-030M	2160	100.7	100.9	105.8	106.5	88.7	87.9	88.7	91.1
	2280	103.0	100.0	114.0	114.1	87.9	84.6	90.8	92.4
	2400	99.7	103.6	110.2	110.3	84.0	85.2	88.3	89.8
	2520	103.7	102.6	108.0	109.3	94.0	92.5	86.3	94.7
	2640	102.5	103.8	102.0	104.0	87.0	89.6	83.0	90.2
22002-11M	2160	99.4	100.5	107.5	107.9	85.3	87.1	86.0	89.3
	2280	98.7	99.0	110.6	110.7	86.1	86.7	88.5	90.2
	2400	102.8	104.8	108.6	109.4	89.8	91.7	88.3	93.6
	2520	100.6	101.4	107.7	108.3	90.9	90.5	86.6	92.2
	2640	103.1	106.3	105.2	107.9	91.6	95.0	88.7	95.8
206PD-45	2160	93.5	92.3	95.0	96.7	79.3	76.3	77.8	81.2
	2280	95.4	93.9	106.2	106.3	81.0	78.5	83.5	85.1
	2400	94.0	96.6	104.2	104.3	77.8	77.0	82.0	83.3
	2520	93.4	91.2	101.3	101.8	82.2	77.6	80.9	84.2
	2640	91.7	97.8	99.0	99.7	74.6	83.8	79.1	84.3

TABLE 9. MEASURED OVERALL SOUND PRESSURE LEVELS, P1 AND P2 ACTIVE, AIRBORNE COMPONENTS REMOVED

Configuration	RPM	Unweighted OASPL ~ dB			A-Weighted OASPL ~ dBA		
		P1	P2	P12	P1	P2	P12
3006H	2160	104.4	104.6	105.7	92.0	92.3	93.5
	2280	104.8	103.7	105.4	92.9	91.5	93.7
	2400	103.2	106.5	107.0	89.1	89.7	91.3
	2520	102.8	102.8	104.0	93.5	92.6	94.2
	2640	105.1	107.7	108.0	92.7	94.1	95.0
Rigid	2160	127.8	127.0	127.8	113.8	113.4	114.2
	2280	113.7	117.1	117.2	103.2	104.6	105.2
	2400	119.9	117.8	120.3	107.0	106.4	108.3
	2520	117.8	112.9	118.3	102.8	103.0	104.8
	2640	132.3	132.3	132.9	121.6	121.8	122.5
22002-1	2160	99.1	99.2	100.9	86.3	84.2	87.5
	2280	102.0	98.9	102.0	86.3	82.4	86.5
	2400	97.5	101.7	102.3	82.1	82.7	85.1
	2520	97.5	97.4	99.1	85.8	82.7	86.0
	2640	96.1	102.0	102.3	83.0	86.6	87.2
WRB-030M	2160	100.7	100.9	102.1	88.7	87.9	89.6
	2280	103.0	100.0	103.1	87.9	84.6	88.0
	2400	97.3	103.1	103.1	74.8	80.4	80.5
	2520	103.7	102.6	104.2	94.0	92.5	94.2
	2640	102.5	103.8	103.9	87.0	89.6	90.2
22002-11M	2160	99.4	100.5	101.1	85.3	87.1	88.1
	2280	98.7	99.0	99.4	86.1	86.7	87.2
	2400	102.8	104.8	105.4	89.8	91.7	92.9
	2520	100.6	101.4	101.9	90.9	90.5	91.2
	2640	103.1	106.3	106.7	91.6	95.0	95.7
206PD-45	2160	93.5	92.3	94.4	79.3	76.3	79.8
	2280	95.4	93.9	96.1	81.0	78.5	81.6
	2400	94.0	96.6	97.1	77.8	77.0	79.0
	2520	93.4	91.2	94.1	82.2	77.6	82.3
	2640	91.7	97.8	97.8	74.6	83.8	83.8

TABLE 10. COMPARISON OF MEASURED STRUCTURE-BORNE NOISE TRANSMISSION OASPL TO DESIGN MODEL PREDICTIONS FOR P123

Configuration	RPM	Unweighted P123 OASPL ~ dB		A-Weighted P123 OASPL ~ dBA	
		Measured	Predicted	Measured	Predicted
3006H	2160	111.2	108.4	94.7	92.9
	2280	116.7	108.9	96.4	93.9
	2400	112.6	110.3	93.3	99.7
	2520	111.6	108.0	95.3	93.1
	2640	111.9	111.1	96.8	102.1
Rigid	2160	129.7	122.8	114.5	111.4
	2280	129.5	120.3	108.8	108.5
	2400	123.9	130.5	109.2	120.5
	2520	121.7	123.5	106.4	111.5
	2640	134.5	132.4	124.9	122.2
22002-1	2160	103.7	106.2	89.1	93.4
	2280	113.0	100.2	91.1	81.5
	2400	107.9	106.0	87.6	89.9
	2520	105.4	103.8	87.5	87.2
	2640	105.6	104.0	88.3	88.0
WRB-030M	2160	106.5	96.2	91.1	84.0
	2280	114.1	95.2	92.4	76.9
	2400	110.3	97.9	89.8	78.9
	2520	109.3	99.5	94.7	87.2
	2640	104.0	98.7	90.2	85.0
22002-11M	2160	107.9	104.4	89.3	91.8
	2280	110.7	102.3	90.2	87.9
	2400	109.4	105.3	93.6	95.6
	2520	108.3	104.5	92.2	93.1
	2640	107.9	106.3	95.8	95.4
206PD-45	2160	96.7	92.9	81.2	79.0
	2280	106.3	90.0	85.1	71.1
	2400	104.3	95.1	83.3	76.8
	2520	101.8	93.2	84.2	74.5
	2640	99.7	93.4	84.3	77.9

TABLE 11. COMPARISON OF MEASURED STRUCTURE-BORNE NOISE TRANSMISSION OASPL TO DESIGN MODEL PREDICTIONS FOR P12

Configuration	RPM	Unweighted P12 OASPL dB		A-Weighted P12 OASPL dBA	
		Measured	Predicted	Measured	Predicted
3006H	2160	105.7	108.2	93.5	92.4
	2280	105.4	105.4	93.7	93.0
	2400	107.0	110.3	91.3	99.7
	2520	104.0	107.9	94.2	93.1
	2640	108.0	110.8	95.0	101.2
Rigid	2160	127.8	122.7	114.2	111.0
	2280	117.2	117.0	105.2	107.8
	2400	120.3	130.4	108.3	120.8
	2520	118.3	122.3	104.8	110.8
	2640	132.9	131.8	122.5	122.0
22002-1	2160	100.9	103.1	87.5	90.7
	2280	102.0	96.6	86.5	79.7
	2400	102.3	99.5	85.1	86.8
	2520	99.1	101.4	86.0	86.6
	2640	102.3	99.7	87.2	85.4
WRB-030M	2160	102.1	95.1	89.6	83.2
	2280	103.1	88.4	88.0	75.6
	2400	103.1	90.3	80.5	67.9
	2520	104.2	97.9	94.2	87.1
	2640	103.9	95.7	90.2	84.2
22002-11M	2160	101.1	104.2	88.1	91.6
	2280	99.4	99.7	87.2	87.6
	2400	105.4	105.2	92.9	95.6
	2520	101.9	104.5	91.2	93.1
	2640	106.7	105.6	95.7	95.2
206PD-45	2160	94.4	88.0	79.8	73.7
	2280	96.1	83.1	81.6	69.7
	2400	97.1	86.7	79.0	71.9
	2520	94.1	90.4	82.3	73.3
	2640	97.8	90.0	83.8	76.6

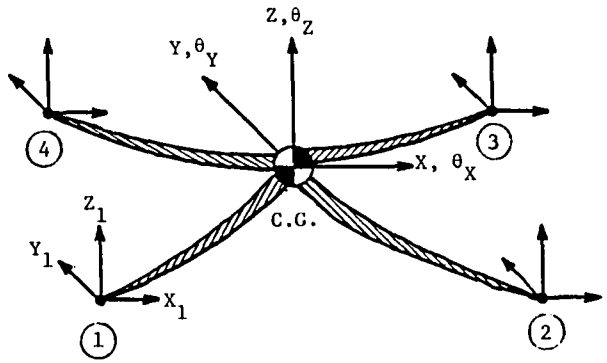

a) Engine ~ Rigid Body

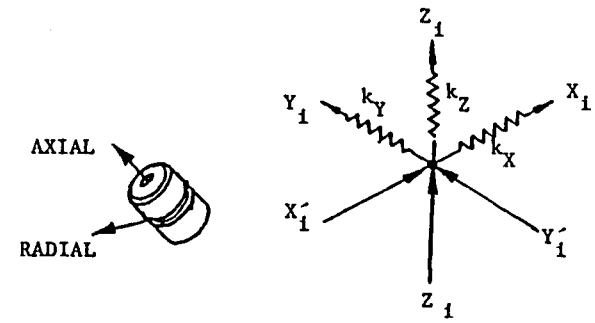

b) Vibration isolators ~ Translational Springs

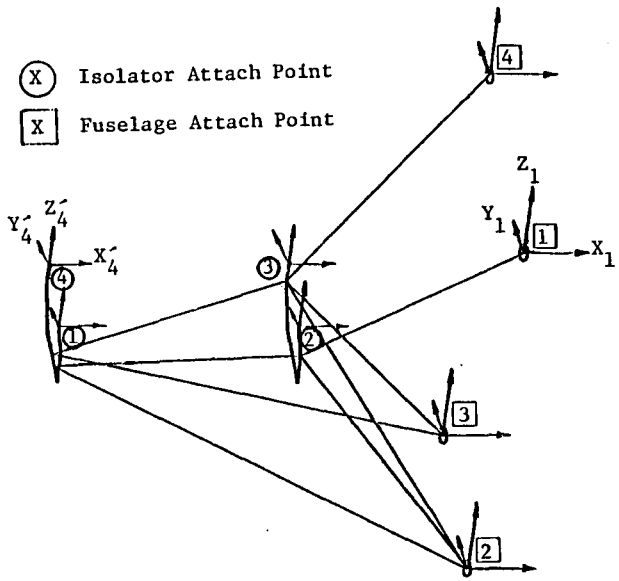

c) Engine mount structure ~ F.E. Model

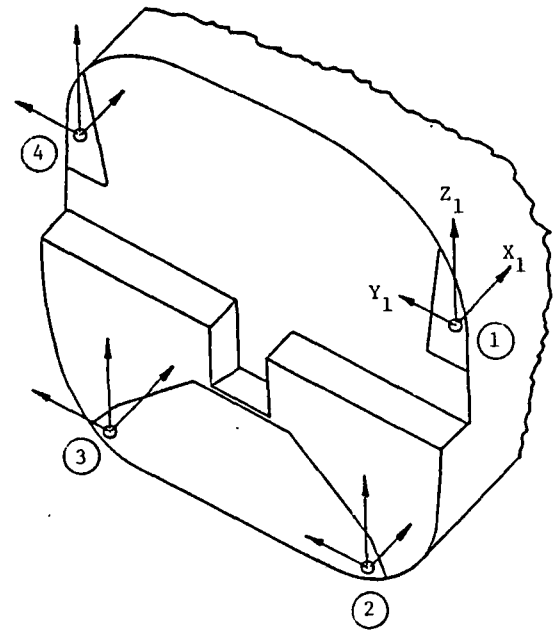

d) Firewall and cabin ~ Empirical Data Base

Figure 1. Components Of The Noise Transmission Model.

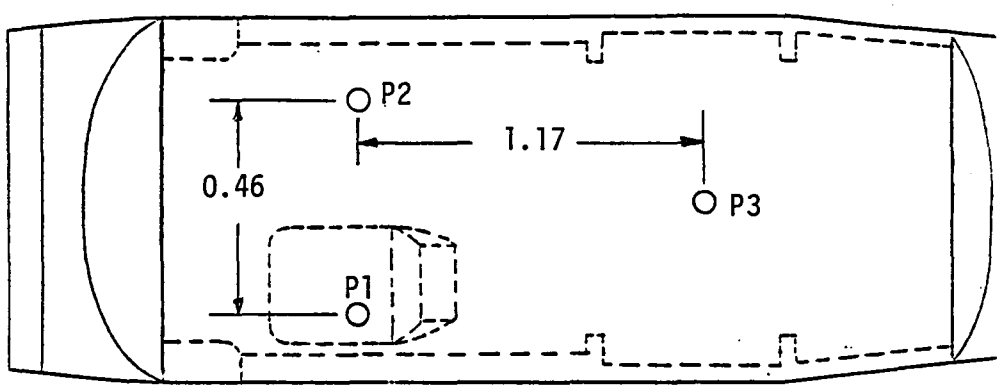

a) Top View

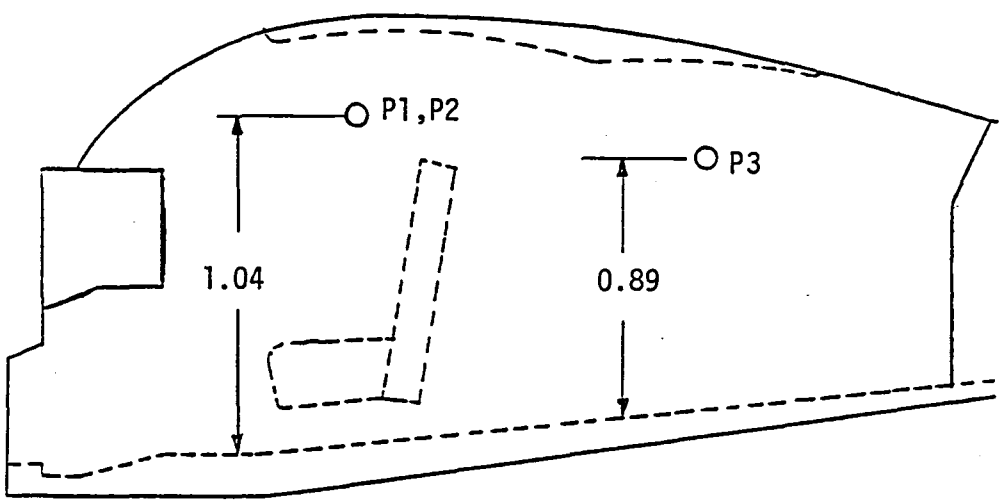

b) Side View

All dimensions in meters.

Figure 2. Cabin Response Microphone Locations.

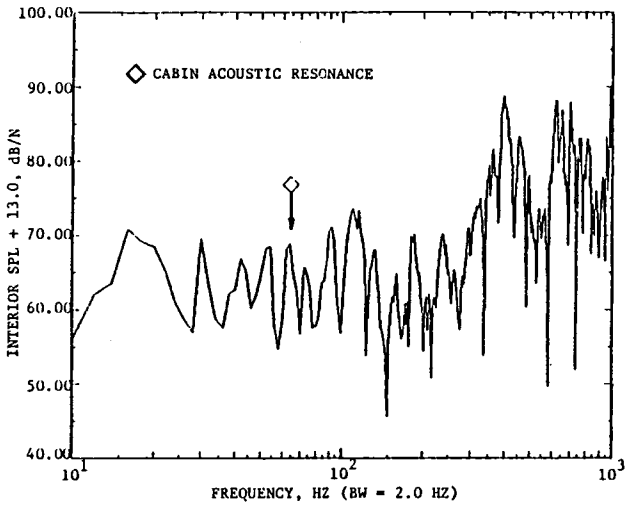

Fuselage sound pressure level transfer function, input at X1, response at P3

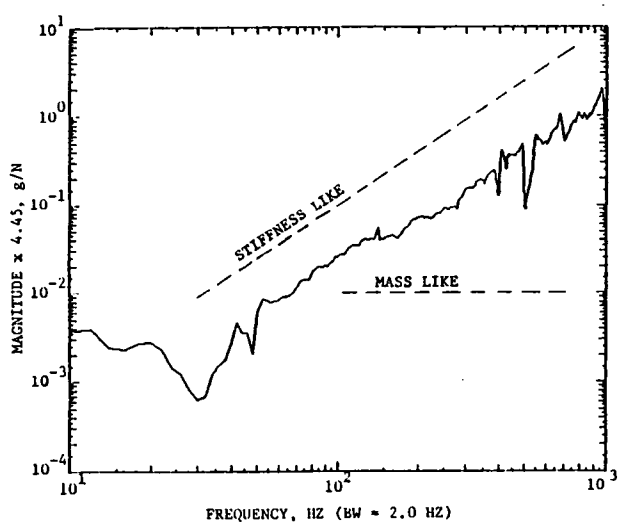

Fuselage driving point inertance at X1

Figure 3. Typical Cabin and Firewall Spectral Responses.

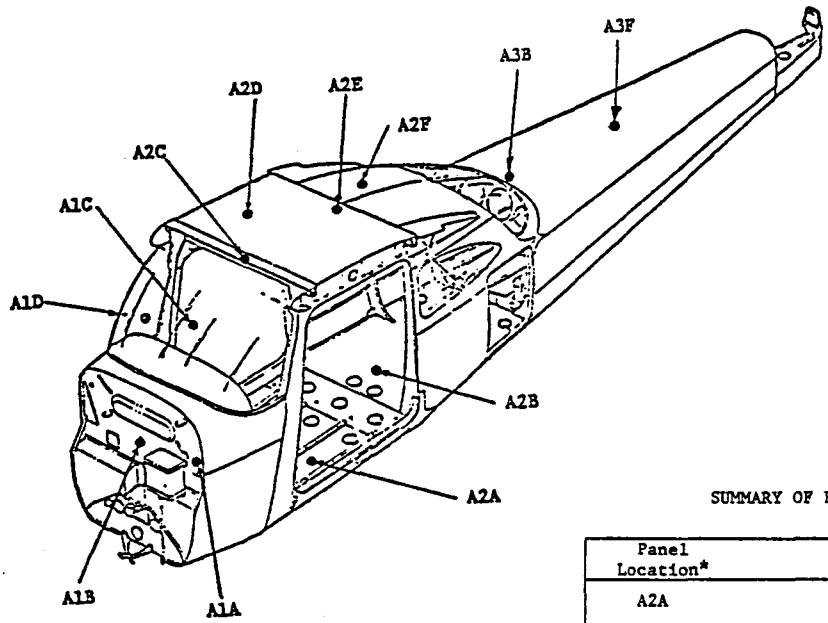

SUMMARY OF FUSELAGE PANEL RESONANT FREQUENCIES

Panel Location*	Resonant Frequencies (Hz)
A2A	103, 163, 215
A1C	103, 156, 200
A3C	44, 47
A2D	121, 180, 220
A3D	44, 47, 61
A1E	45, 92
A1F	30
A2F	73, 98
A3F	93, 130, 200
A1G	60, 75, 125

*Corresponding to accelerometer locations

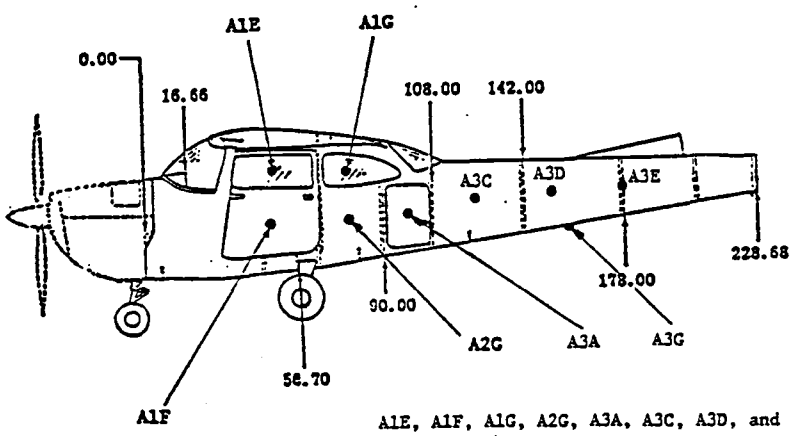

A1E, A1F, A1G, A2G, A3A, A3C, A3D, and A3E on opposite side of aircraft.

Figure 4. Model 172 Test Aircraft Panel Resonant Frequencies.

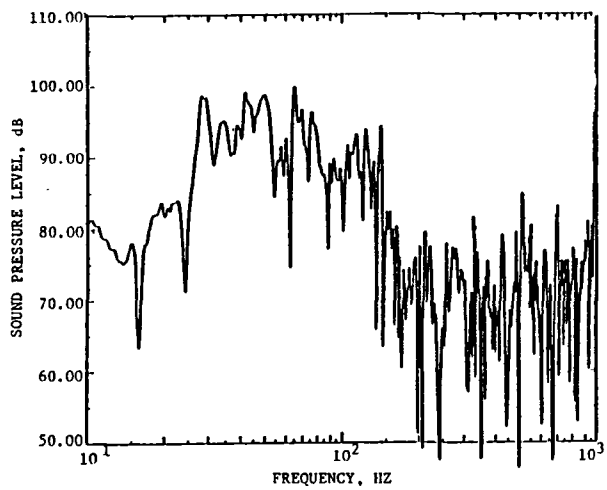

a) Rigid Isolators

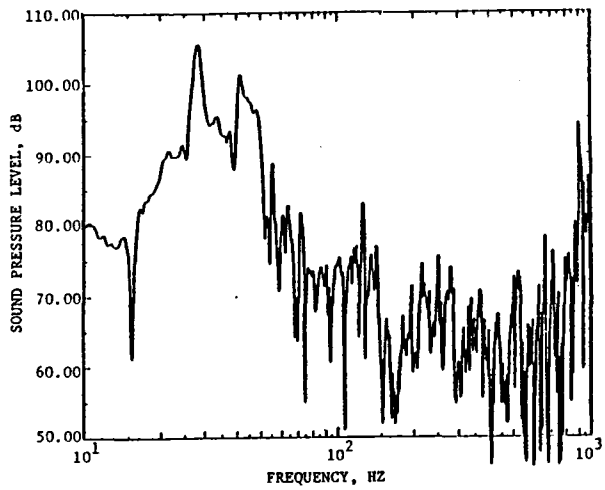

b) Original Equipment (3006H)

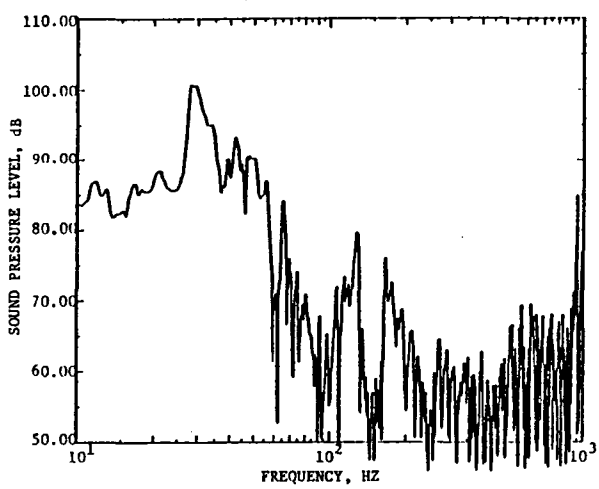

c) Soft Rubber (22002-1)

Figure 5a. Measured SPL Transfer Function Spectra at P1, Load Case #2, Ref. 89N rms.

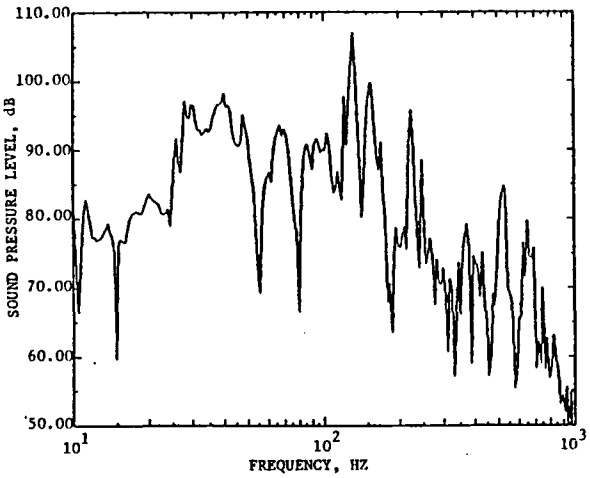

a) Rigid Isolators

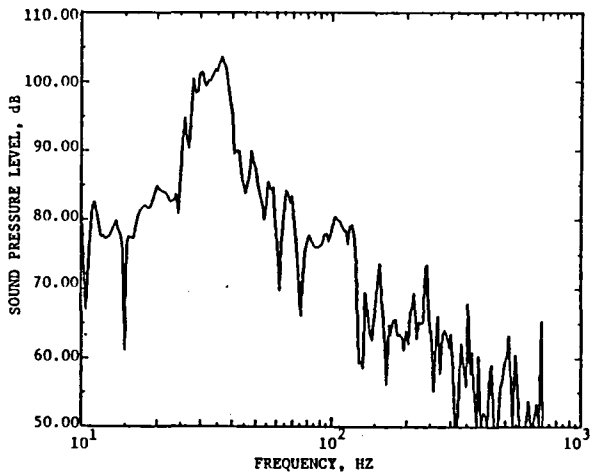

b) Original Equipment (3006H)

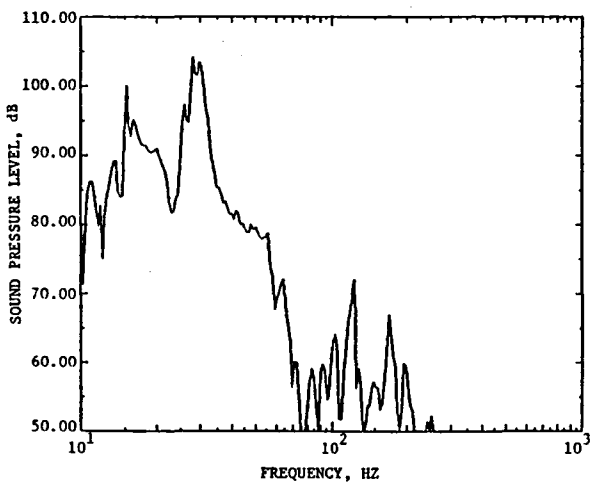

c) Soft Rubber (22002-1)

Figure 5b. Computed SPL Transfer Function Spectra at P1, Load Case #2, Static Isolator Properties, Ref. 89N rms.

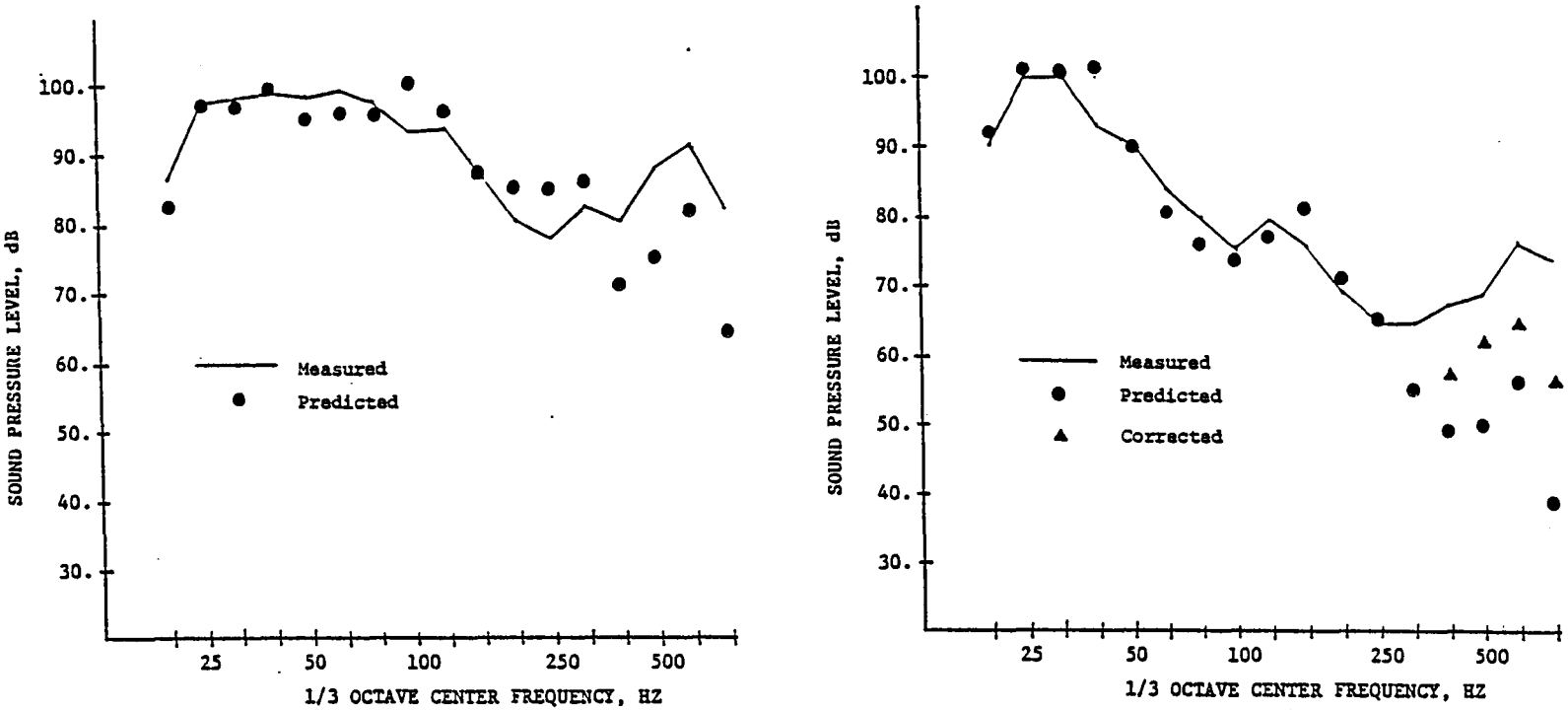

a) Rigid Isolators

b) Soft Rubber (22002-1)

Figure 6. Comparison of Measured and Predicted Maximum Interior SPL Responses for Measured Isolator Properties.

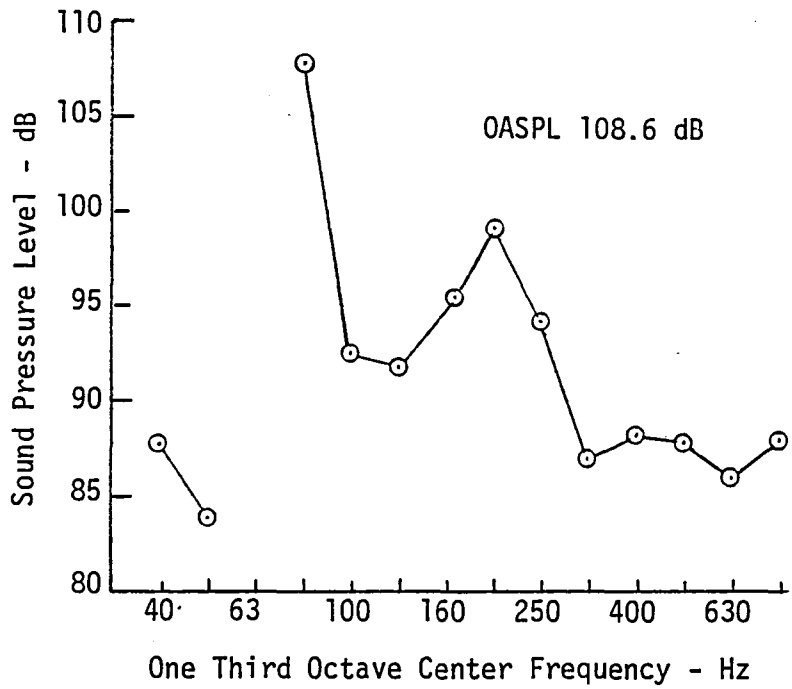

a) Unweighted

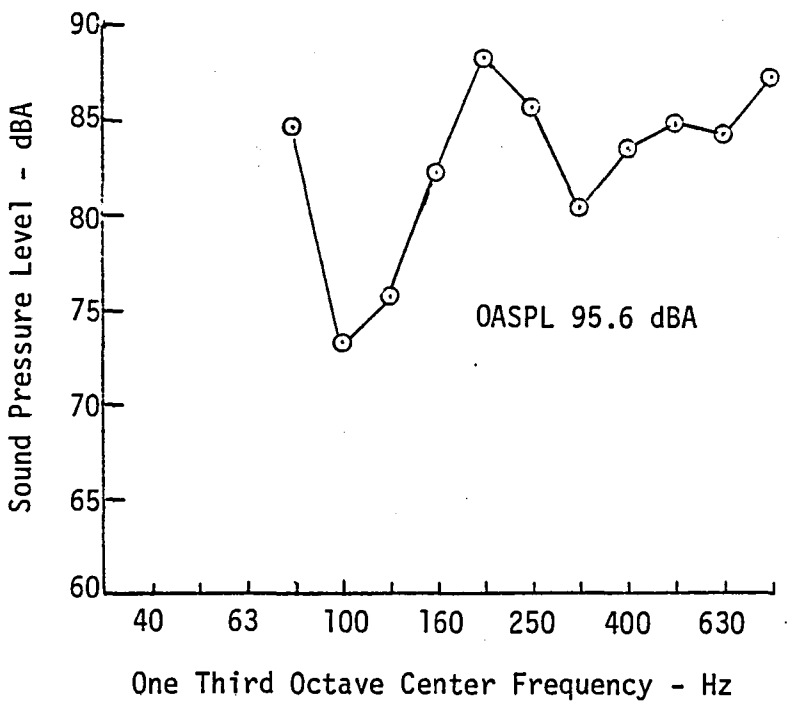

b) A-Weighted

Figure 7. Measured Structure-Borne Noise Levels During Engine Excitation, 3006H Isolator, 2160 rpm, Interior Removed.

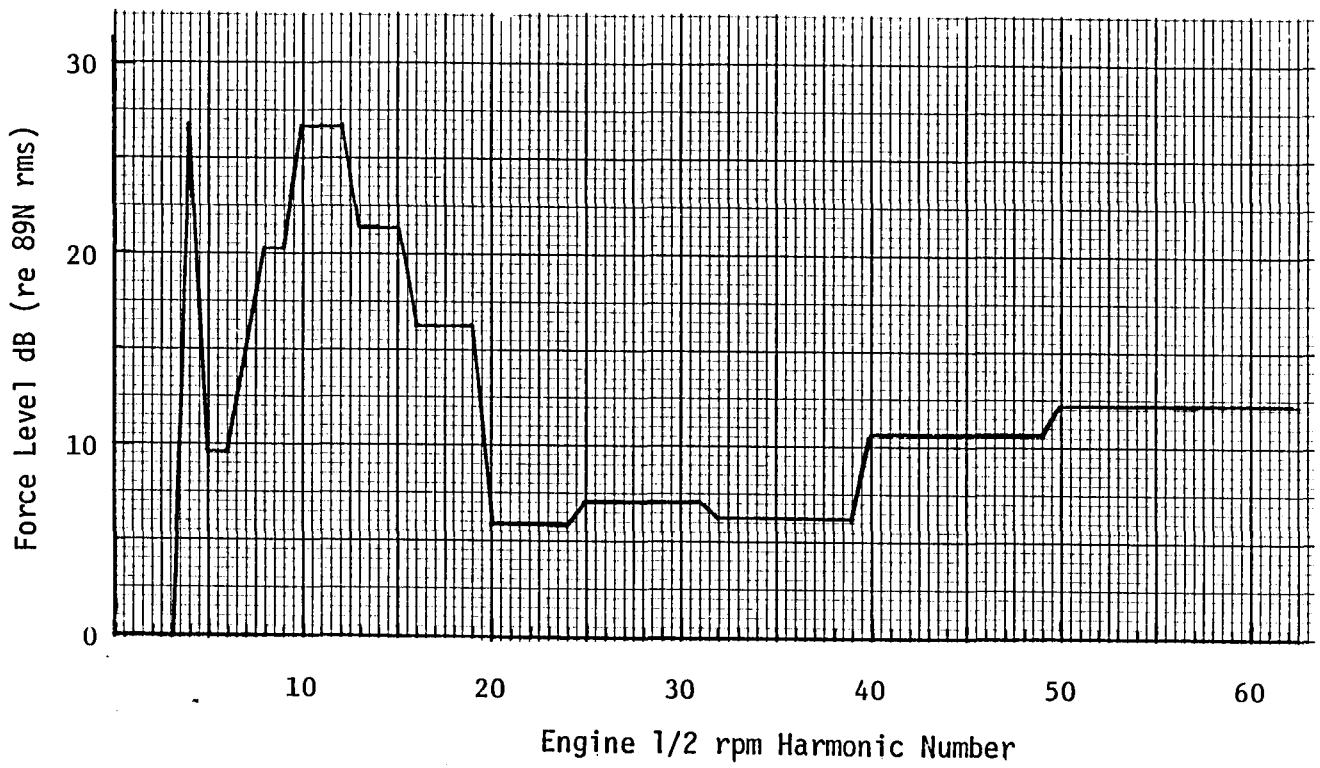

Figure 8. Simulated Engine Running 1/2 rpm Harmonic Force Levels.

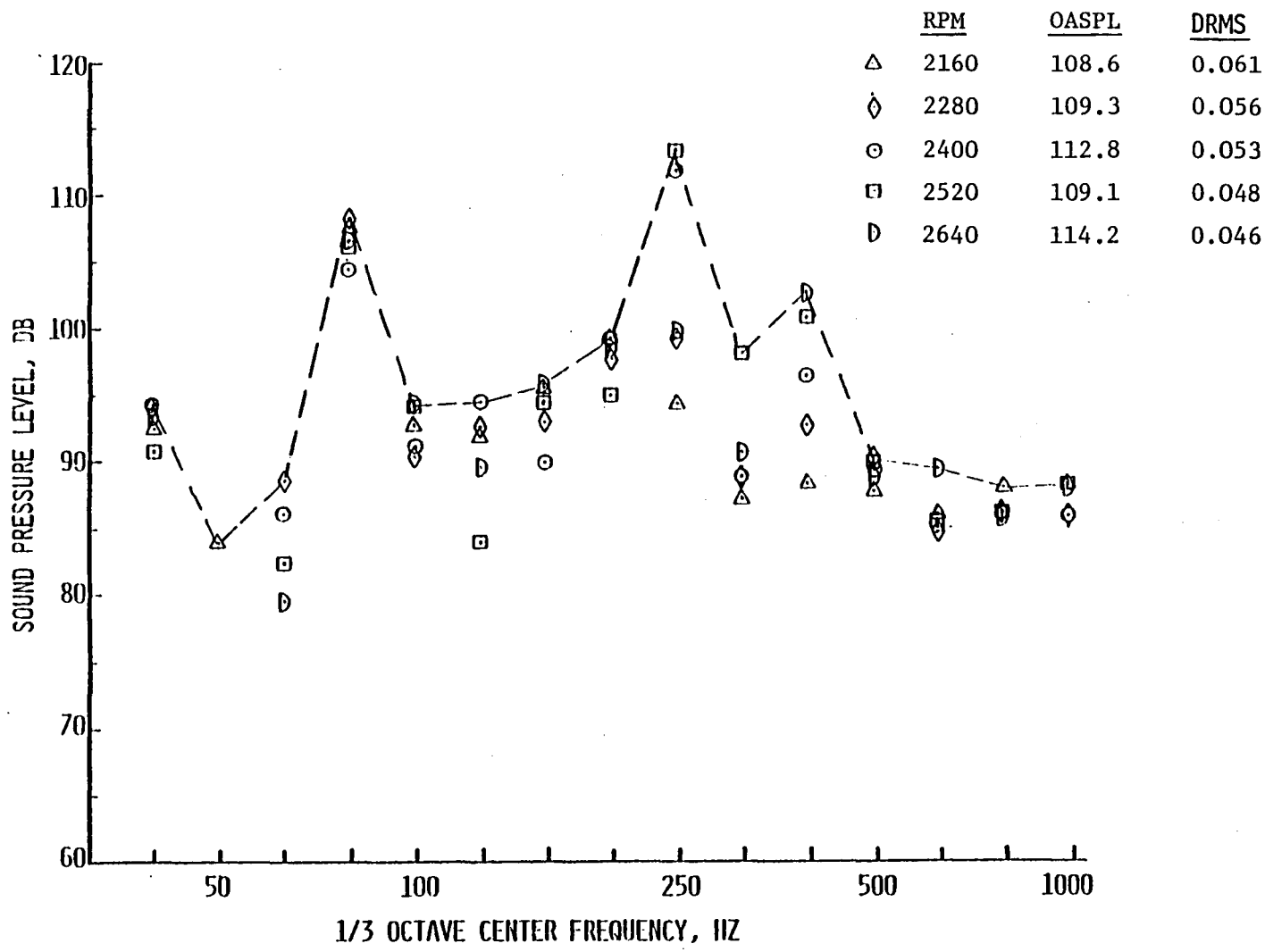

Figure 9. Predicted Interior SPL, Original Equipment Isolators.

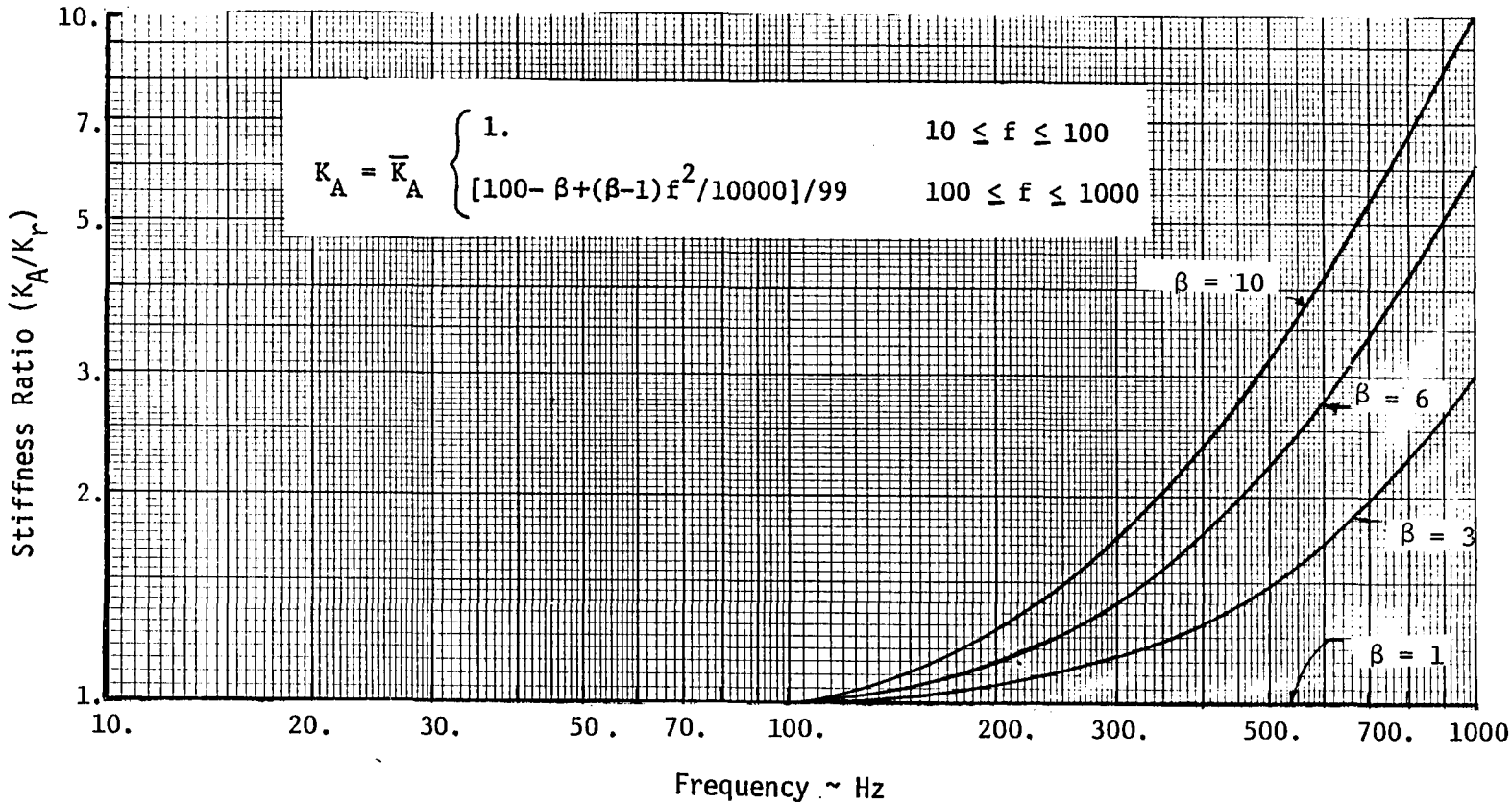

Figure 10. Isolator Frequency Dependence Model, Ref. K_r = 1751 N/cm (1000. lb/in.).

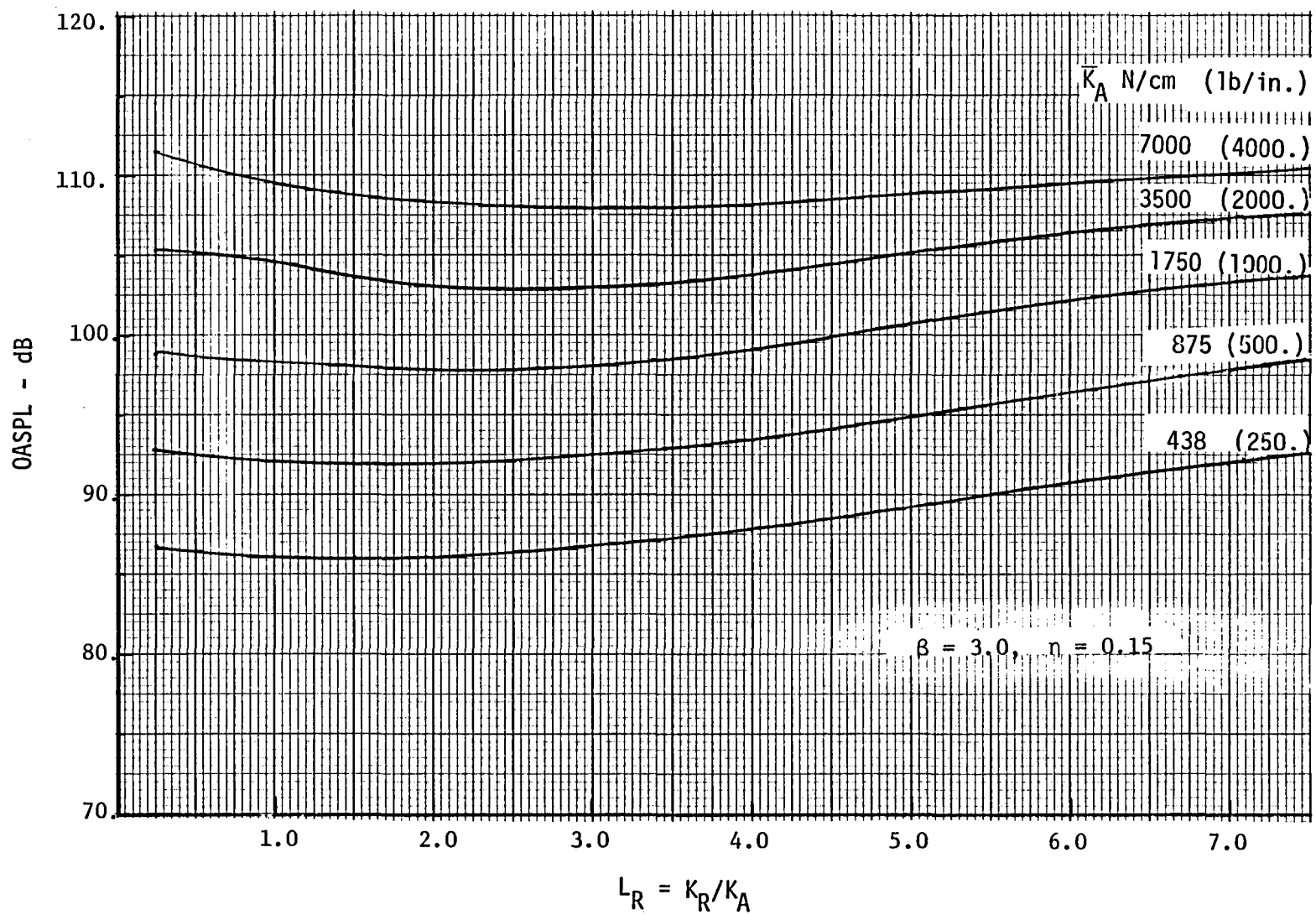

Figure 11. Effect of Radial to Axial Stiffness Ratio on OASPL

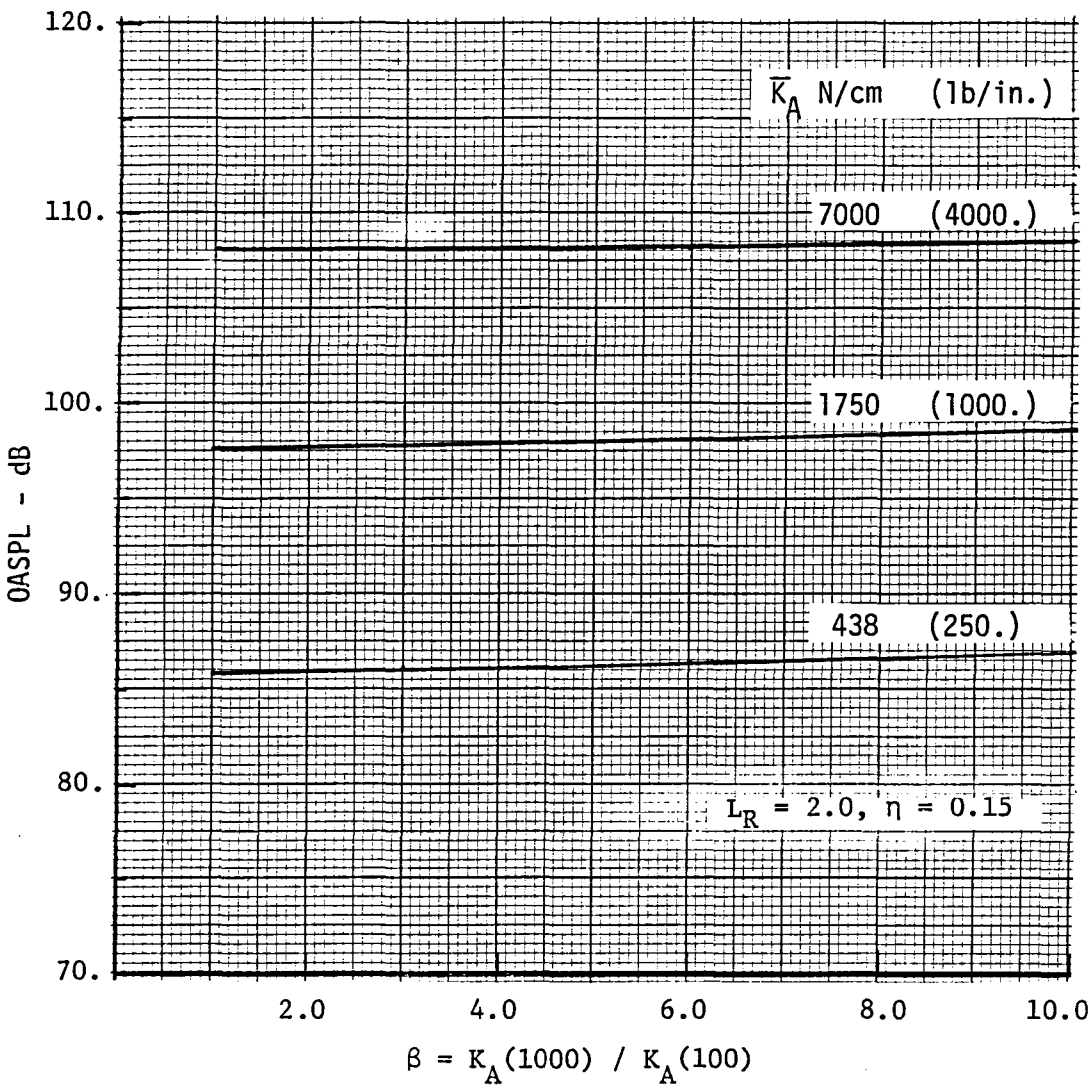

Figure 12. Effect of Isolator Frequency Dependence on OASPL

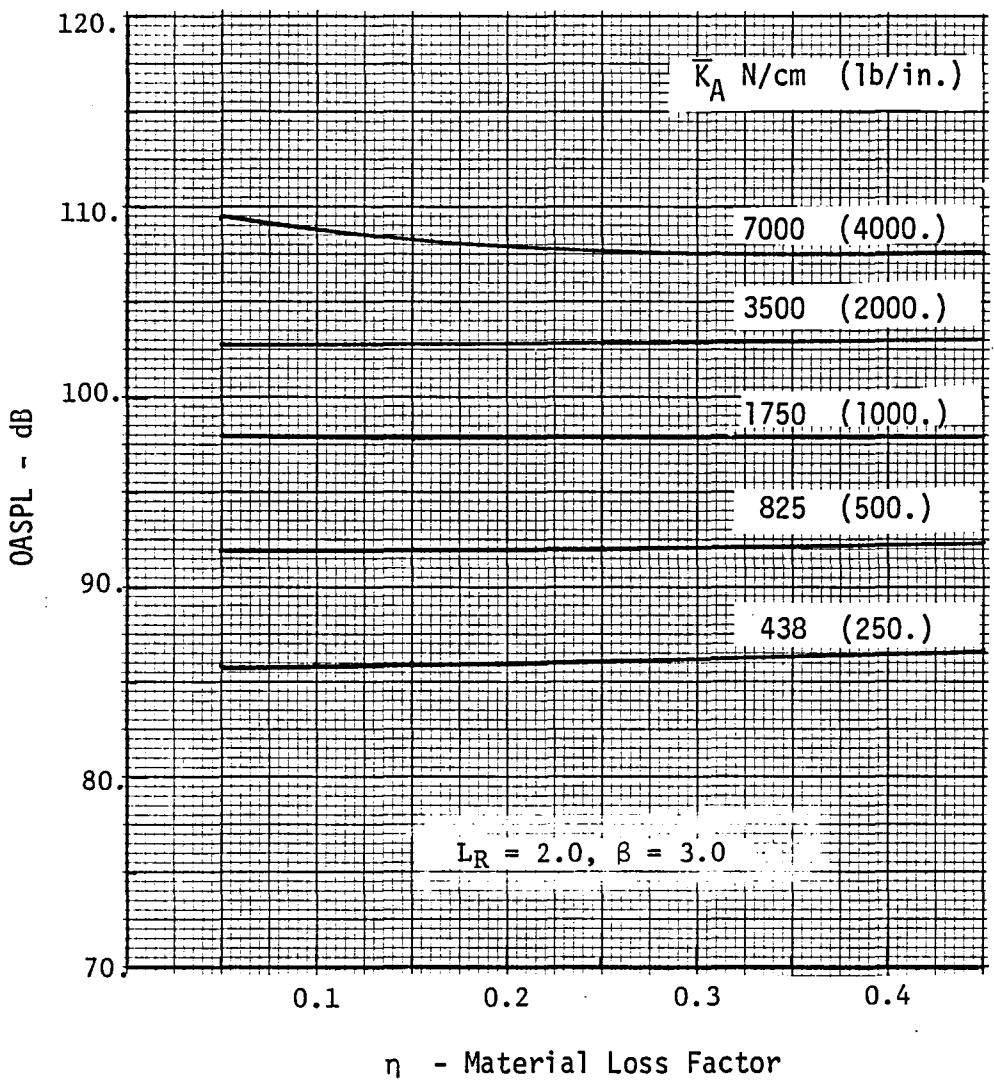

Figure 13. Effect of Material Loss Factor on OASPL.

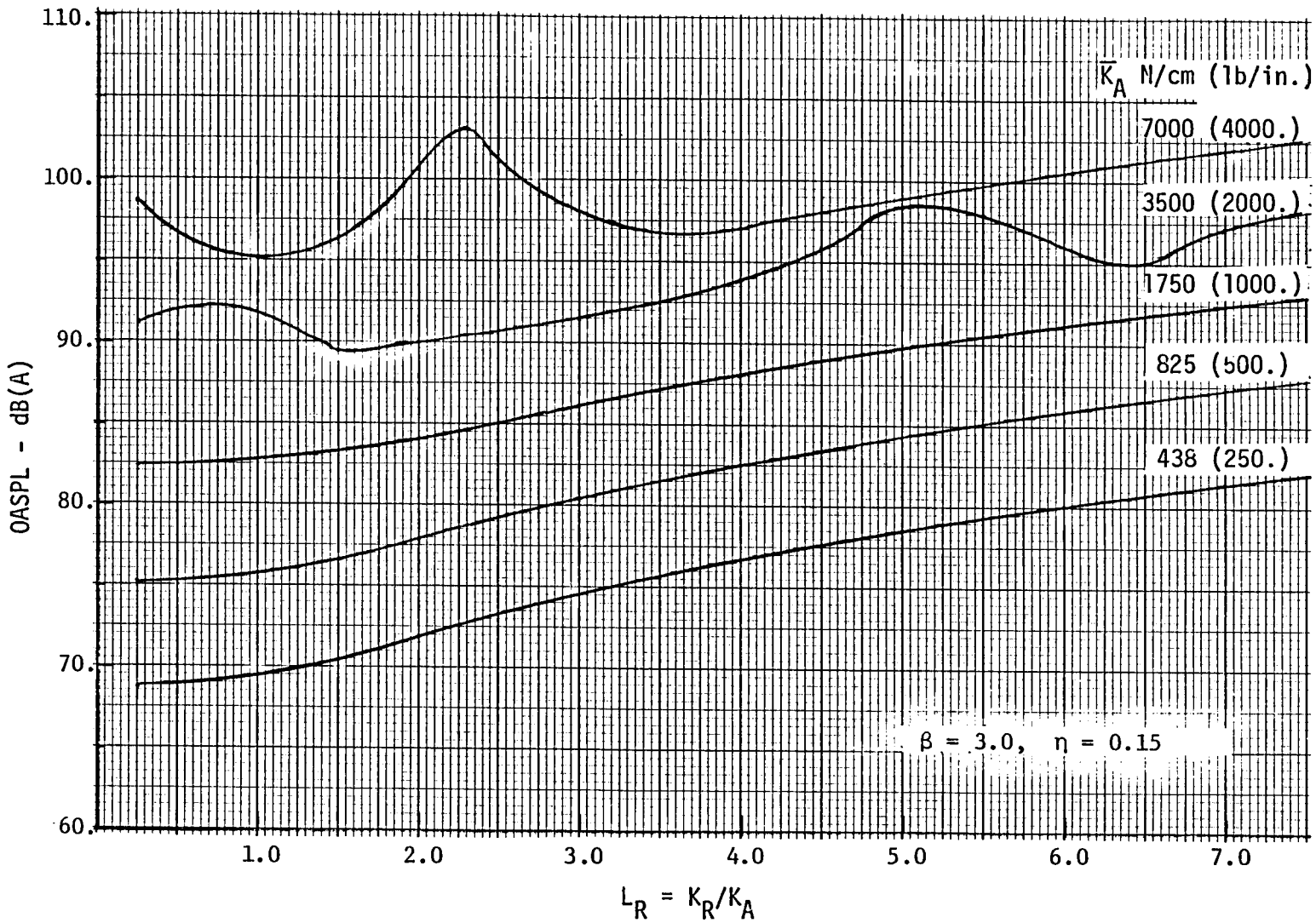

Figure 14. Effect of Radial to Axial Stiffness Ratio on OASPL - A wt.

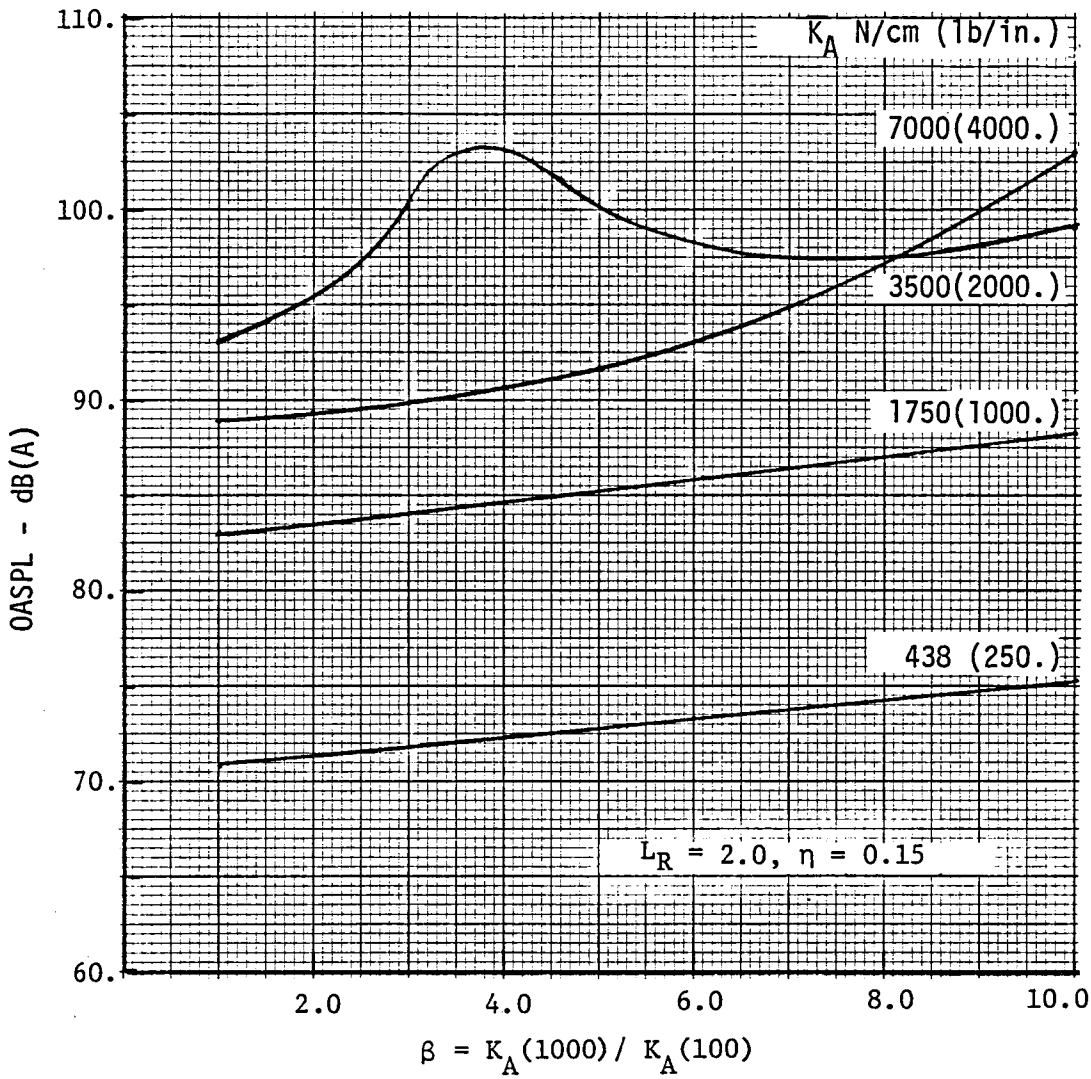

Figure 15. Effect of Isolator Frequency Dependence on OASPL - A wt.

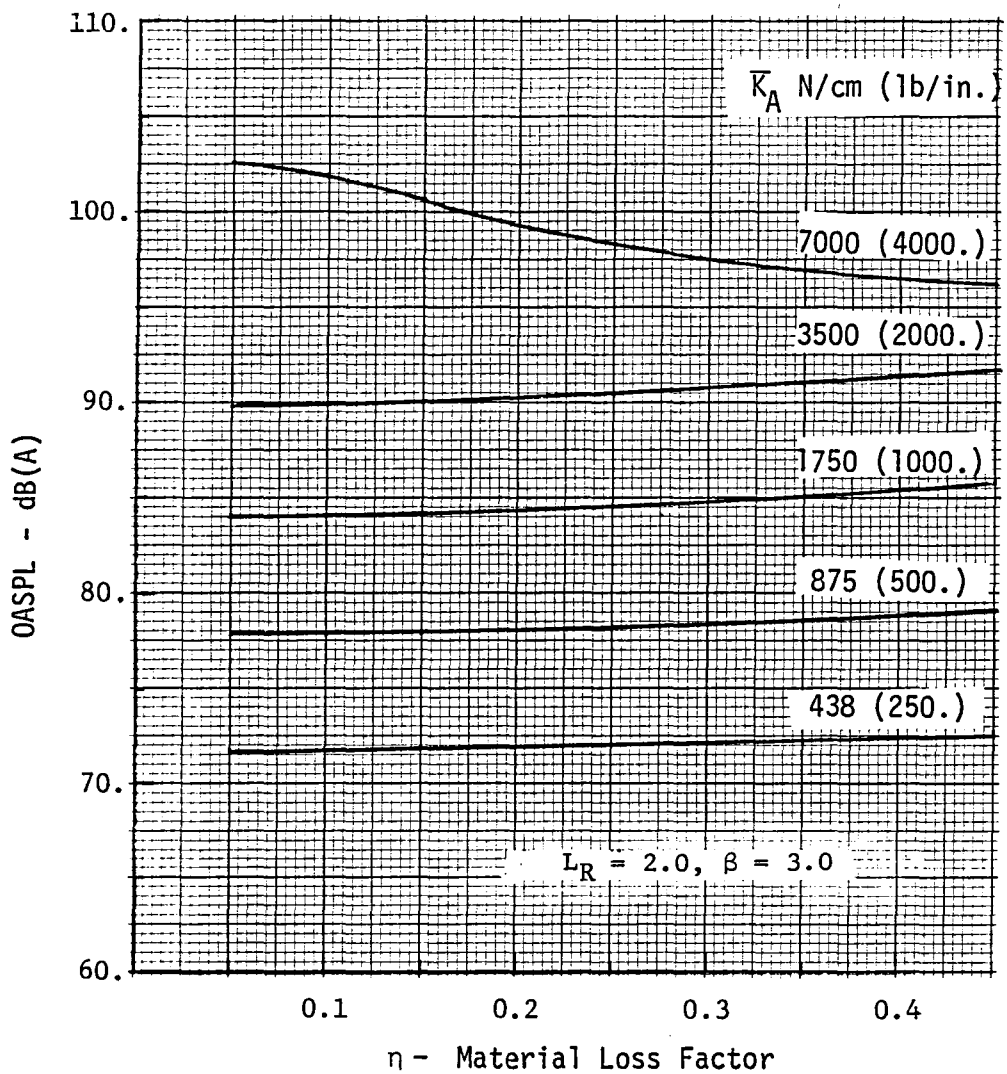

Figure 16. Effect of Material Loss Factor on OASPL - A wt.

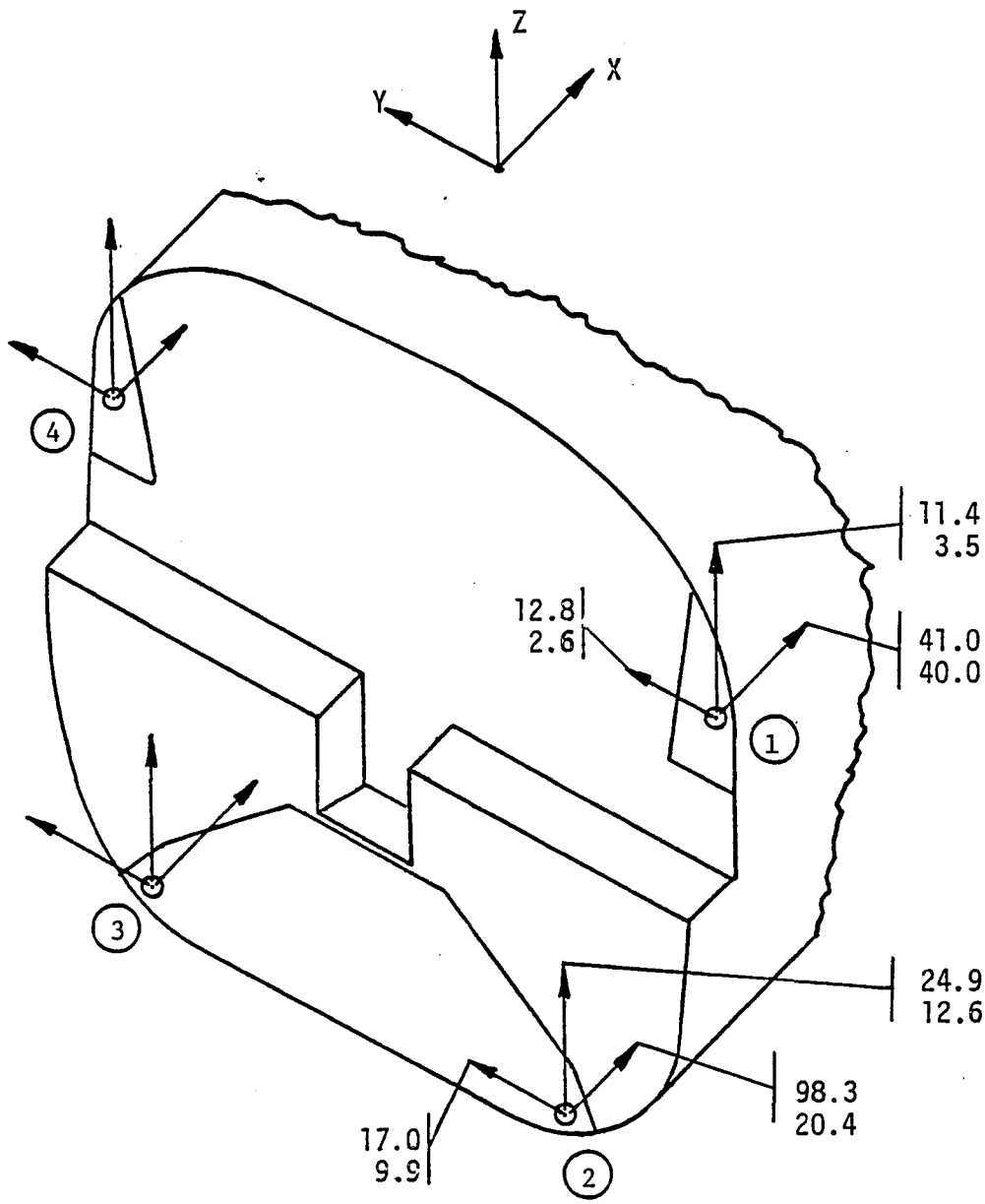

SYMMETRIC STRUCTURE

Figure 17. Fuselage Engine Mount Attach Point Stiffness Ratio K/K_r, K_r = 1750 N/cm (1000 lb/in.).

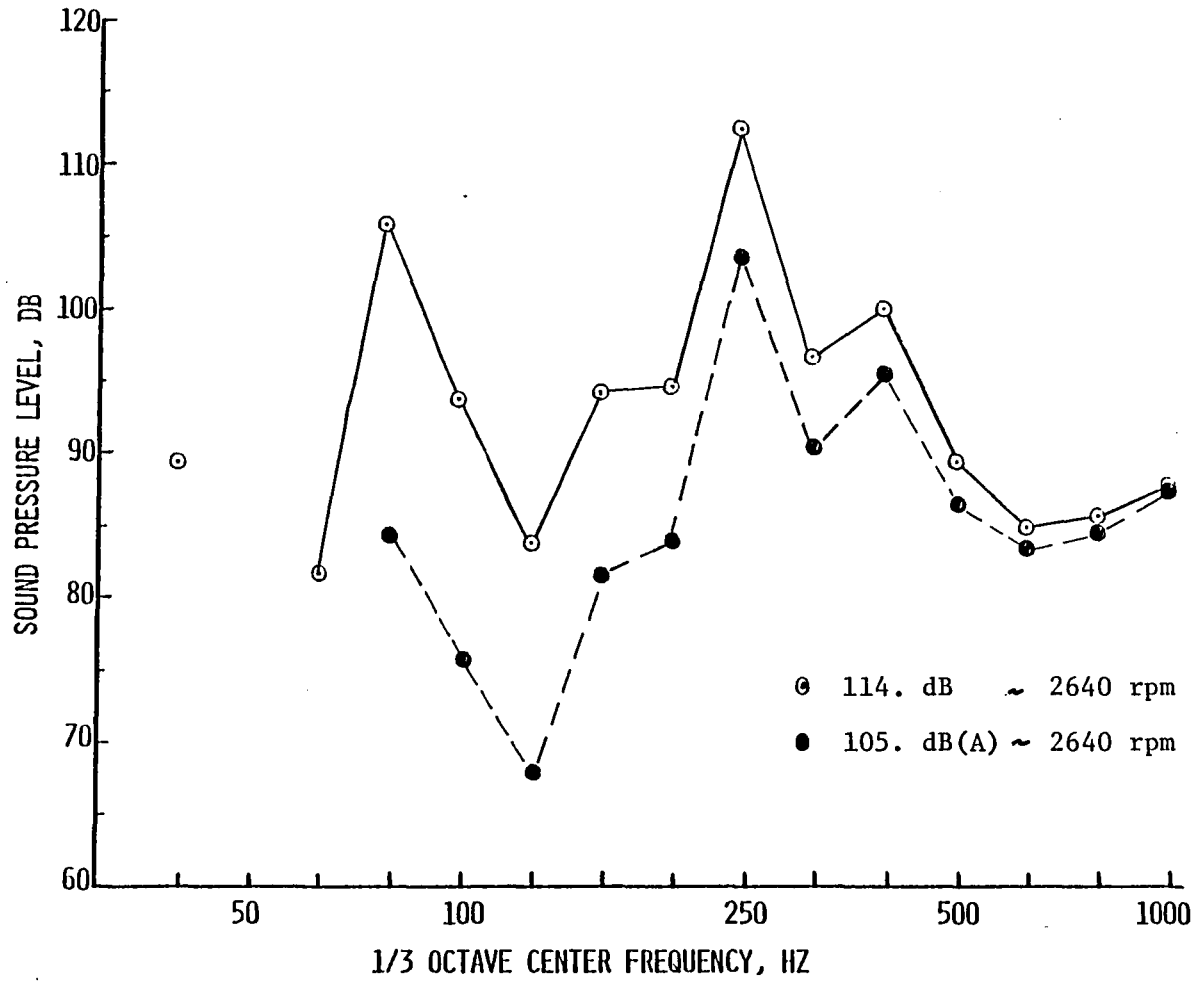

Figure 18. Predicted Maximum Interior SPL Spectra ~ Original Equipment Isolators.

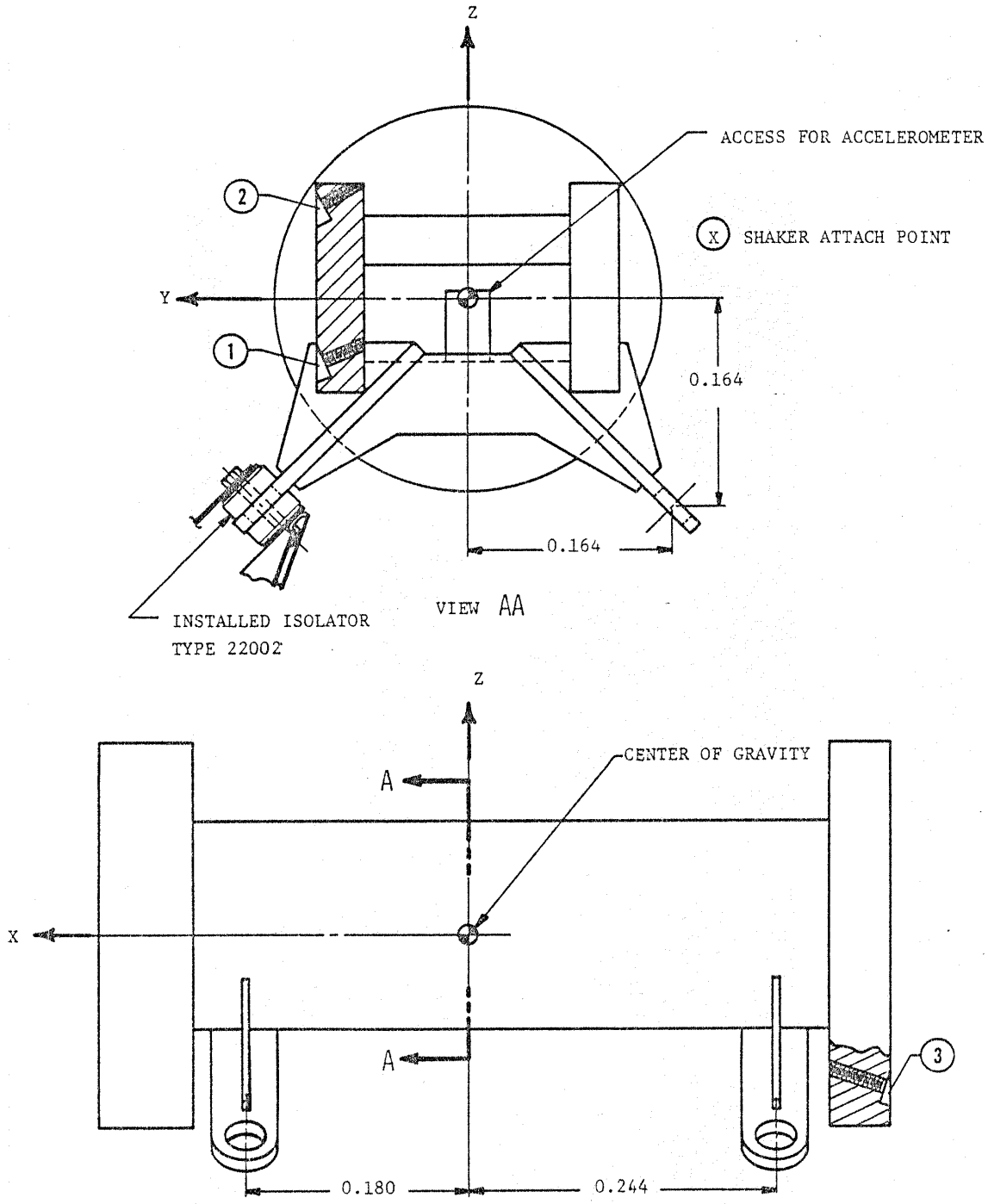

* All Dimensions Given In Meters

Figure 19. Sketch of the Rigid Engine.

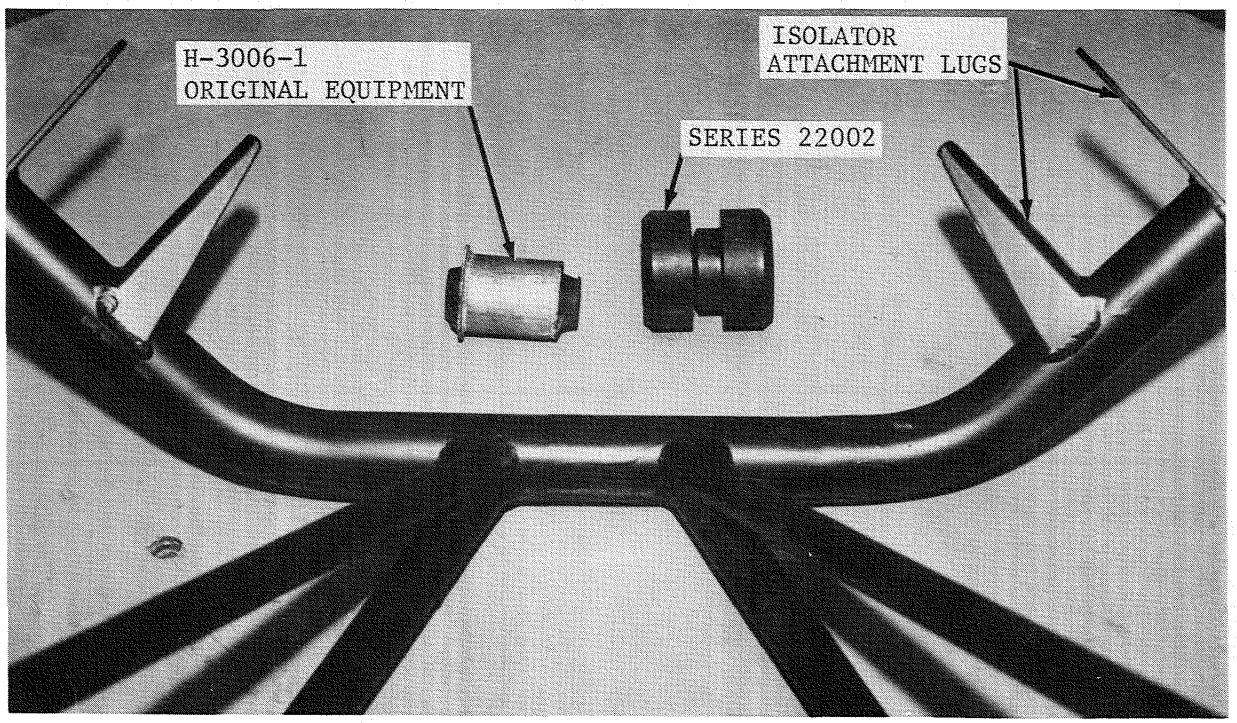

Figure 20. Vibration Isolators and Mounting Lugs

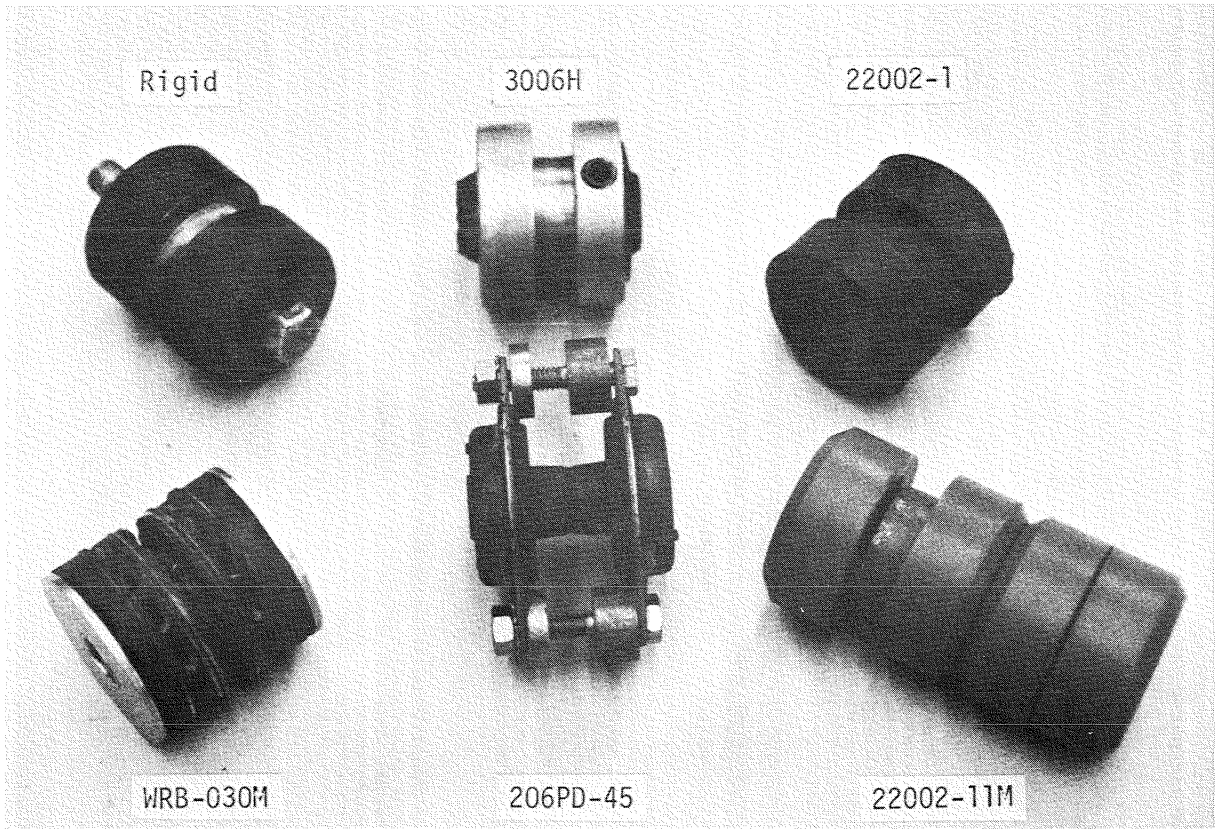

Figure 21. Isolator Configurations.

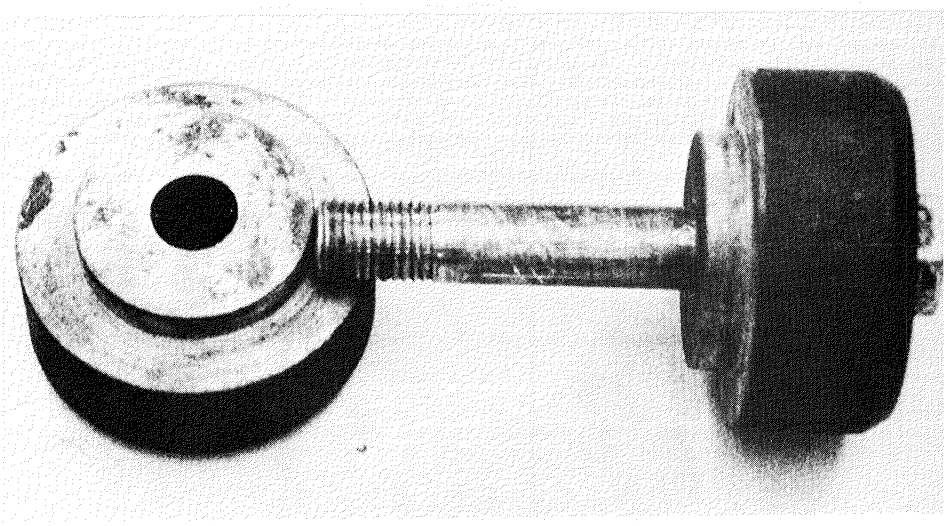

a) Rigid

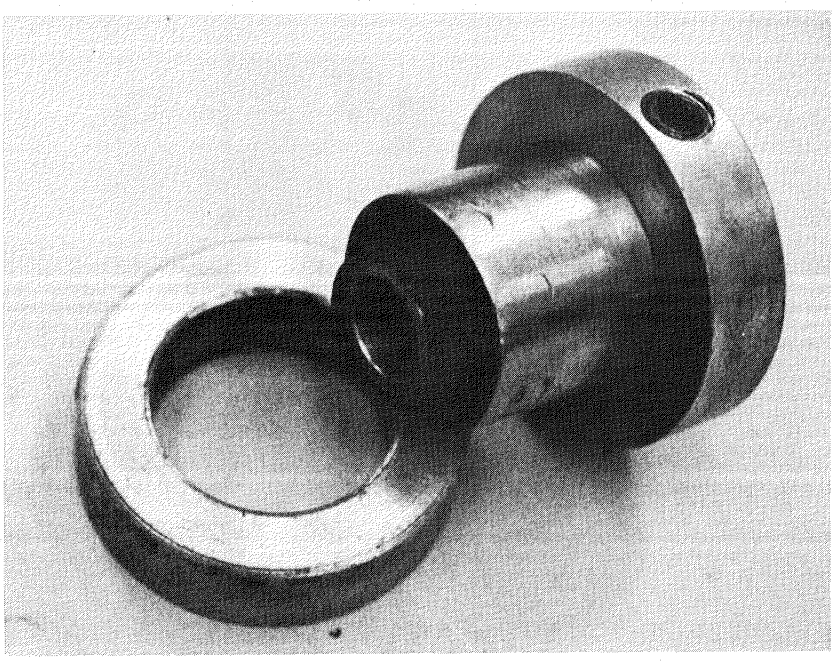

b) 3006H

Figure 22. Isolator Component Parts.

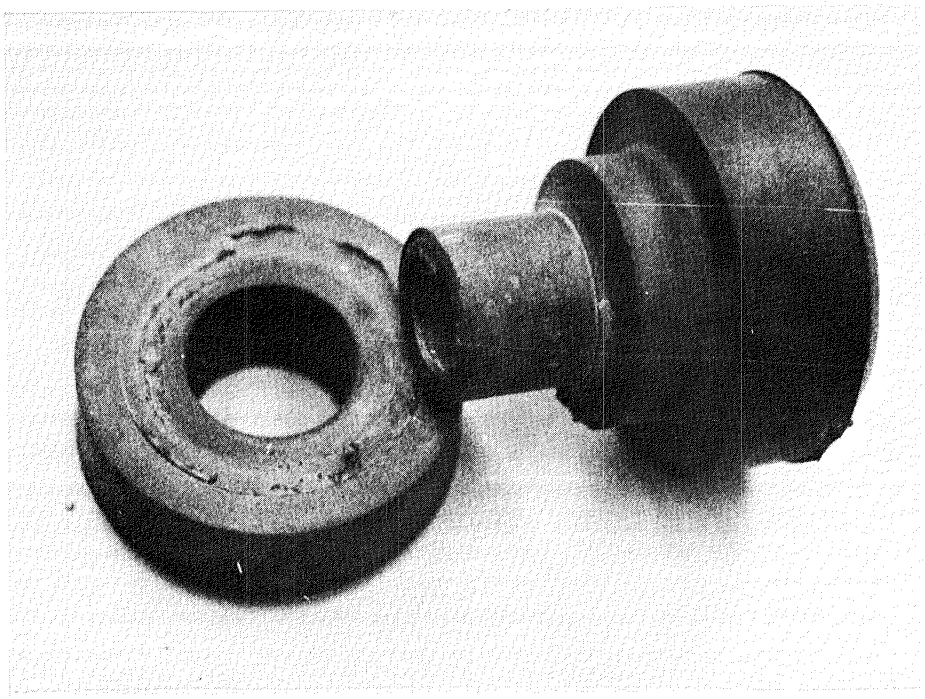

c) 22002-1

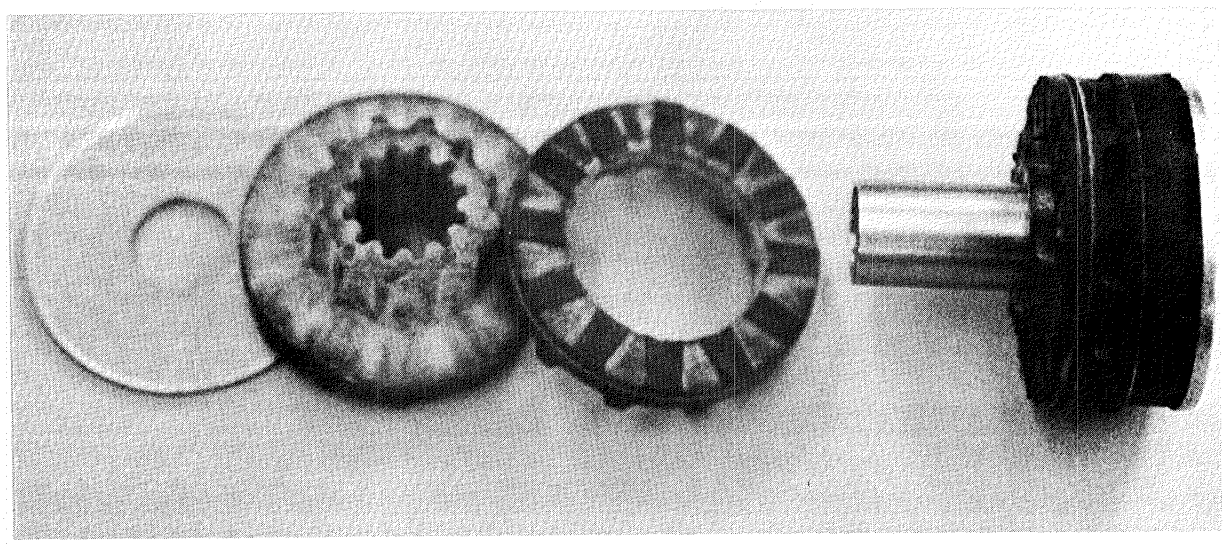

d) WRB-030M

Figure 22. (Continued) - Isolator Component Parts.

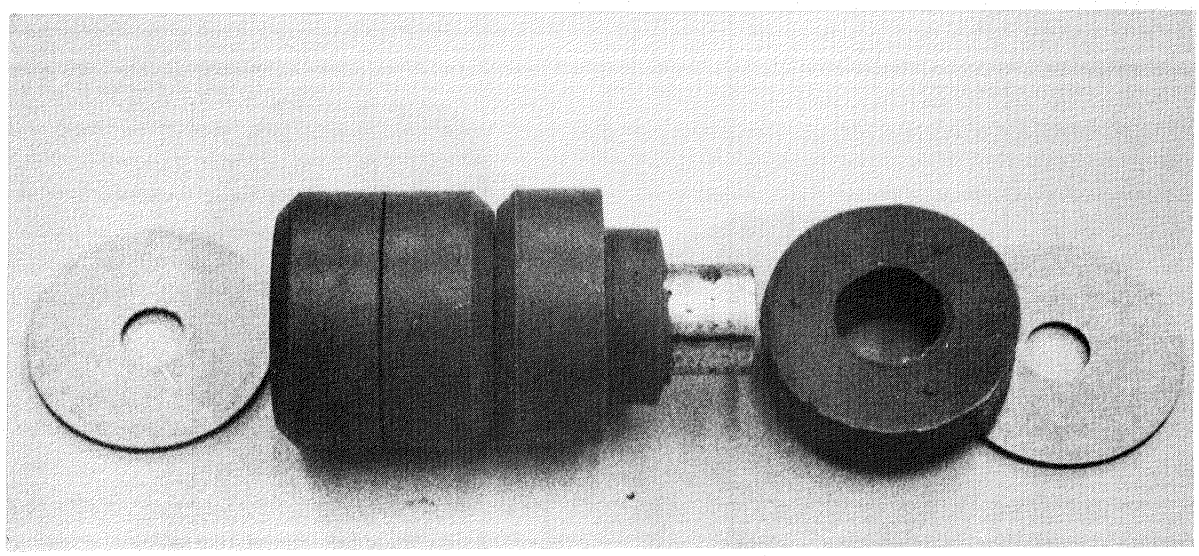

e) 22002-11M

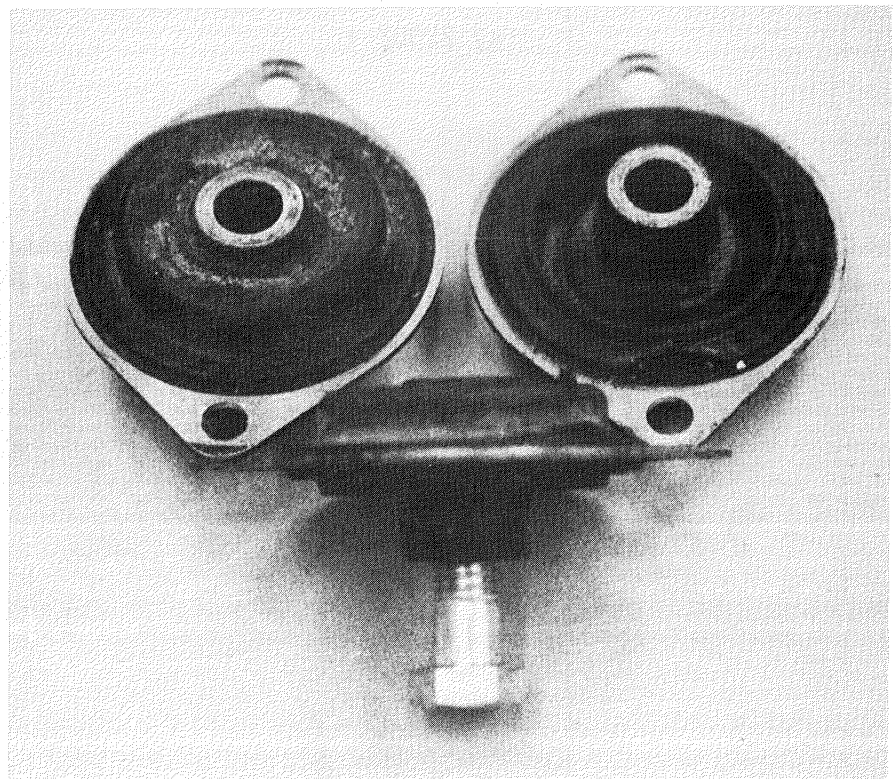

f) 206PD-45

Figure 22. (Continued) - Isolator Component Parts.

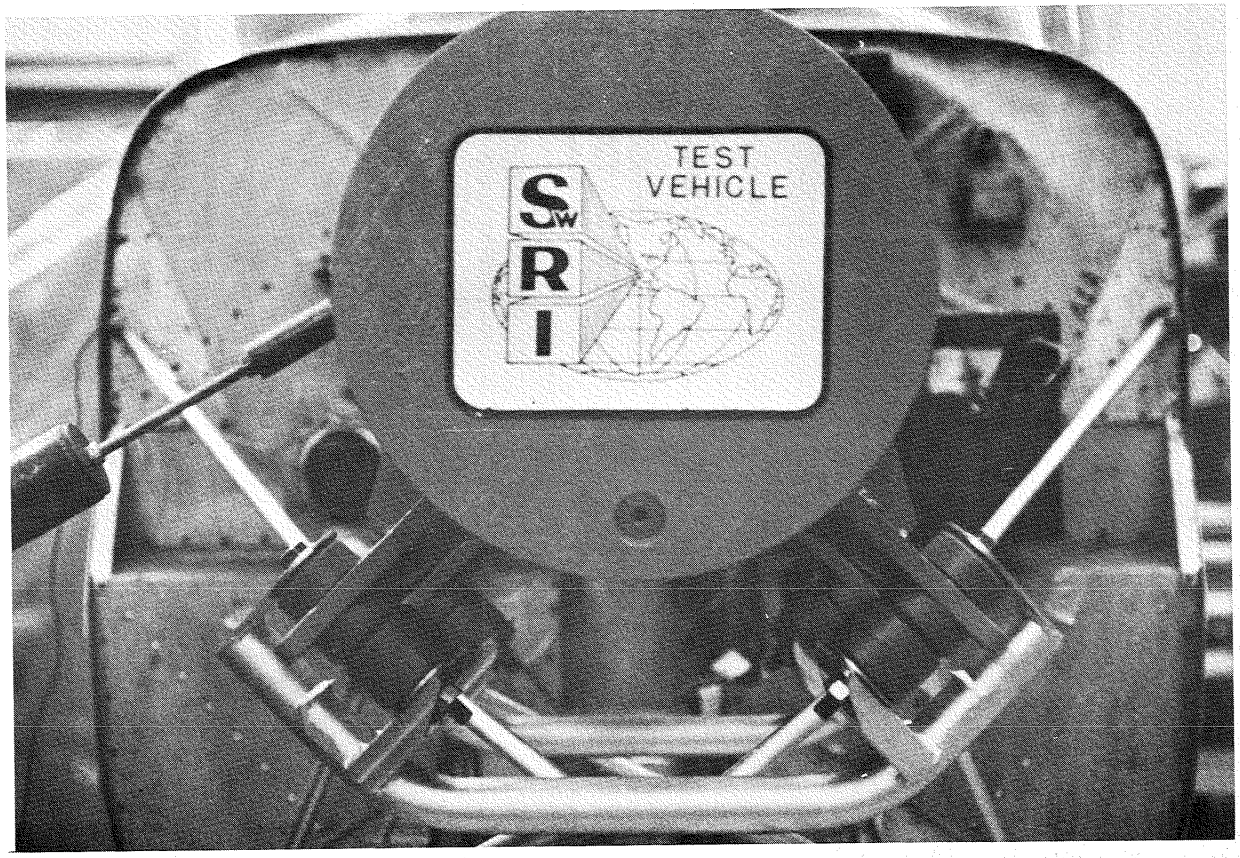

Figure 23. Installed 22002-11M Isolator Configuration.

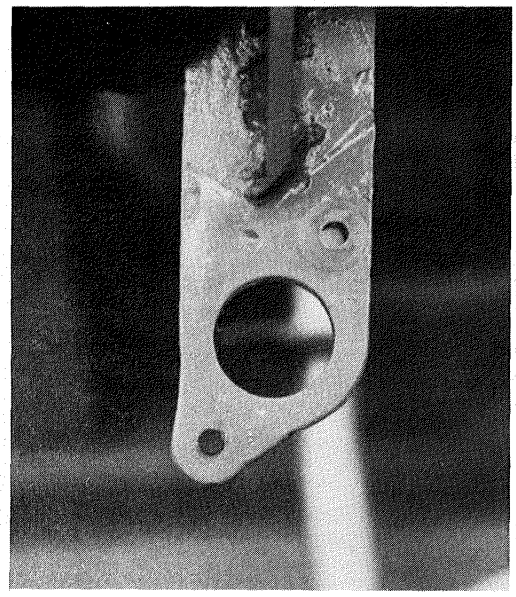

a) Modified Engine Arm

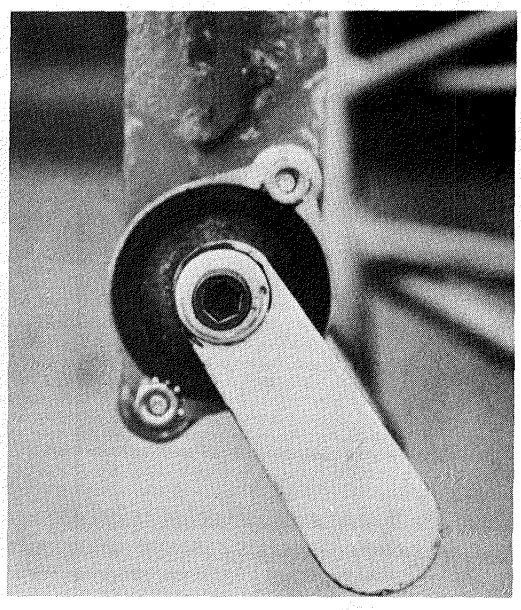

b) Side View (Installed)

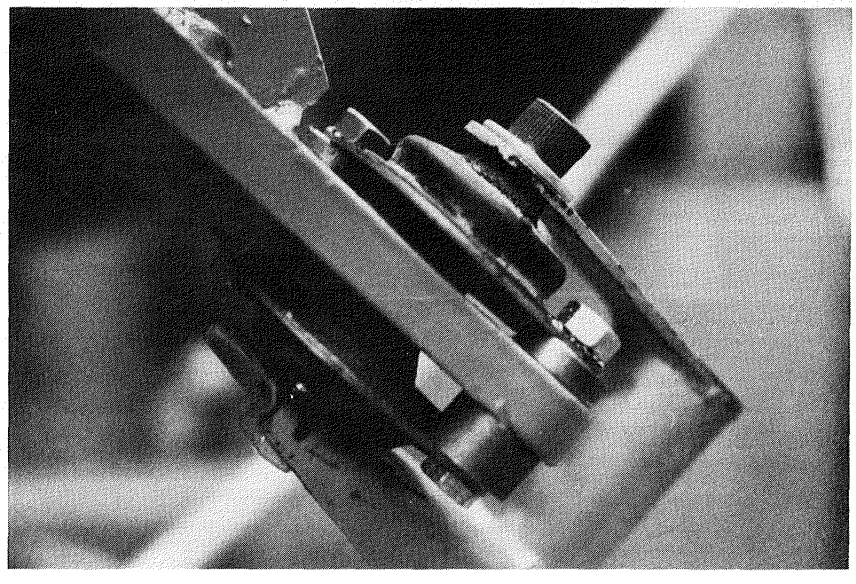

c) Front View (Installed)

Figure 24. Installed 206PD-45 Isolator Configuration.

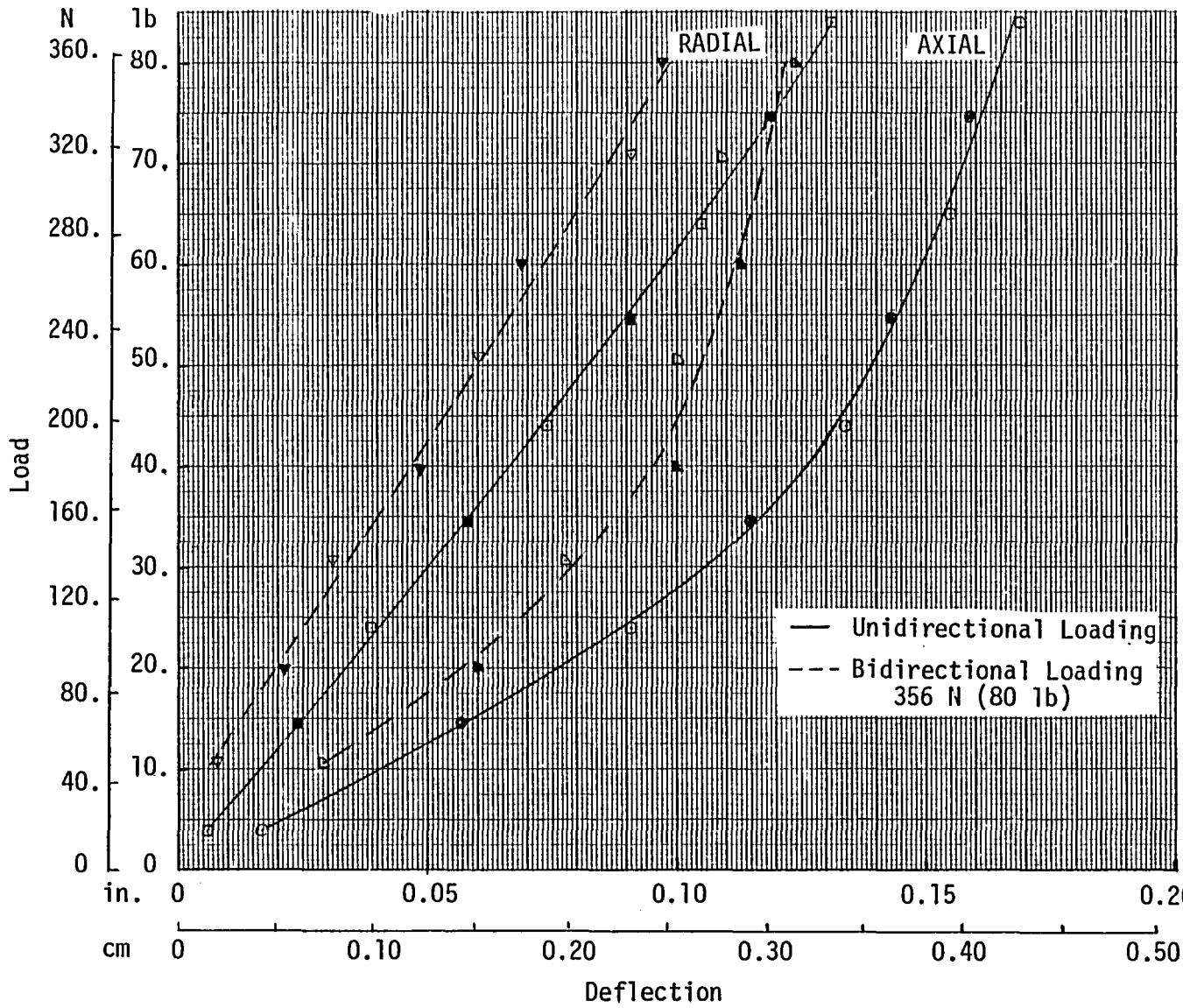

Figure 25. Static Load Deflection Curves, WRB-030M Isolator.

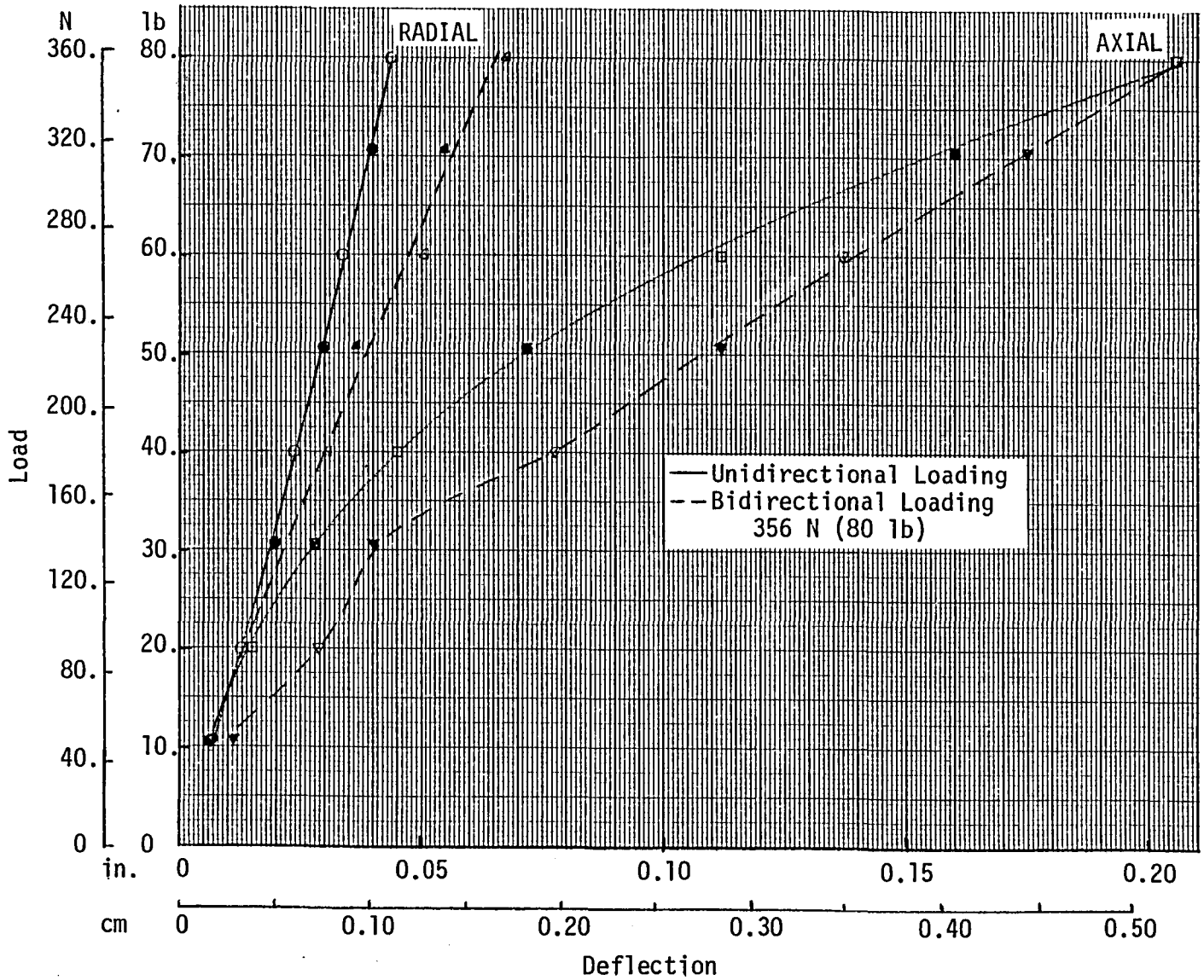

Figure 26. Static Load Deflection Curves, 22002-11M Isolator.

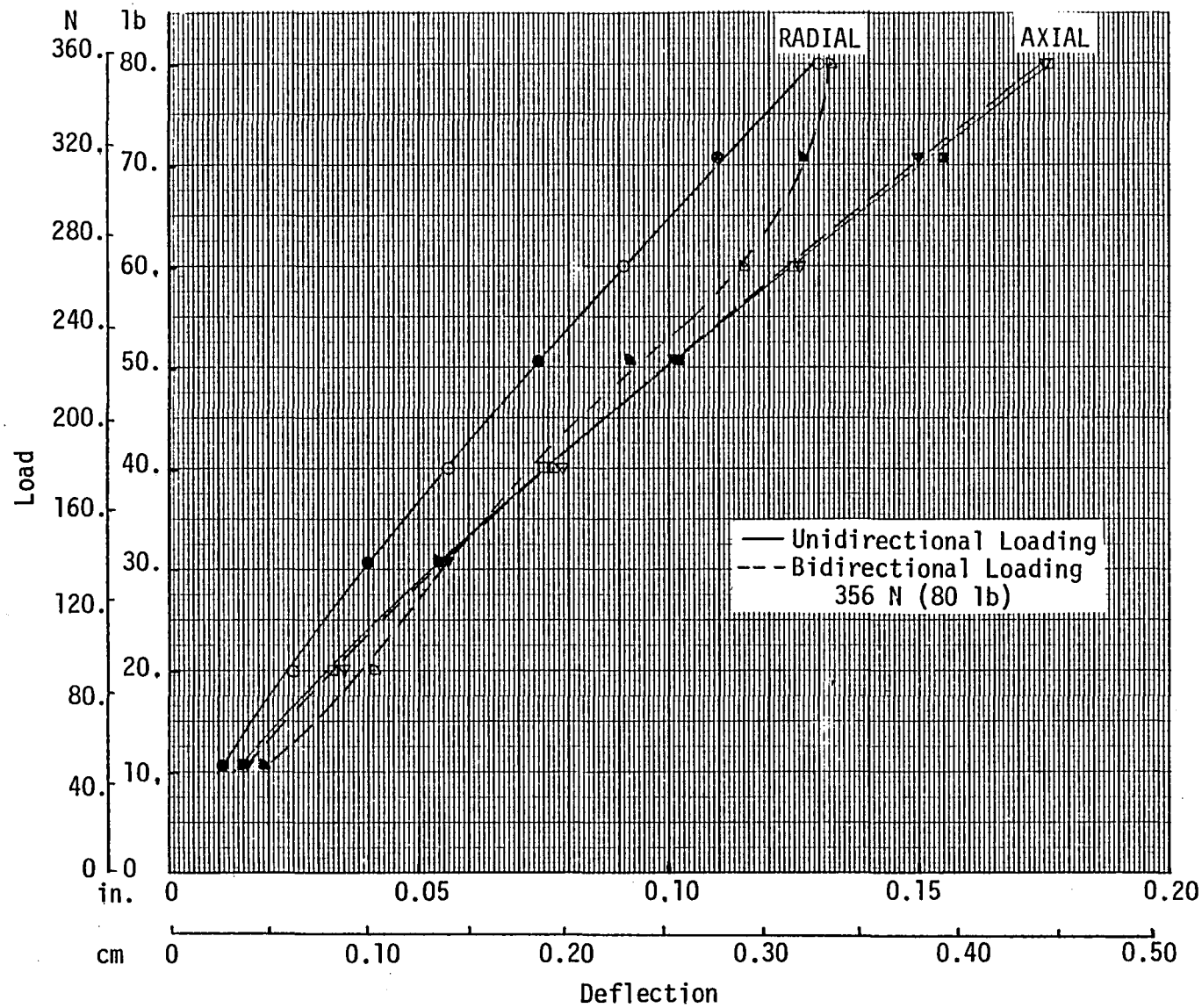

Figure 27. Static Load Deflection Curve, 206PD-45 Isolator.

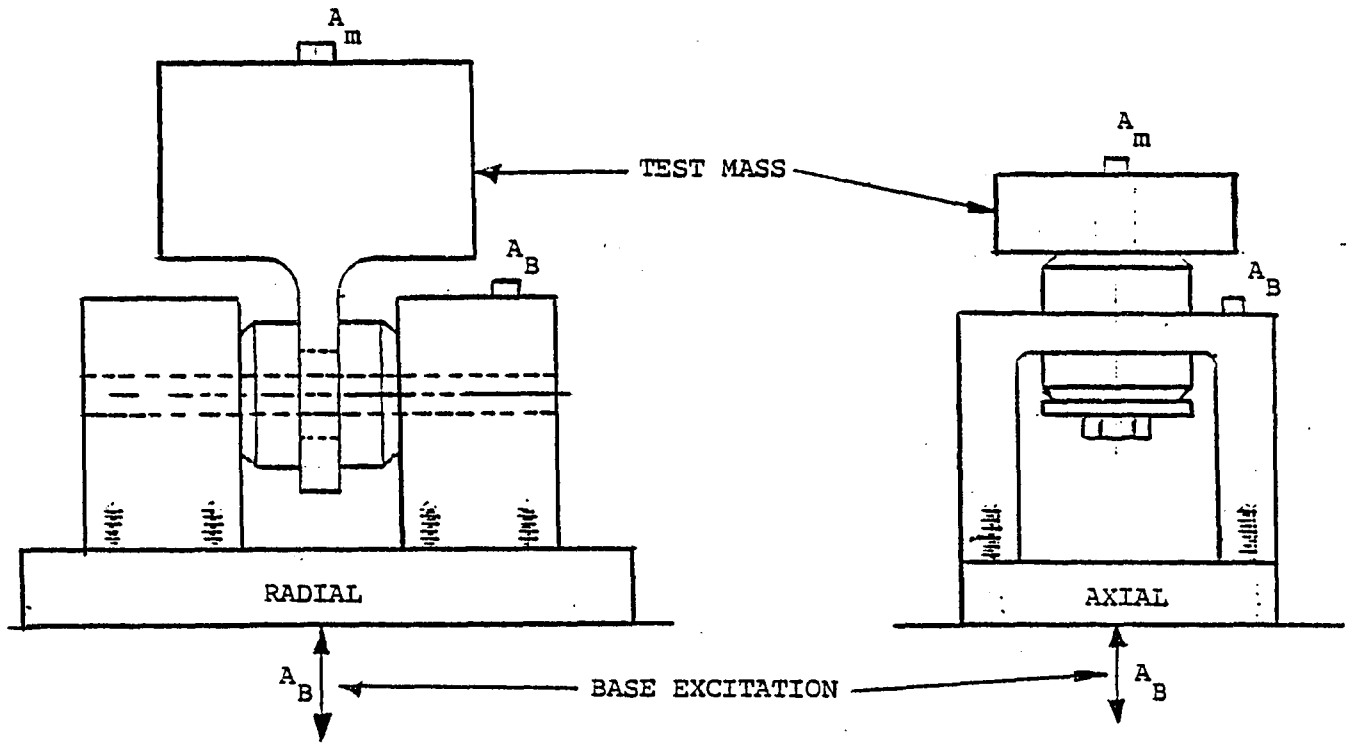

Figure 28. Isolator Dynamic Properties Test Setup.

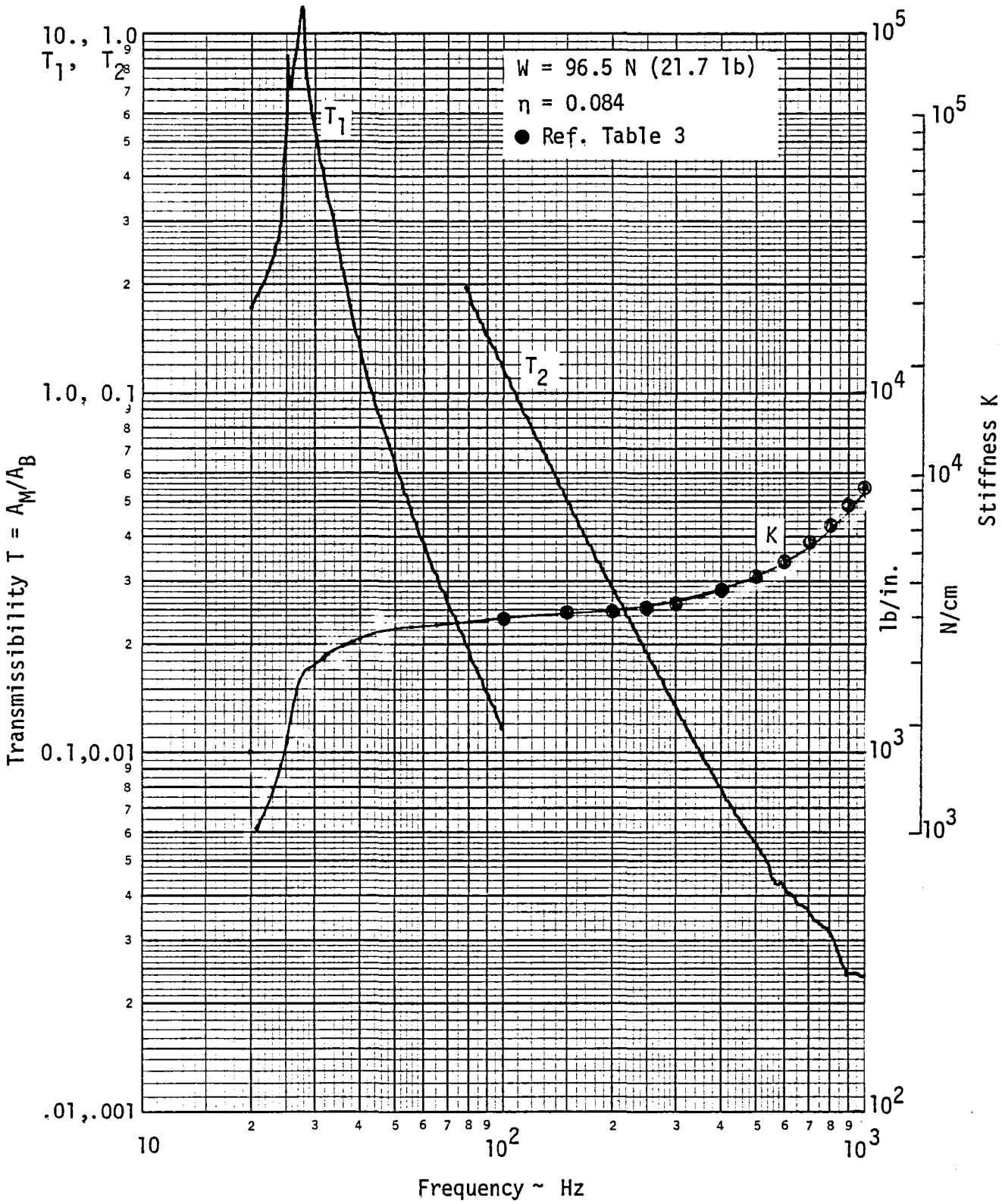

Figure 29a. Measured Transmissibility and Computed Axial Stiffness 22002-1 Isolator.

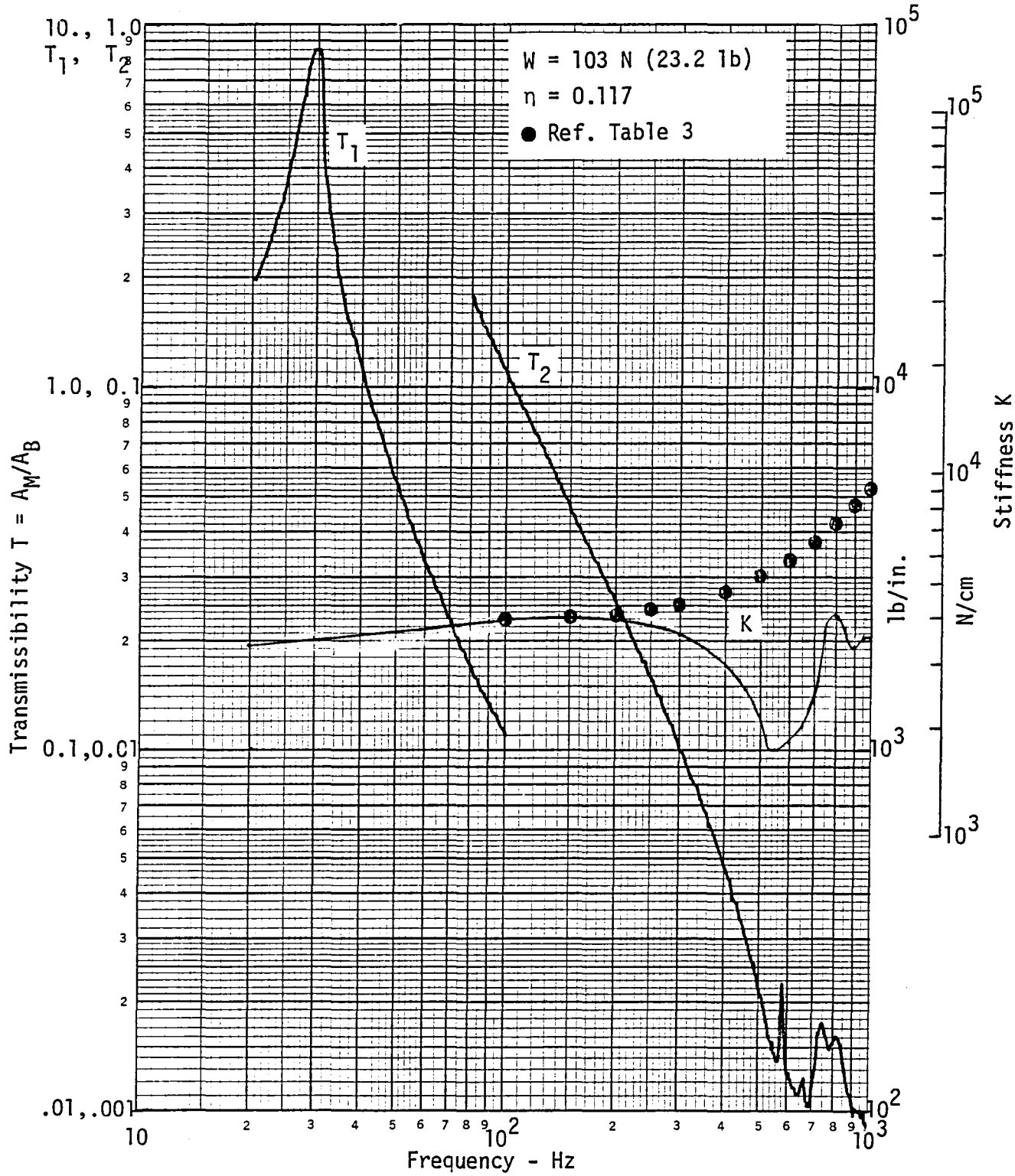

Figure 29b. Measured Transmissibility and Computed Radial Stiffness 22002-1 Isolator.

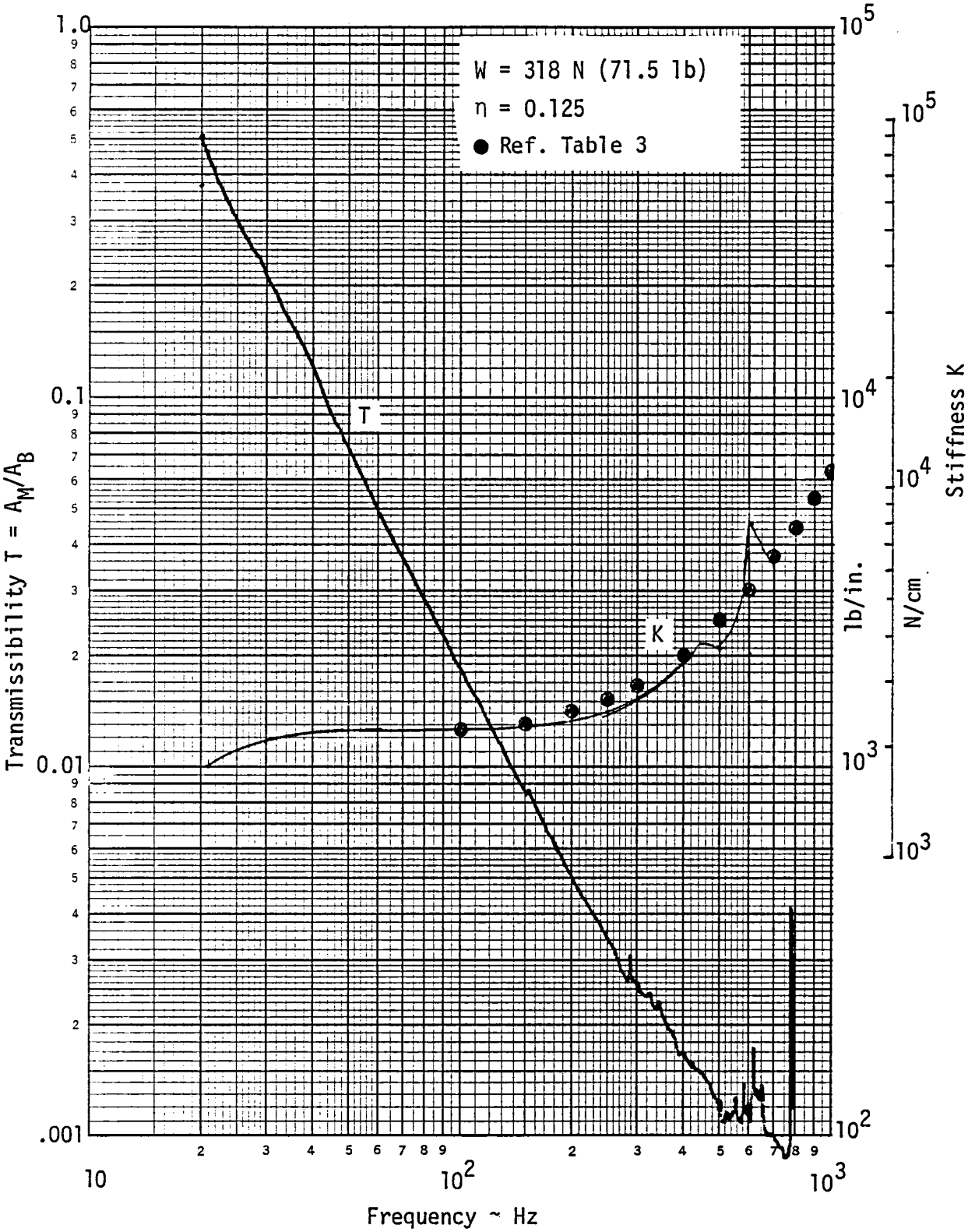

Figure 30a. Measured Transmissibility and Computed Axial Stiffness WRB-030M Isolator.

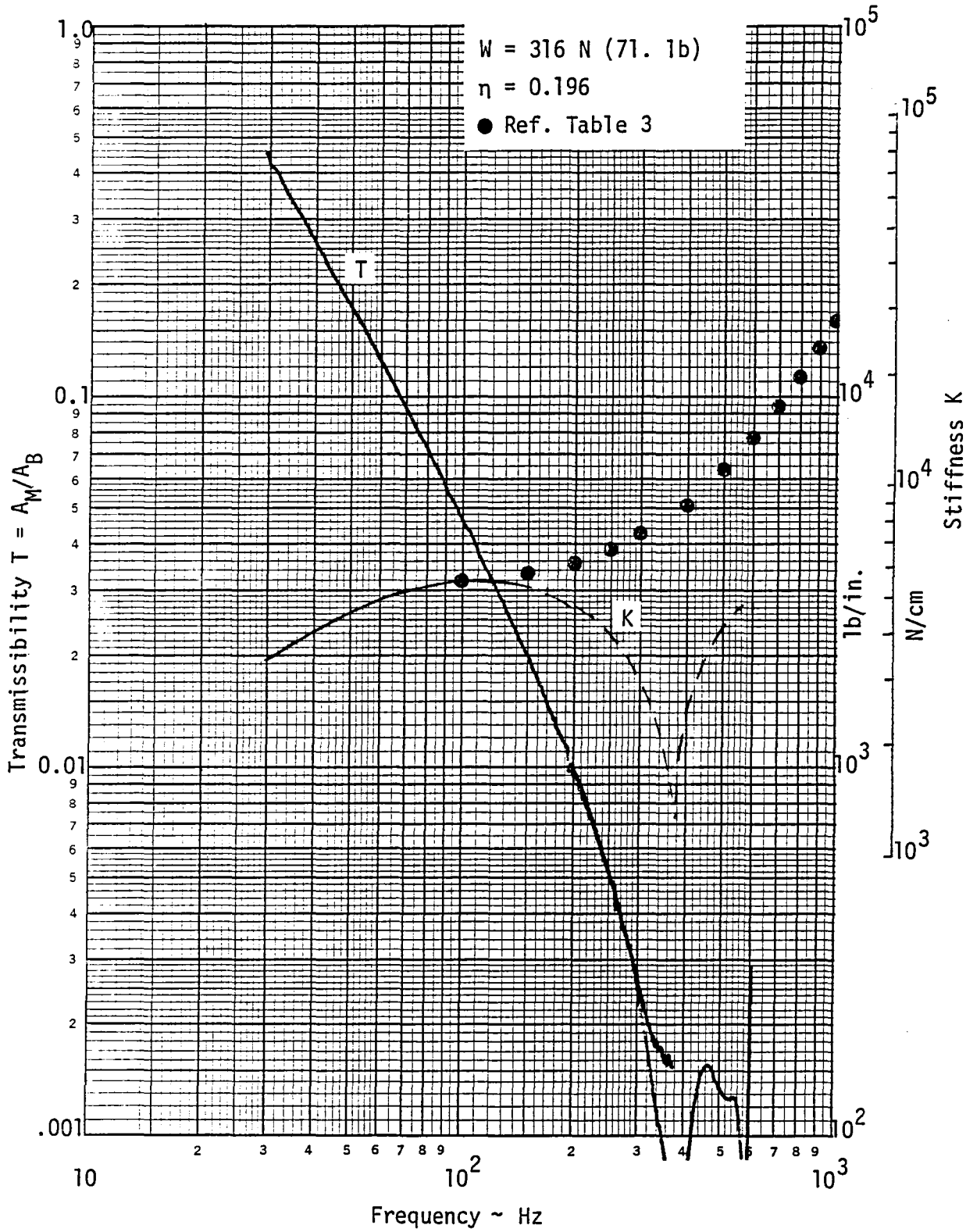

Figure 30b. Measured Transmissibility and Computed Radial Stiffness WRB-030M Isolator.

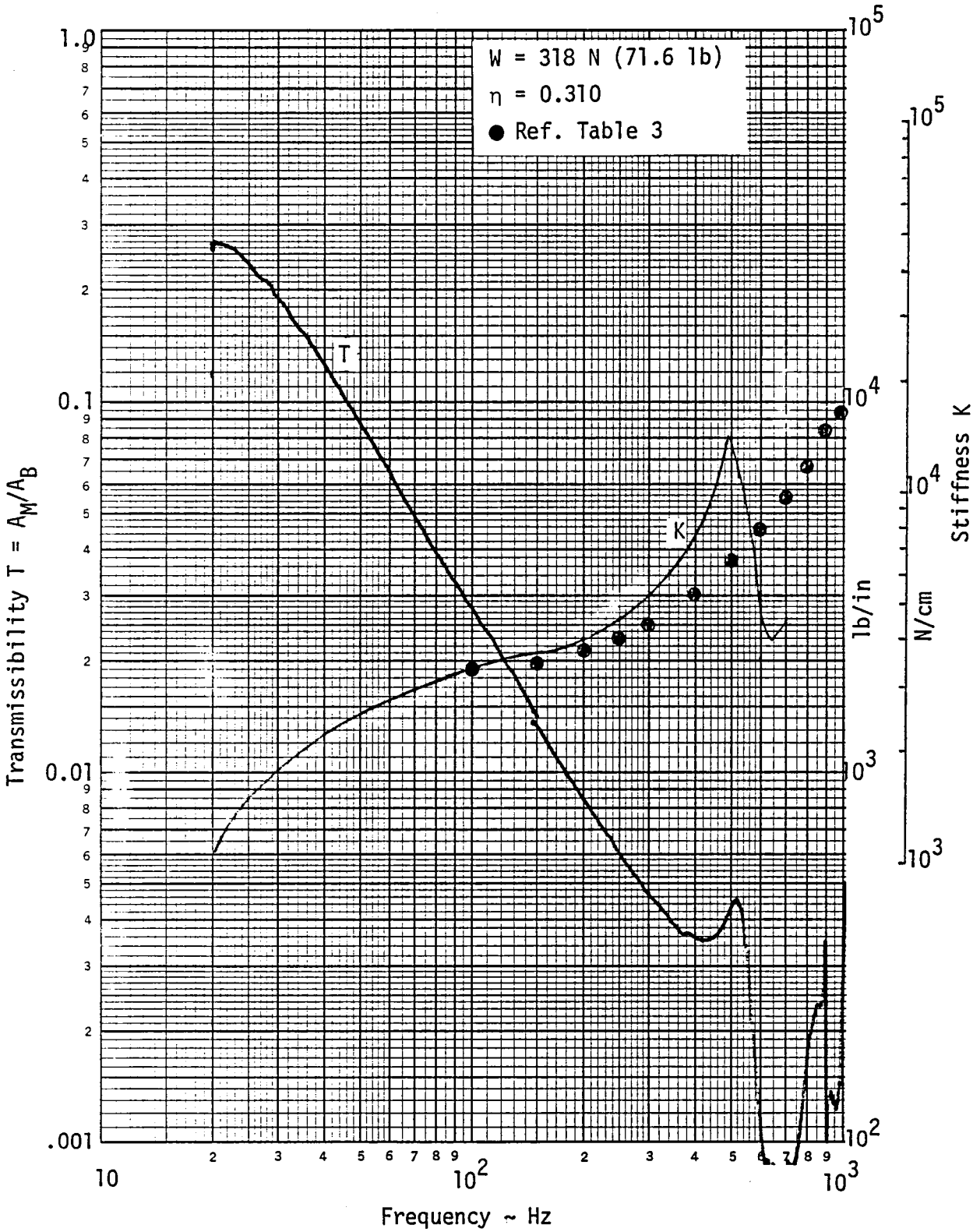

Figure 31a. Measured Transmissibility and Computed Axial Stiffness 22002-11M Isolator.

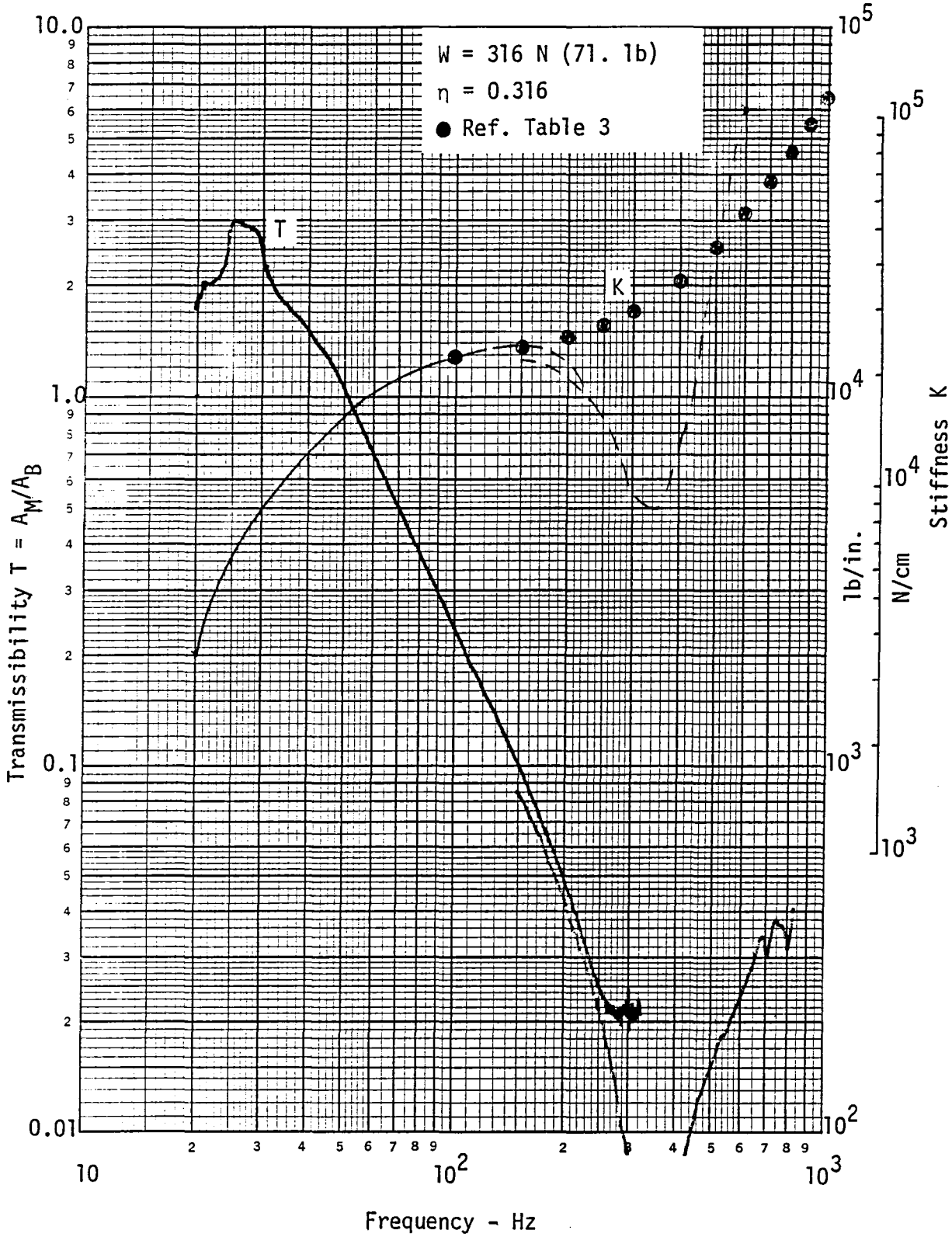

Figure 31b. Measured Transmissibility and Computed Radial Stiffness 22002-11M Isolator.

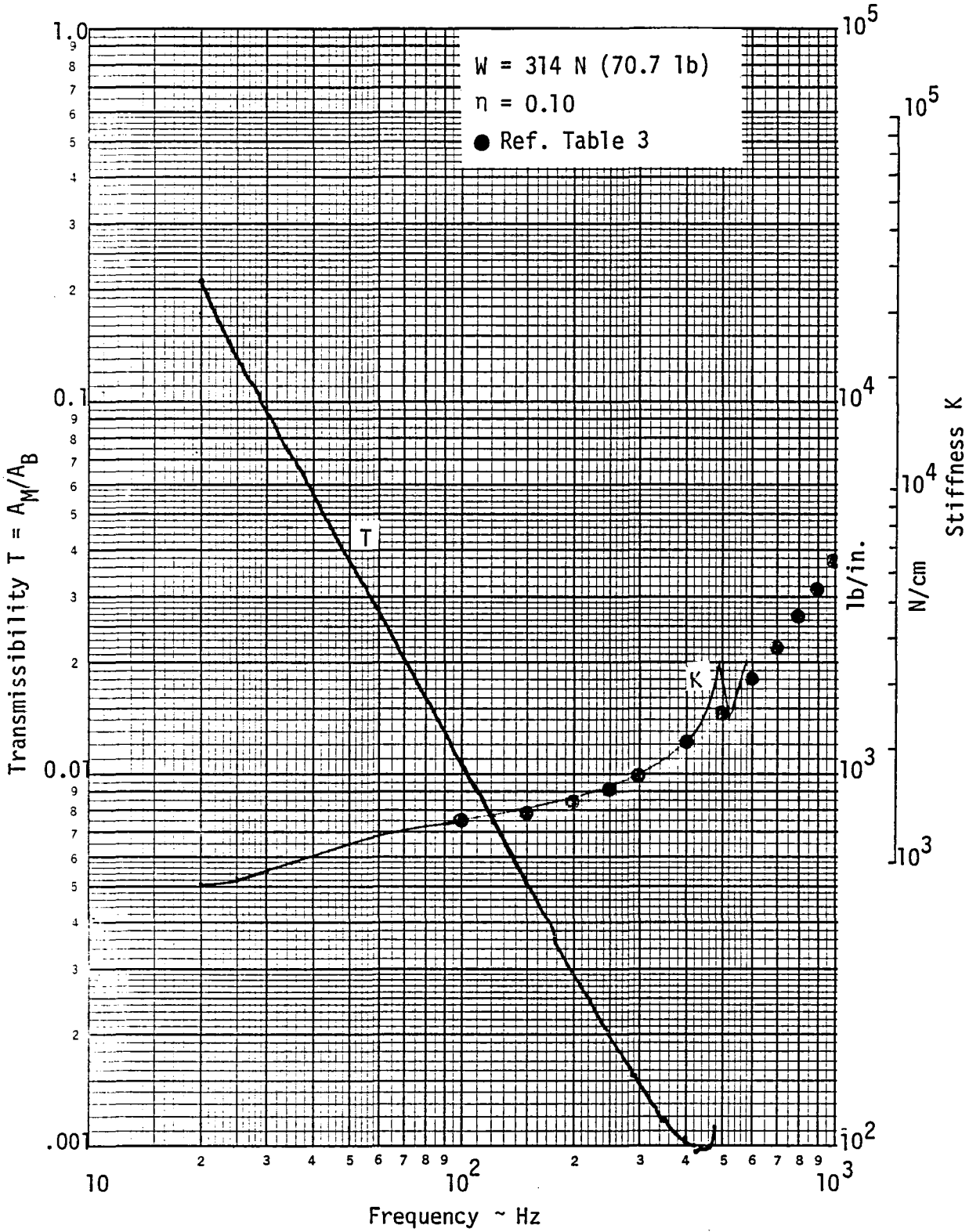

Figure 32a. Measured Transmissibility and Computed Axial Stiffness 206PD-45 Isolators.

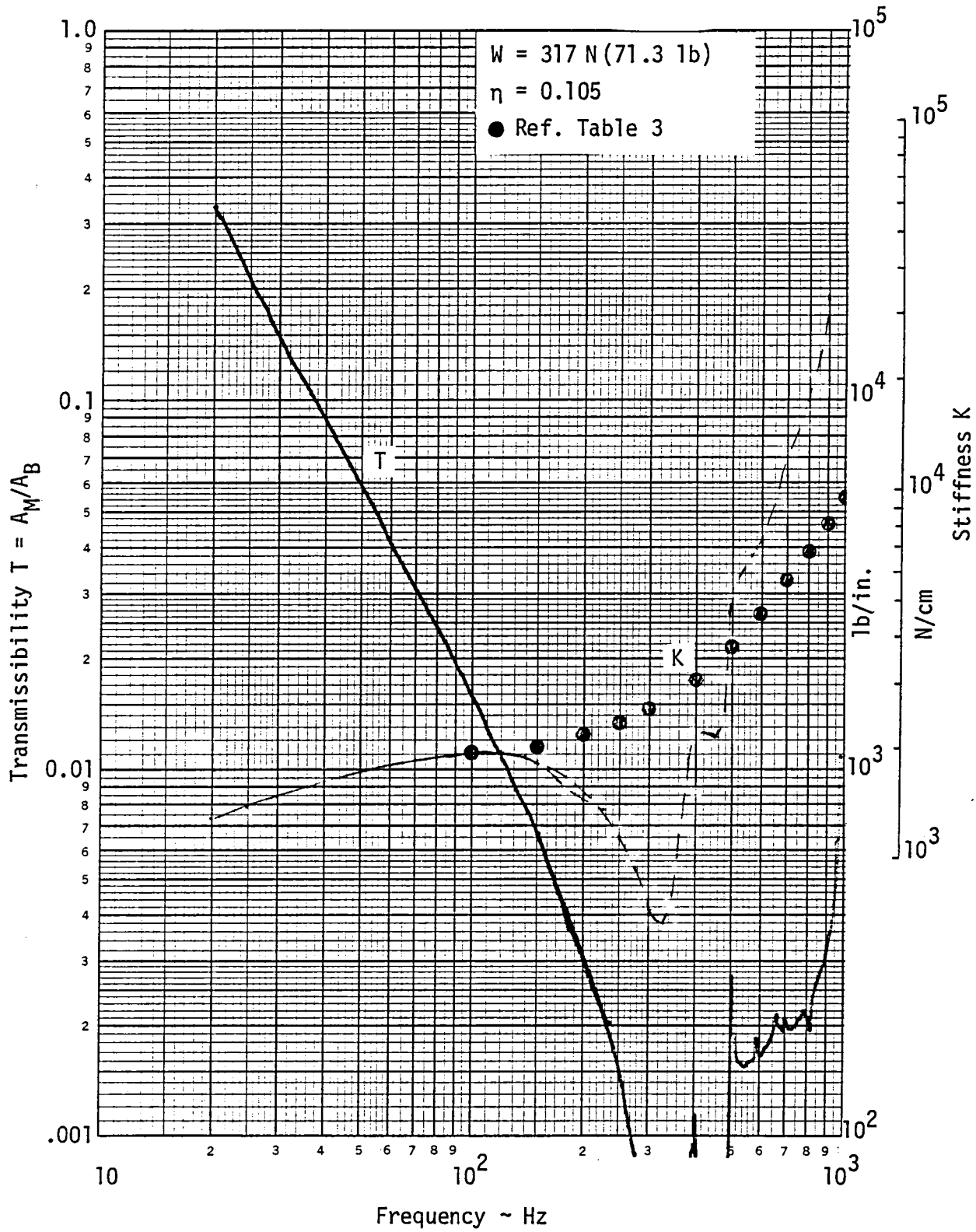

Figure 32b. Measured Transmissibility and Computed Radial Stiffness 206PD-45 Isolator.

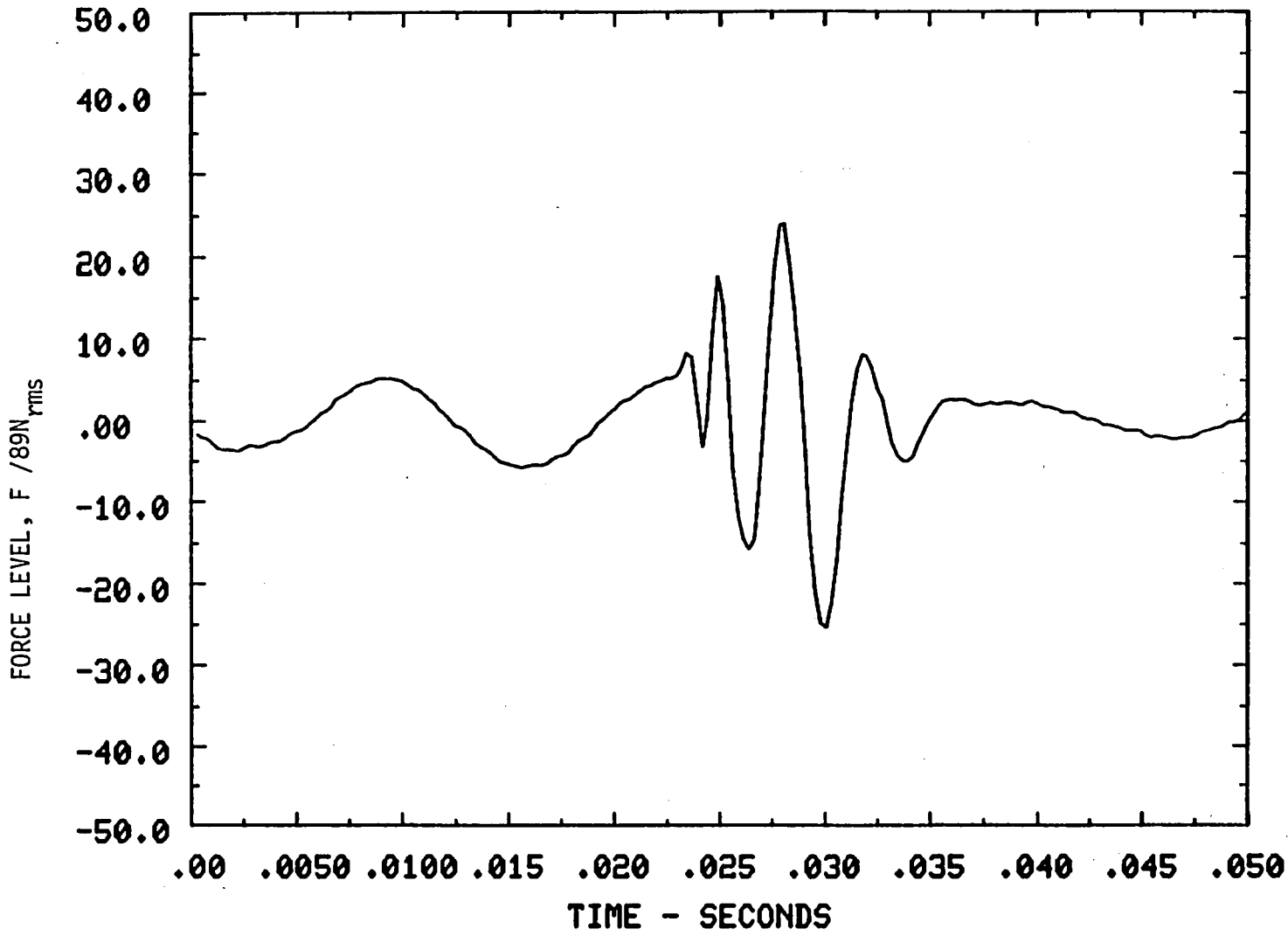

Figure 33. Drive Force Input Time History, Shaped Terminal Peak Sawtooth, 2160 rpm.

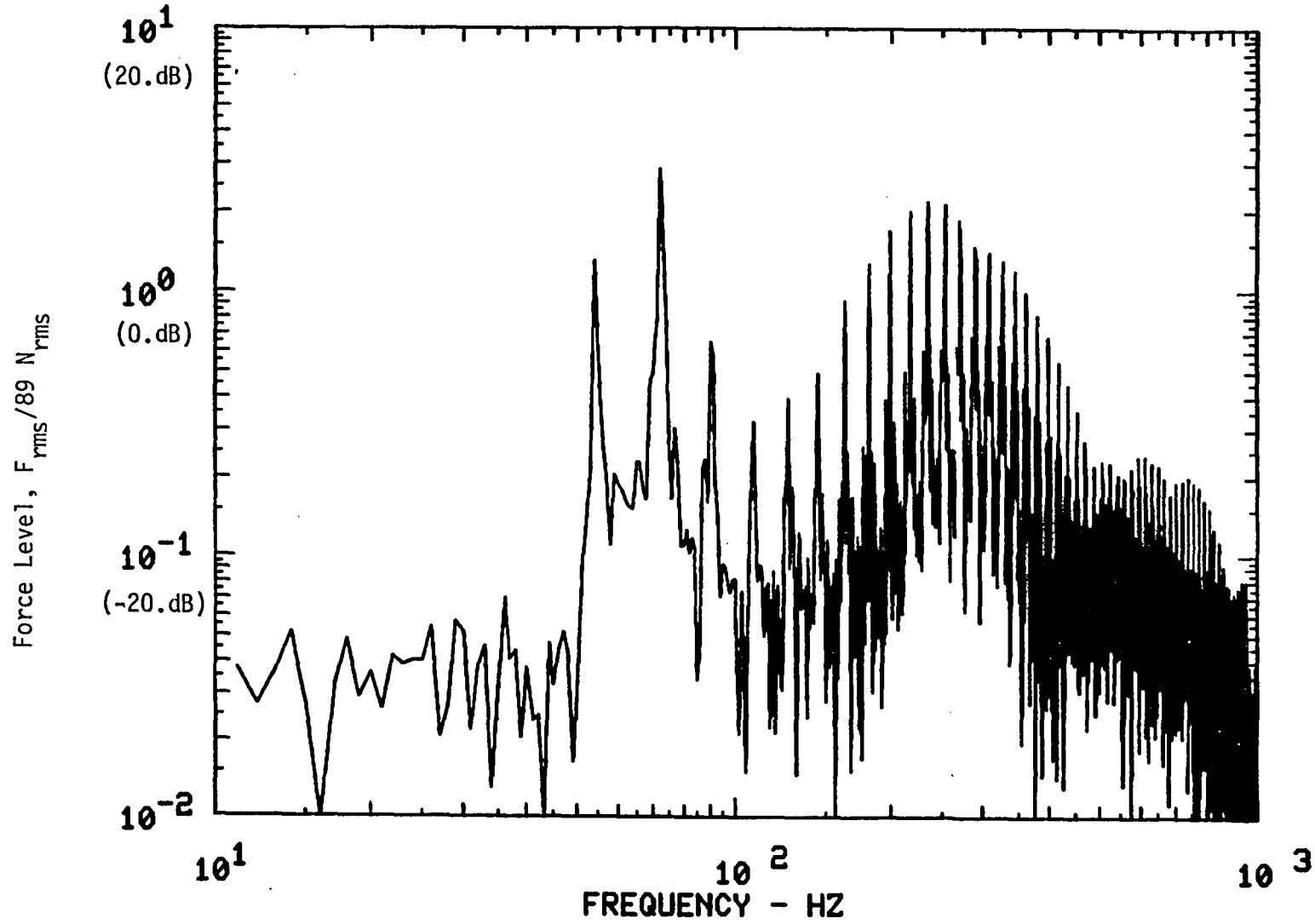

Figure 34. Drive Force Input Spectrum, Shaped Terminal Peak Sawtooth, 2160 rpm.

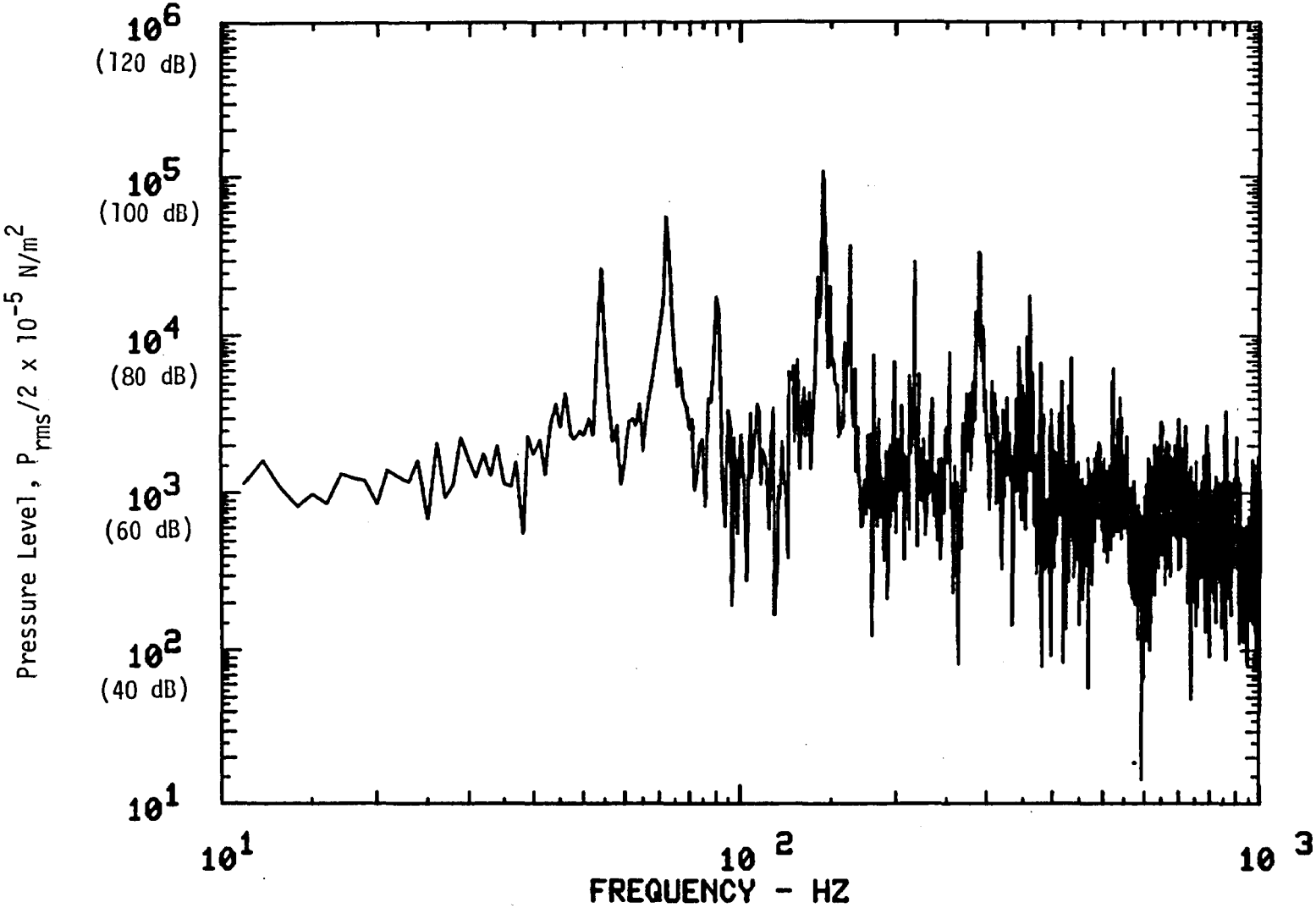

Figure 35. SPL Spectrum, Response at P1, 2160 rpm, Rigid Isolators.

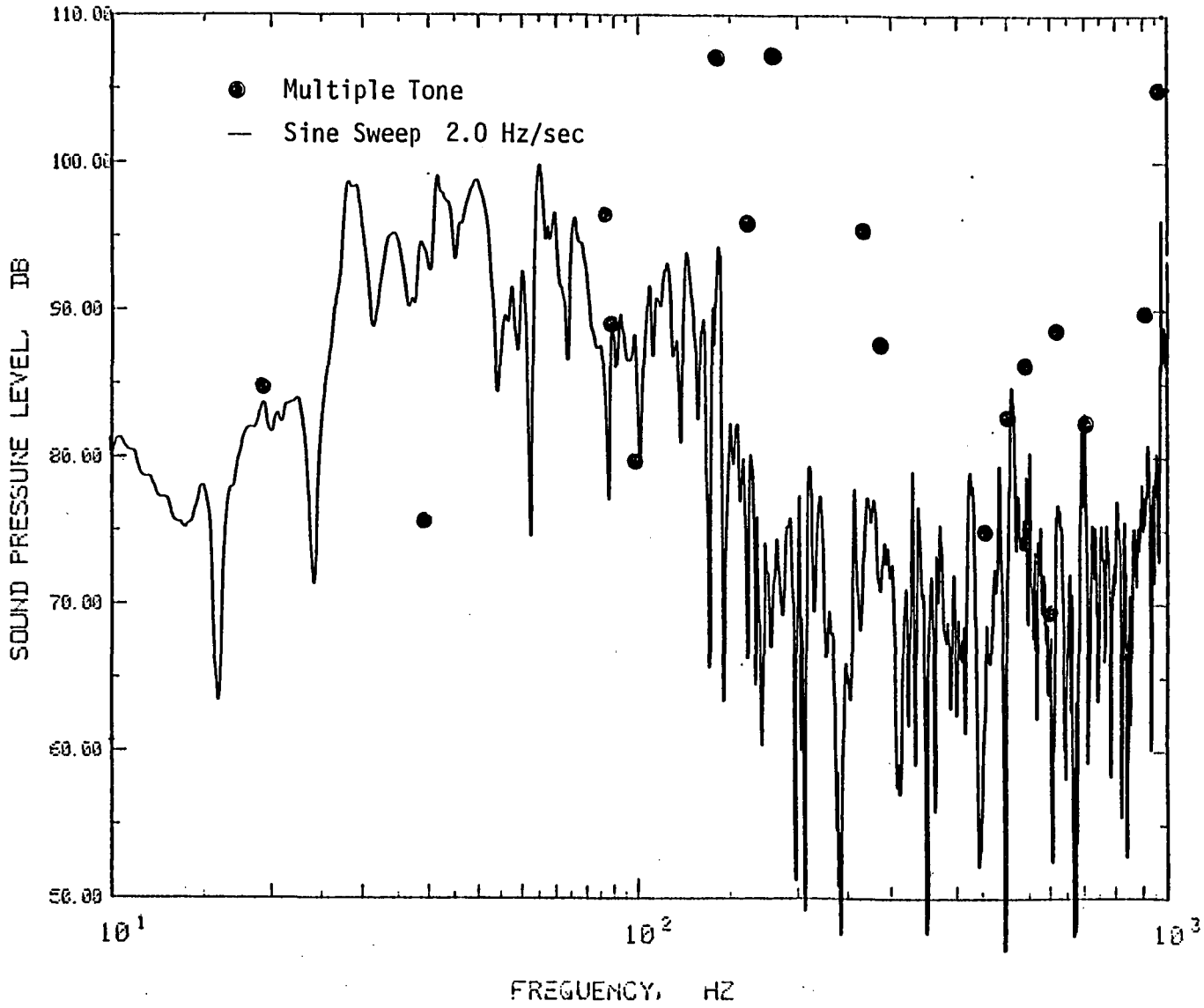

Figure 36. Comparison of SPL Transfer Function for Rigid Isolators, Response at P1, Load Case #2, Ref. 89 N_{rms}.

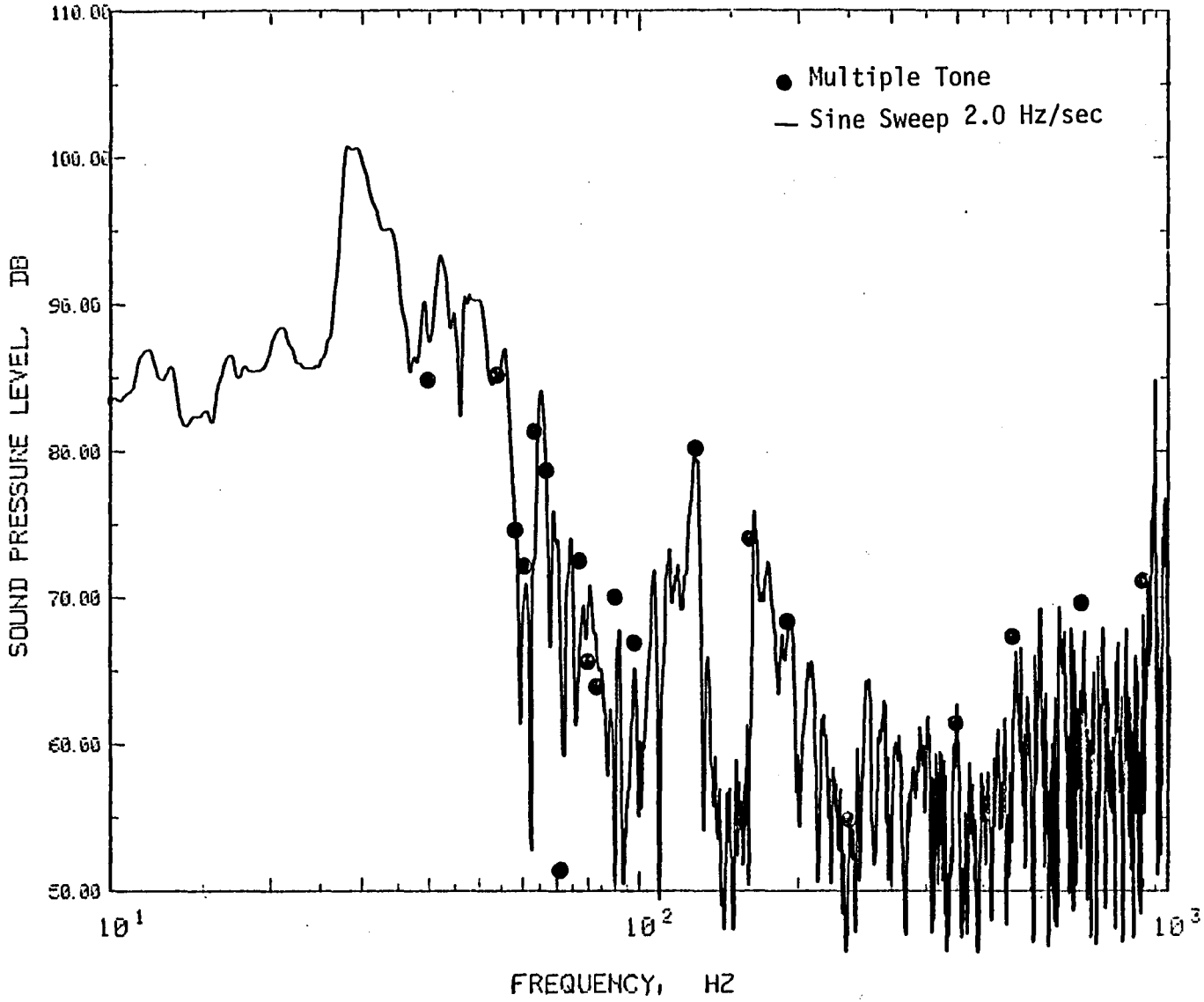

Figure 37. Comparison of SPL Transfer Function for 22002-1 Isolator, Response at P1, Load Case #2, Ref. 89 N_{rms}.

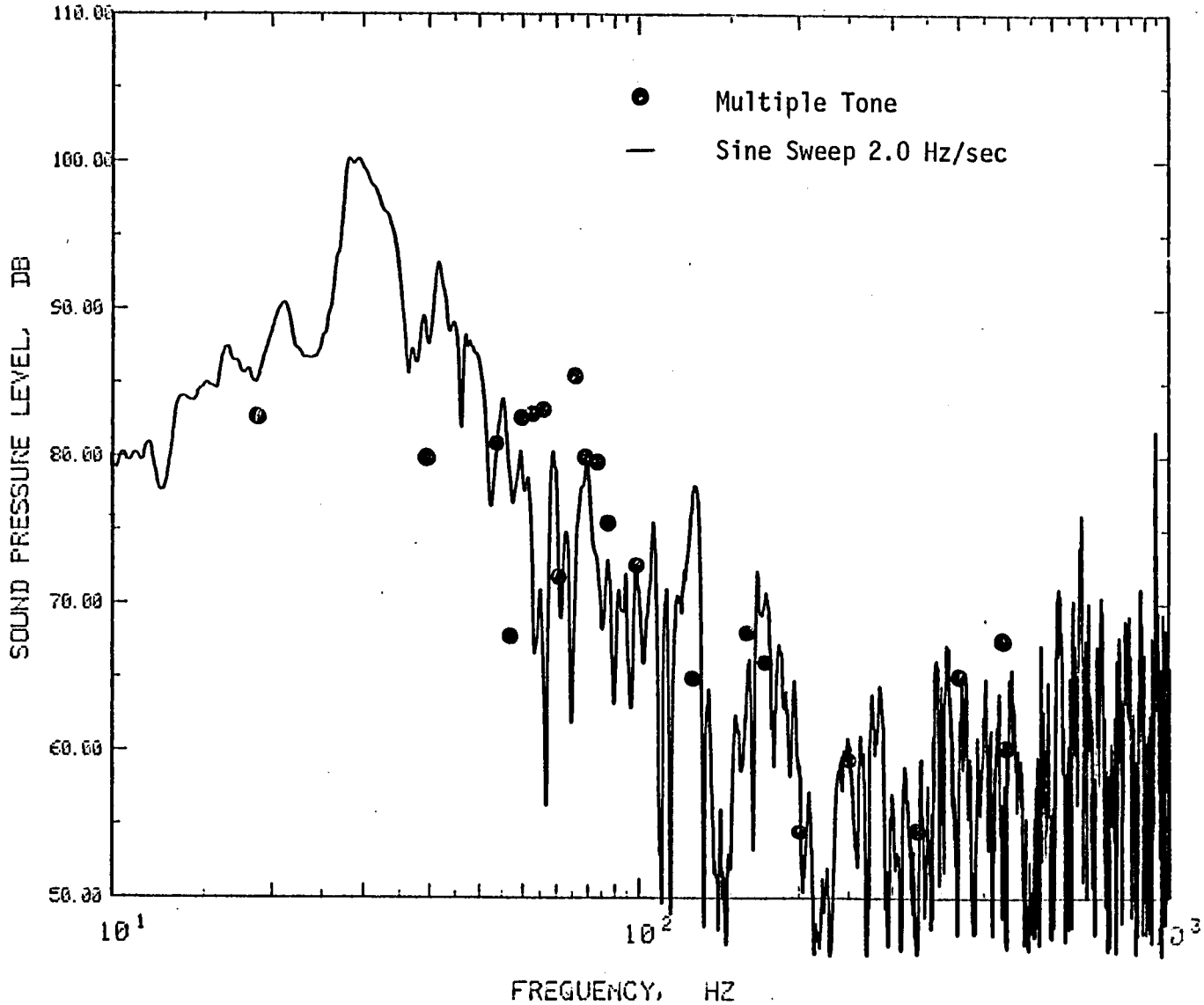

Figure 38. Comparison of SPL Transfer Functions for 22002-1 Isolator, Response at P3, Load Case #2, Ref. 89 N_{rms}.

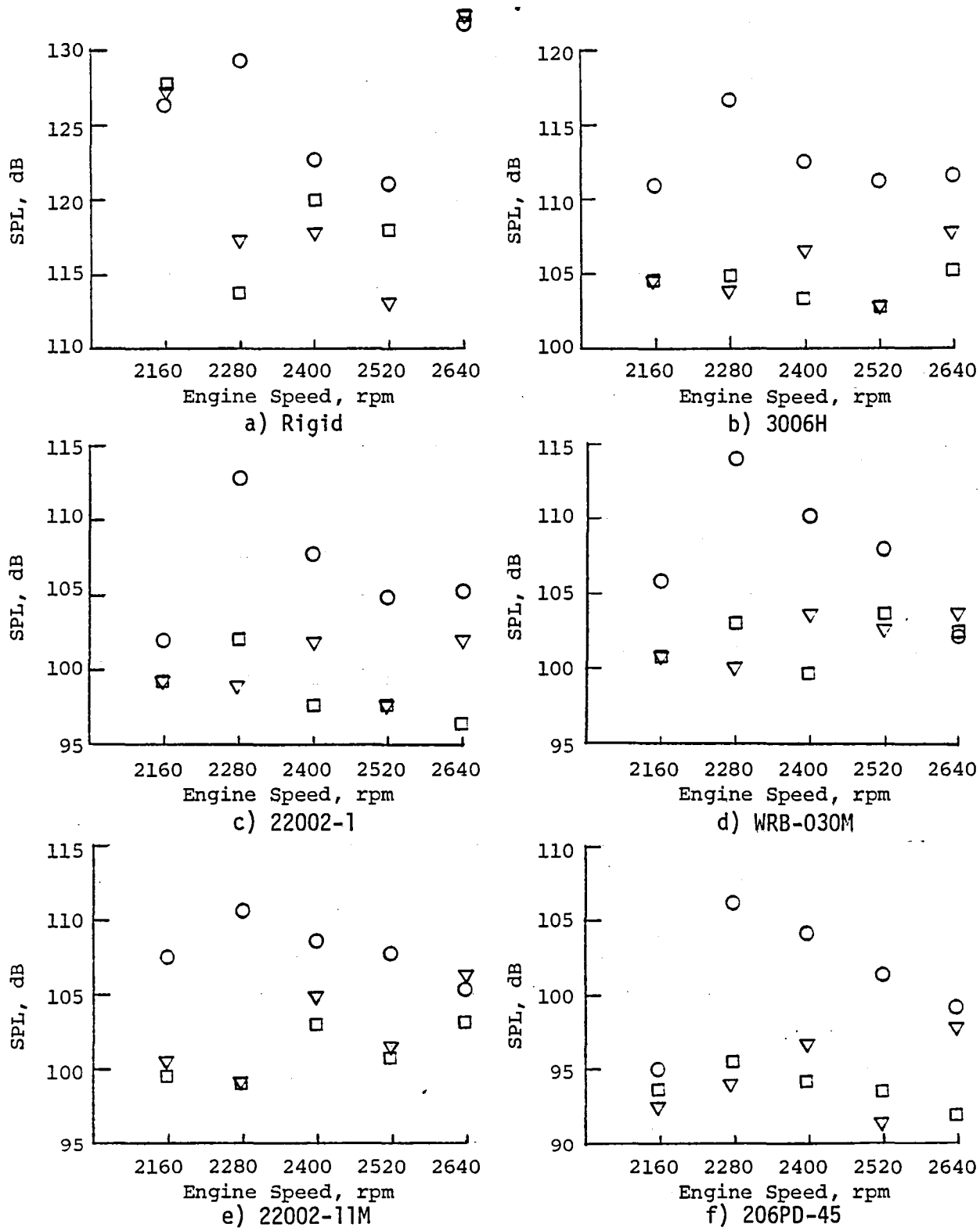

Figure 39. Measured Unweighted Interior Sound Pressure Levels at Various Engine Speeds; □-P1, ▽-P2, ○-P3.

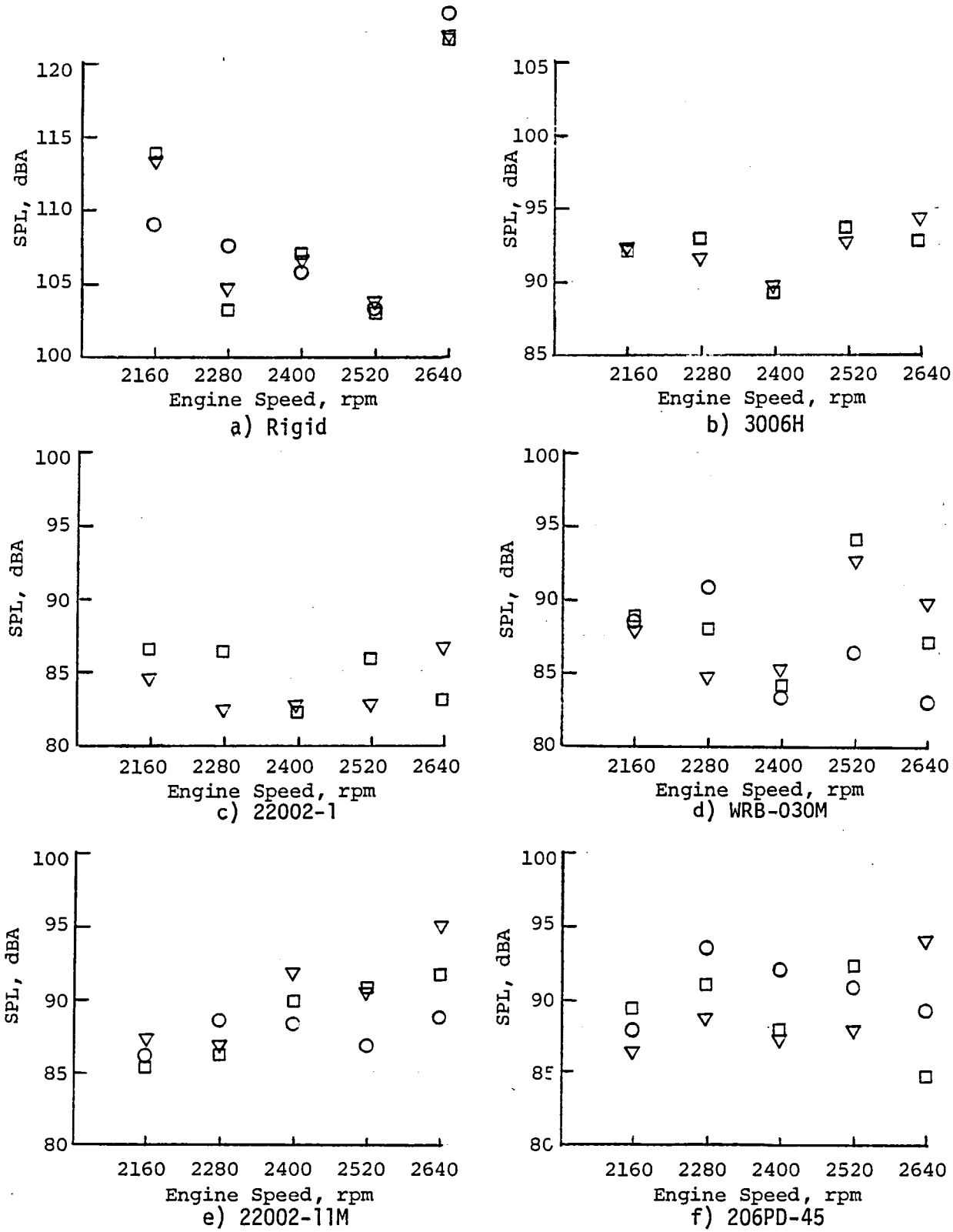

Figure 40. Measured A-Weighted Interior Sound Pressure Levels at Various Engine Speeds; □-P1, ▽-P2, ○-P3.

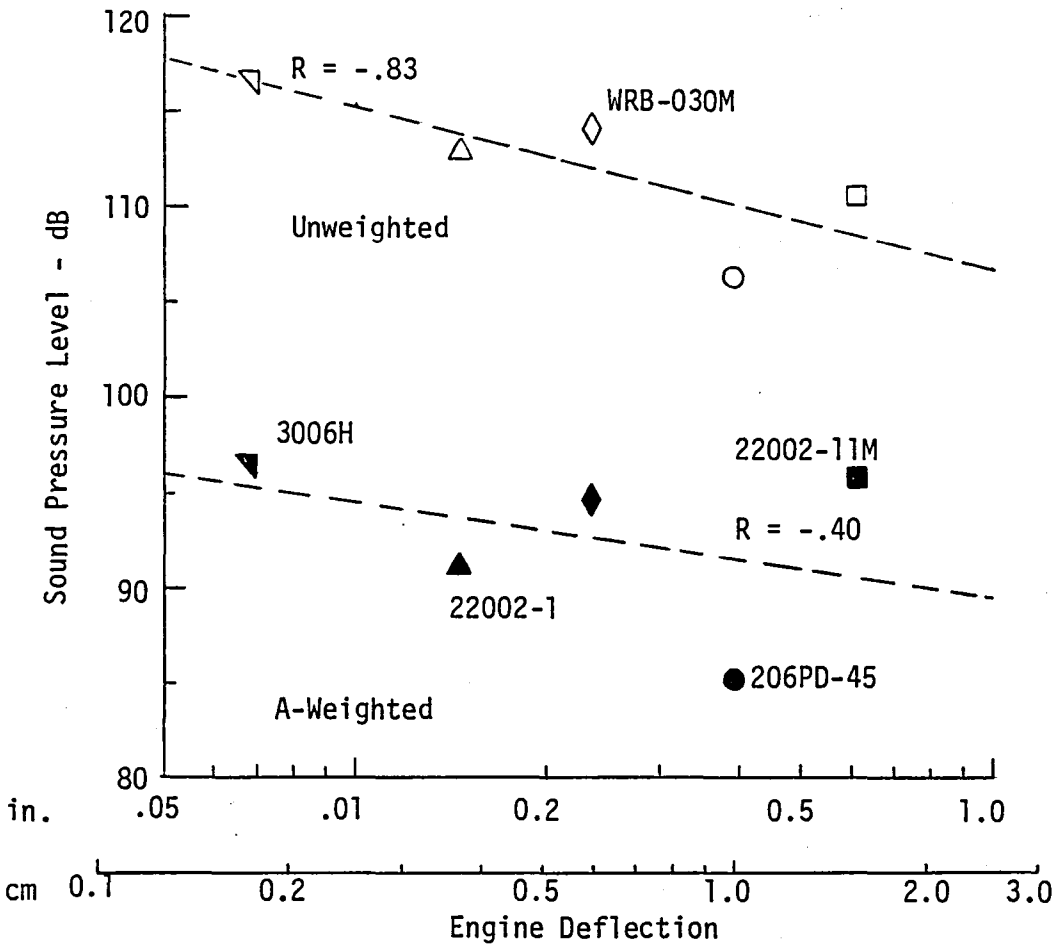

Figure 41. Correlation of Measured P123 OASPL With Predicted Maximum Engine Deflection Due to Static Torque.

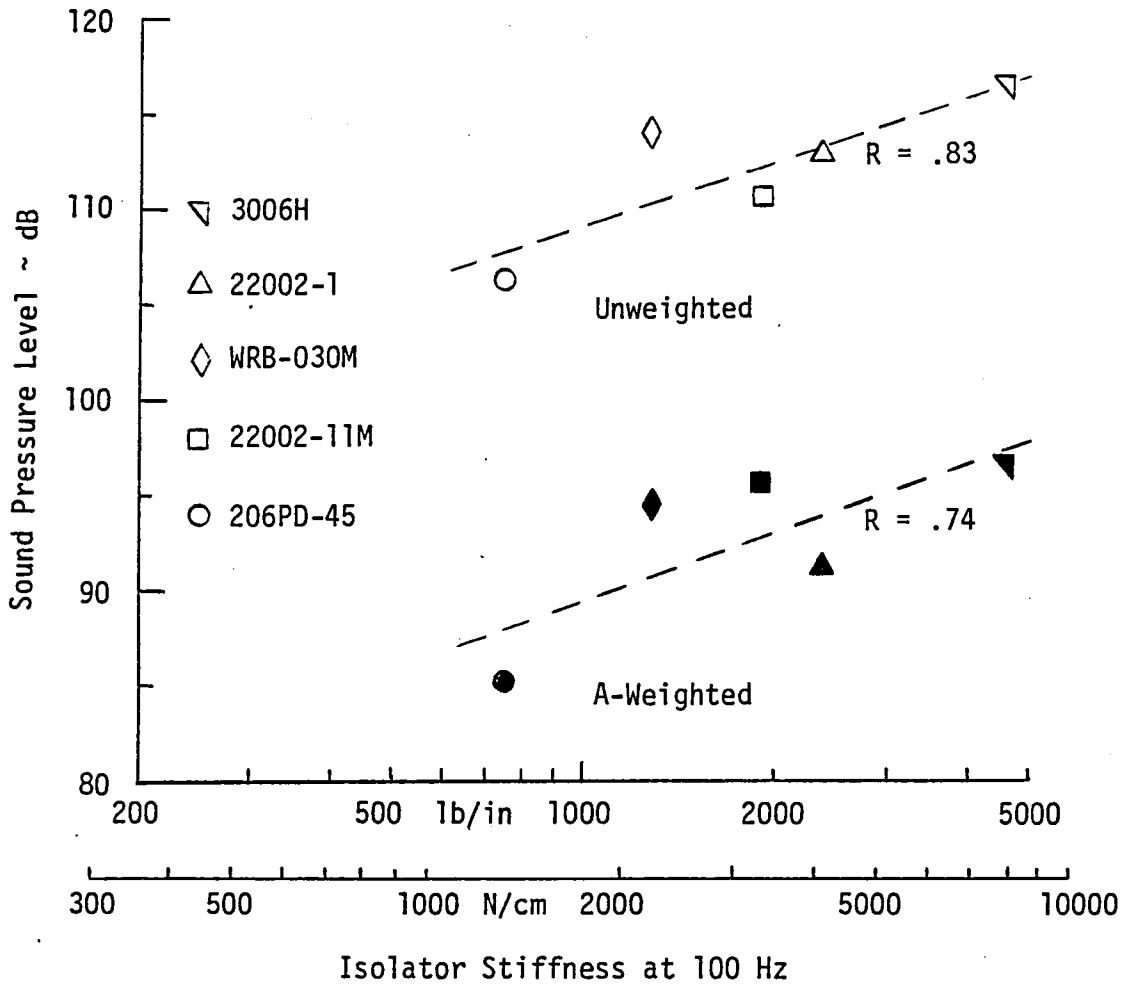

Figure 42. Correlation of Measured P123 OASPL with Isolator Dynamic Stiffness at 100 Hz.

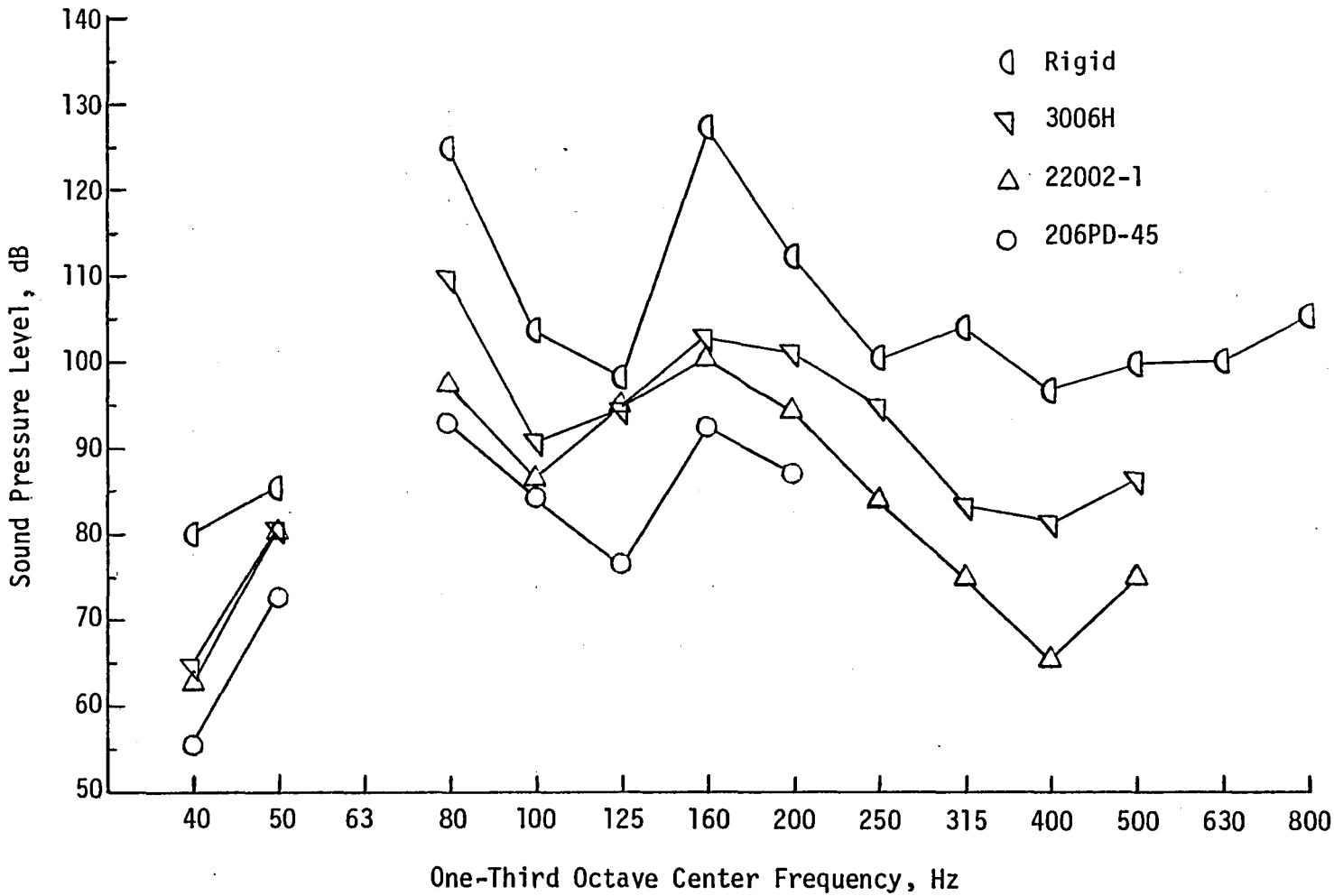

Figure 43. Comparison of Measured Sound Pressure Level P123 Spectra for Various Isolator Configurations at 2160 rpm.

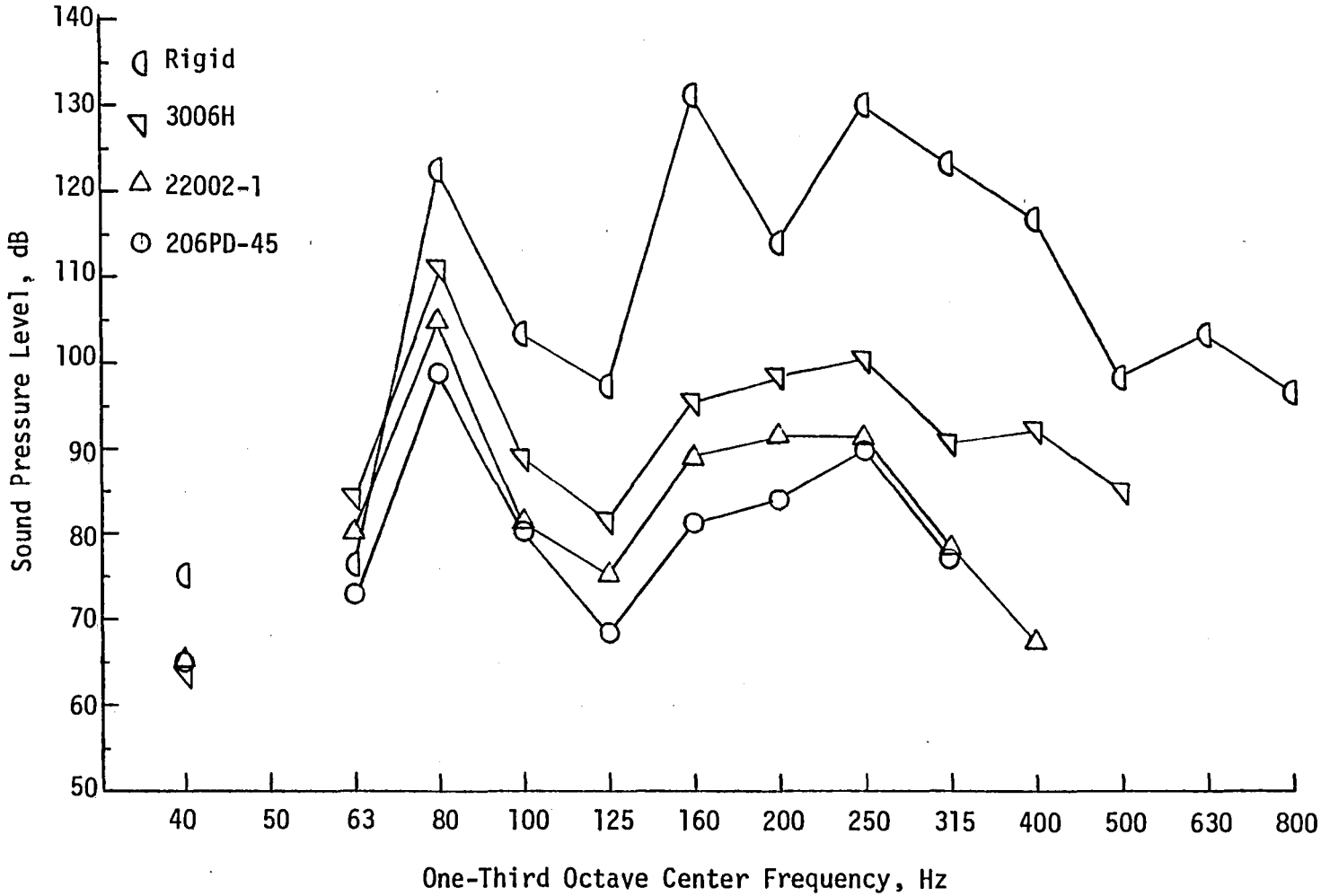

Figure 44. Comparison of Measured Sound Pressure Level P123 Spectra for Various Isolator Configurations at 2640 rpm.

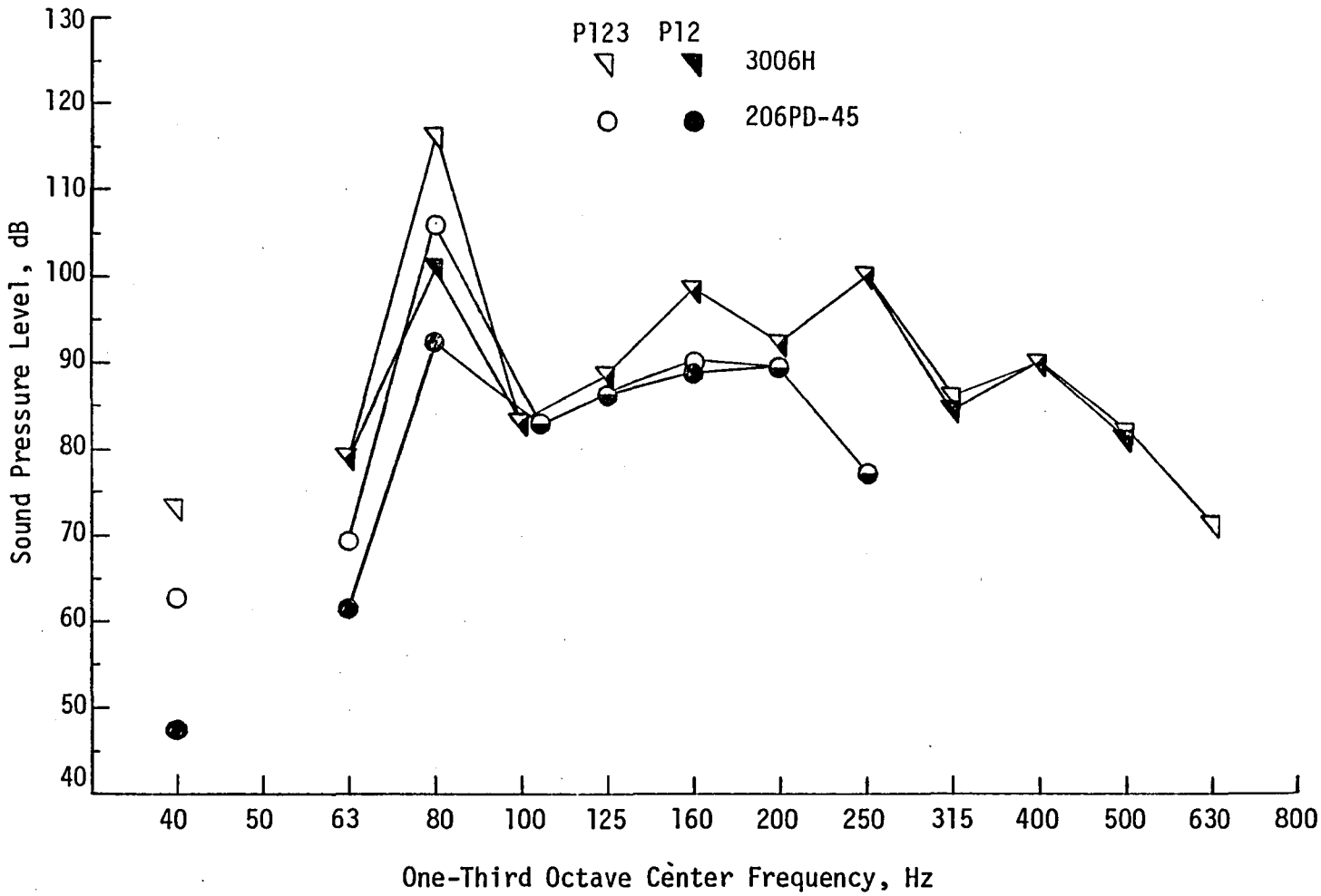

Figure 45. Effect of Removing P3 from Measured Sound Pressure Level Spectra at 2280 rpm.

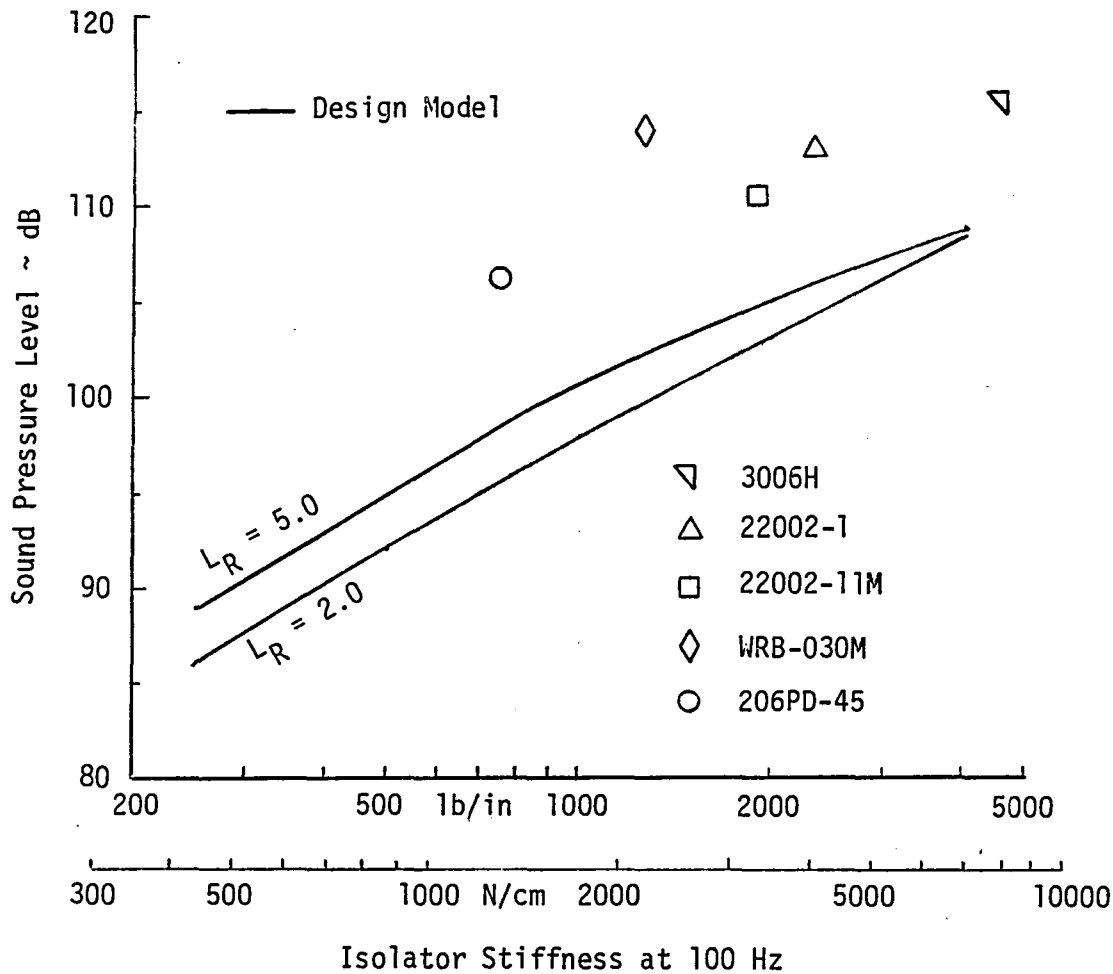

Figure 46. Comparison of Measured P123 Unweighted OASPL Data to Isolator Design Specification Model.

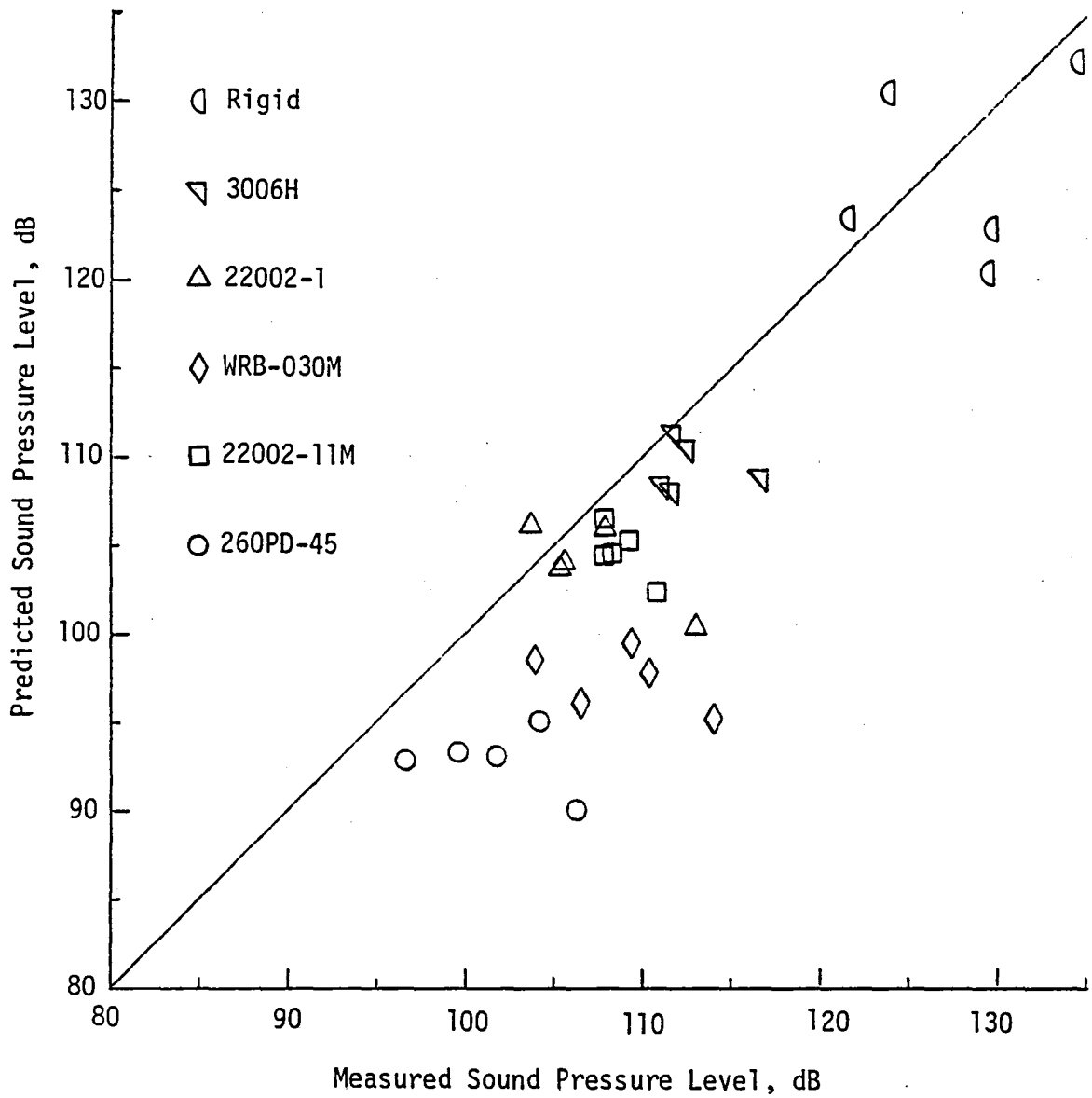

Figure 47. Correlation of Predicted to Measured Unweighted OASPL with all Microphones Active, P123.

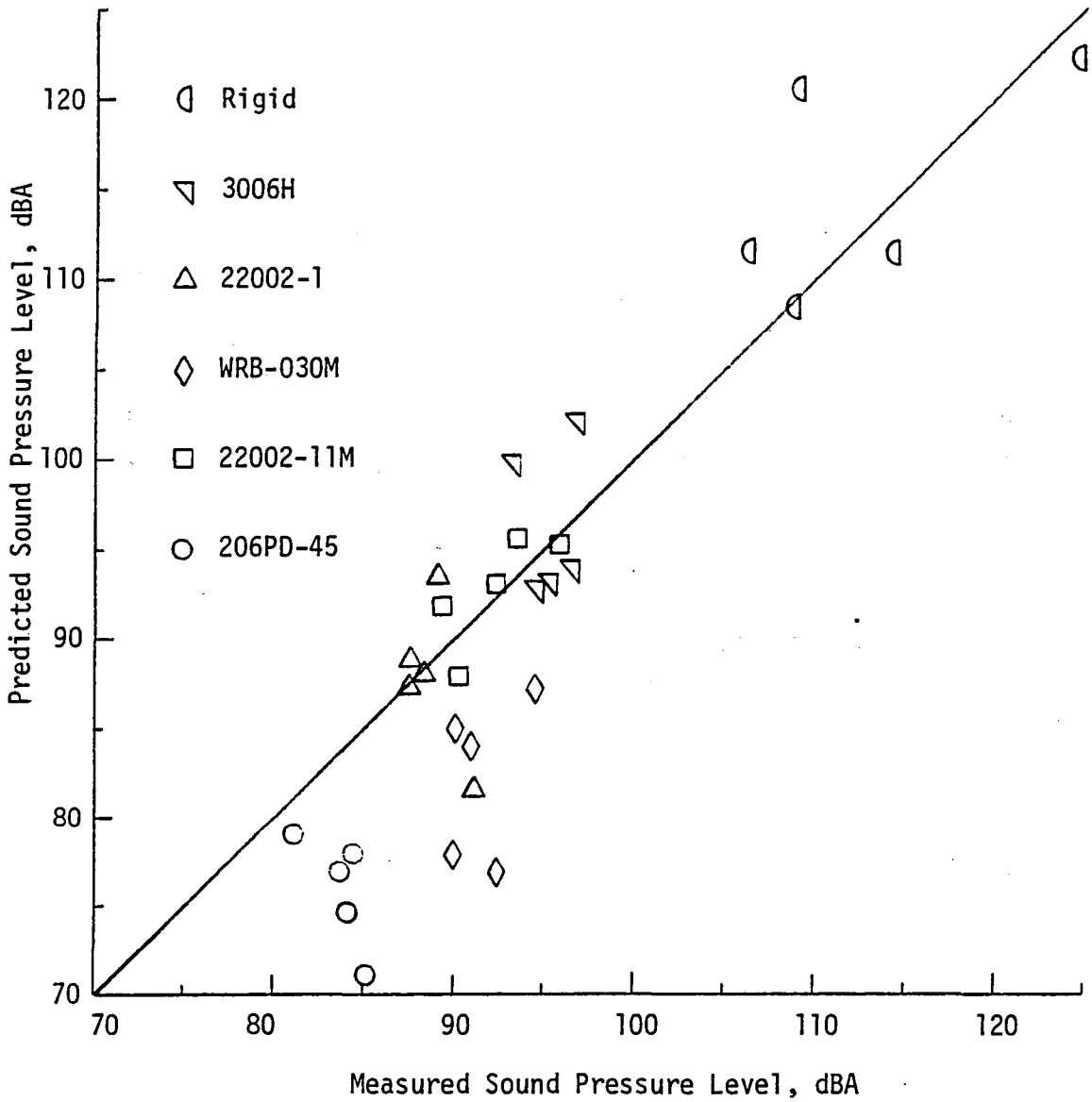

Figure 48. Correlation of Predicted to Measured A-Weighted OASPL with all Microphones Active, P123.

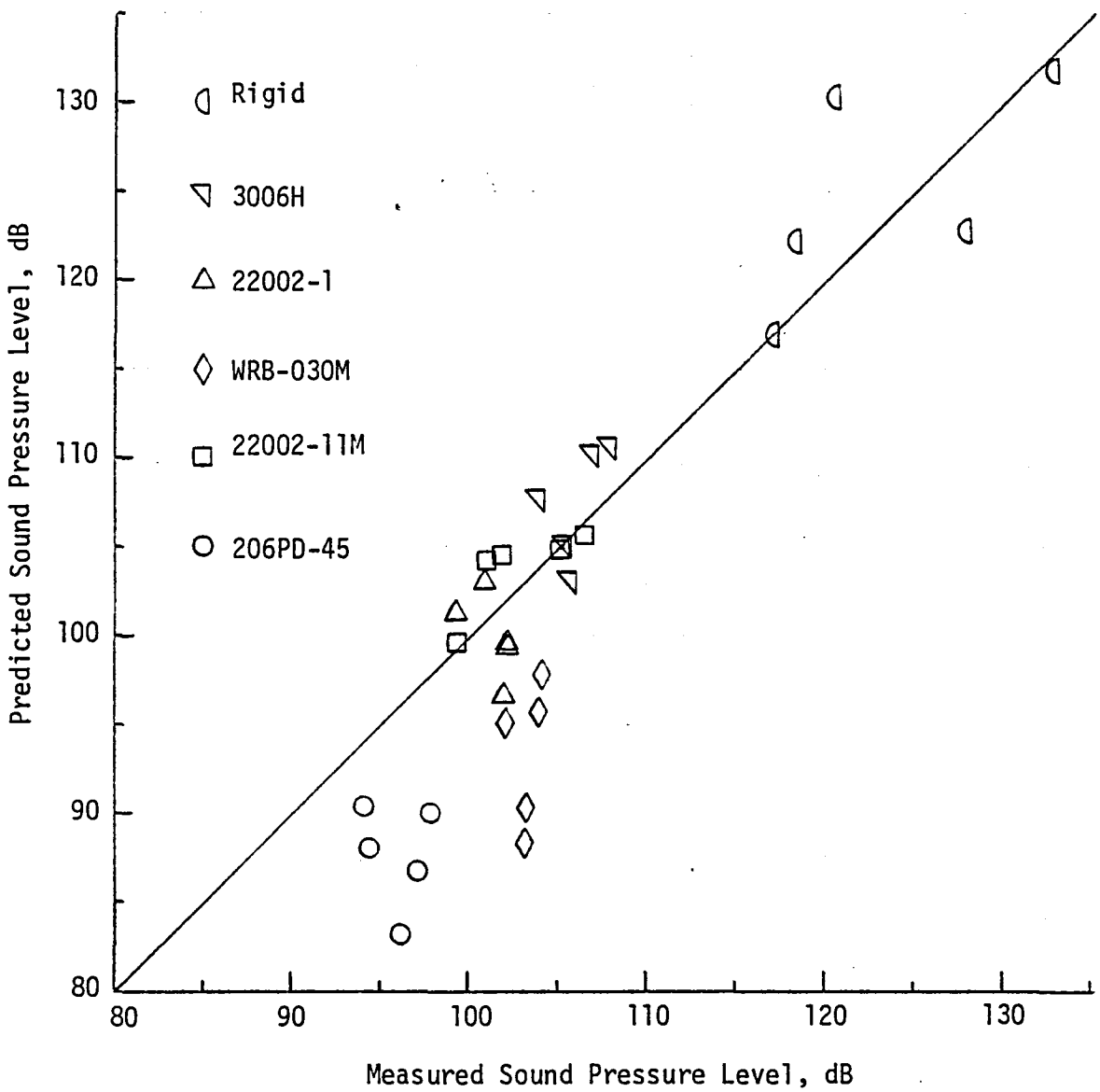

Figure 49. Correlation of Predicted to Measured Unweighted OASPL with P3 Removed, P12.

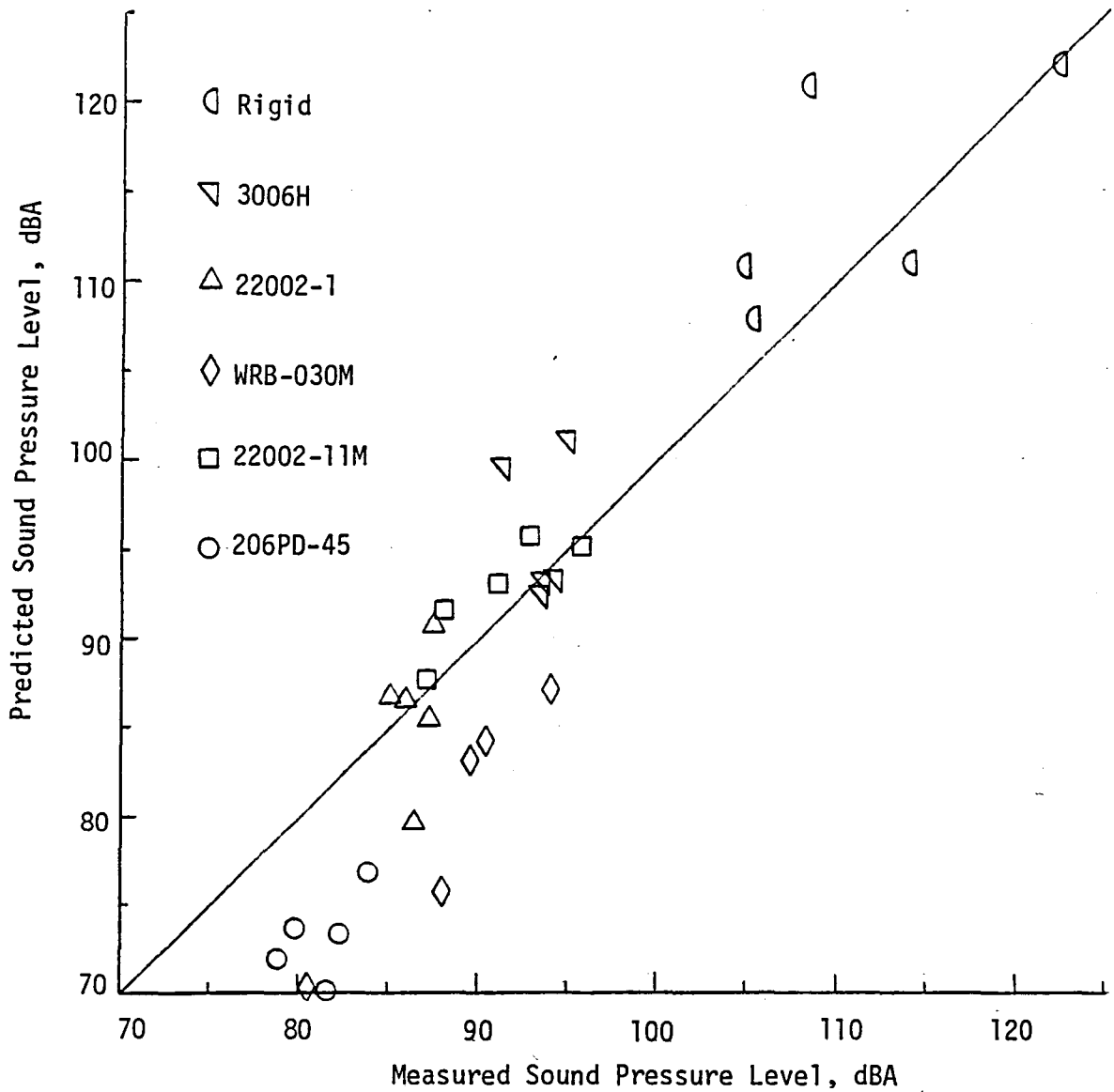

Figure 50. Correlation of Predicted to Measured A-weighted OASPL with P3 Removed, P12.

1. Report No.	2. Government Accession No.	3. Recipient's Catalog No.
NASA CR-166021		

4. Title and Subtitle	5. Report Date
Design and Test of Aircraft Engine Isolators for Reduced Interior Noise	December 1982
	6. Performing Organization Code

7. Author(s)	8. Performing Organization Report No.
James F. Unruh and Dennis C. Scheidt	06-4860
	10. Work Unit No.

9. Performing Organization Name and Address	11. Contract or Grant No.
Southwest Research Institute P.O. Drawer 28510 San Antonio, Texas 78284	NAS 1-14861
	13. Type of Report and Period Covered
12. Sponsoring Agency Name and Address	Contractor Report
National Aeronautics & Space Administration Washington, D.C. 20546	14. Sponsoring Agency Code

15. Supplementary Notes

Langley Technical Monitor: John S. Mixson
Final Report

16. Abstract

Improved engine vibration isolation was proposed to be the most weight and cost efficient retrofit structure-borne noise control measure for single engine general aviation aircraft. A study was carried out with the objectives: (1) to develop an engine isolator design specification for reduced interior noise transmission, (2) select/design candidate isolators to meet a 15 dB noise reduction design goal, and (3) carry out a proof of concept evaluation test. Analytical model of the engine, vibration isolators and engine mount structure were coupled to an empirical model of the fuselage for noise transmission evaluation. The model was used to develop engine isolator dynamic properties design specification for reduced noise transmission. Candidate isolators were chosen from available product literature and retrofit to a test aircraft. A laboratory based test procedure was then developed to simulate engine induced noise transmission in the aircraft for a proof of concept evaluation test. Three candidate isolator configurations were evaluated for reduced structure-borne noise transmission relative to the original equipment isolators. Analysis of the resulting noise transmission data show that (1) overall maximum interior noise level reduction on the order of 10 dB were realized from the candidate isolators, (2) the noise transmission model used in the isolator design specification was quite adequate for evaluating trends in improved isolation for known isolator dynamic properties.

17. Key Words (Suggested by Author(s))	18. Distribution Statement
Interior Noise Engine Isolators General Aviation	Unclassified - Unlimited Subject Category 71

19. Security Classif. (of this report)	20. Security Classif. (of this page)	21. No. of Pages	22. Price
Unclassified	Unclassified	116	

End of Document